BremHLR

Kompetenzzentrum für Höchstleistungsrechnen Bremen

Statusbericht 2016

des

Kompetenzzentrums

für

Höchstleistungsrechnen Bremen

–BremHLR–

Bremen, Juni 2017

Universität Bremen JACOBS UNIVERSITY ALFRED-WEGENER-INSTITUT HELMHOLTZ-ZENTRUM FÜR POLAR- UND MEERESFORSCHUNG Hochschule Bremerhaven

HLRN

Norddeutscher Verbund für Hoch- und Höchstleistungsrechnen

www.bremhlr.uni-bremen.de

Das Berichtsjahr 2016 in Stichpunkten

- Weitere Steigerung der Bremer Nutzung der Ressourcen des Norddeutschen Verbunds für Hoch- und Höchstleistungsrechnen (HLRN)
- Erfolgreicher 11. BremHLR Workshop zur Einführung in die parallele Programmierung
- Stabiler Produktionsbetrieb des derzeitigen Rechnersystems HLRN-III
- Vorbereitungen zur Beschaffung des Nachfolgesystems HLRN-IV

Inhaltsverzeichnis

1 BremHLR: Aufgaben und organisatorische Struktur

1.1 Aufgaben

Das Land Bremen beteiligt sich am Norddeutschen Verbund für Hoch- und Höchstleistungsrechnen – HLRN – um an dem rasanten Fortschritt der Computer- und Softwaretechnologie Teil zu haben. Das Kompetenzzentrum für Höchstleistungsrechnen Bremen – BremHLR – unterstützt dazu Wissenschaftler im wissenschaftlichen Rechnen insbesondere im Land Bremen. Die Fachberater des BremHLR leisten Unterstützung für Projekte sowohl in der Konzeption, der Antragstellung als auch der Durchführung. Der Schwerpunkt der Unterstützung liegt hierbei auf Projekten auf dem HLRN-System. Seit 2005 wurde die Betreuung aber auch auf Rechenprojekte an den nationalen Höchstleistungsrechenzentren wie z. B. dem Jülich Supercomputing Centre (JSC) ausgeweitet.

Als Bestandteil im Kompetenznetzwerk des HLRN beteiligt sich BremHLR unter anderem an der fachspezifischen Nutzerberatung, der Pflege von Software-Paketen und der Veranstaltung überregionaler Nutzerworkshops. Die Geschäftsstelle des BremHLR ist an der Universität Bremen im Zentrum für Technomathematik angesiedelt.

Das BremHLR wurde am 1. Juli 2003 als Kooperation zwischen der Universität Bremen (UB), der Jacobs University Bremen (JUB) und dem Alfred-Wegener-Institut für Polar- und Meeresforschung (AWI) gegründet. Seit April 2008 ist auch die Hochschule Bremerhaven (HBHV) Kooperationspartner des BremHLR. Das Kompetenzzentrum wird von den beteiligten Kooperationspartnern sowie der Bremer Senatorin für Wissenschaft, Gesundheit und Verbraucherschutz (SfWGV) anteilig finanziell getragen. Seit Januar 2014 ist die JUB als ideelles Mitglied beitragsfrei gestellt.

1.2 Struktur

Dem Lenkungsausschuss des BremHLR als oberstes beschlussfassendes und steuerndes Gremium gehören in der Berichtsperiode folgende Vertreter der kooperierenden Einrichtungen an. Im Einzelnen sind dies:

- Prof. Dr. Alfred Schmidt (UB/Zentrum für Technomathematik ZeTeM)
- Prof. Dr. Wolfgang Hiller (AWI/Rechenzentrum, UB/FB3)
- Prof. Dr. Ulrich Kleinekathöfer (JUB)
- Prof. Dr. Stephan Frickenhaus (HBHV)
- Helmuth Wolf (SfWGV)

Die fachspezifische Betreuung der Projekte am Norddeutschen Verbund für Hoch- und Höchstleistungsrechnen (HLRN) sowie von Projekten an anderen nationalen Höchstleistungsrechenzentren wird von den Fachberatern des BremHLR geleistet, die ebenfalls den Einrichtungen der Kooperationspartner angehören. Im Berichtszeitraum waren folgende Fachberater tätig:

- Dr. Lars Nerger (AWI/Rechenzentrum, UB/ZeTeM, Leiter Geschäftsstelle)
- Thorsten Coordes (UB/ZARM)
- Dr. Achim Geleßus (JUB/CLAMV)
- Dr. Natalja Rakowsky (AWI/Rechenzentrum)
- Dr. Dirk Barbi (AWI/Rechenzentrum, bis Juli 2016)

Die Geschäftsstelle ist verantwortlich für die Organisation der Workshops (siehe Abschnitt Veranstaltungen) und die Unterstützung der Nutzer, insbesondere im Antragsverfahren. Das Sekretariat der Geschäftsstelle wird betreut von

- Julitta von Deetzen.

2 Tätigkeitsprofil des BremHLR im Berichtszeitraum

2.1 Unterstützung der HLRN-Nutzung im Land Bremen

Ein Schwerpunkt der Aktivitäten des BremHLR lag auch in diesem Berichtszeitraum in der Unterstützung der HLRN-Nutzung. Neben den Tätigkeiten von Prof. Dr. Wolfgang Hiller als Mitglied der Technischen Kommission sowie Prof. Dr. Alfred Schmidt als Mitglied des Wissenschaftlichen Ausschusses bestand die Unterstützung des HLRN durch das BremHLR hauptsächlich in der Fachberatung für Bremer Projekte am HLRN von der Antragstellung bis zur Begleitung rechenintensiver Projekte während der gesamten Projektlaufzeit.

Eine wesentliche Aufgabe im Berichtsjahr war die weitere Unterstützung der Bremer Nutzer des HLRN bei der effizienten Nutzung des HLRN-III Hochleistungsrechnersystems. Des Weiteren waren Mitglieder des BremHLR an den Vorbereitungen zur Beschaffung des Nachfolgesystems HLRN-IV beteiligt. Das System soll voraussichtlich in 2018 installiert werden, die Beschaffung hat aufgrund der Größe des Rechnersystems aber einige Vorlaufzeit. So wurde zu Beginn des Jahres 2016 der Mittelantrag an den Wissenschaftsrat eingereicht. Nachdem die Mittel bewilligt wurden wurde in der zweiten Jahreshälfte mit der Ausarbeitung der Unterlagen für die EU-weite Ausschreibung begonnen.

2.2 Weitere Aktivitäten des BremHLR

Im Veranstaltungsjahr 2016 wurde vom BremHLR der *11. Workshop zur Einführung in die parallele Programmierung mit MPI und OpenMP* organisiert und durchgeführt. Mit 23 Teilnehmern war dieser Workshop wieder sehr gut besucht.

Der Workshop wurde in der Zeit vom 18. bis zum 22. Januar 2016 an der JUB abgehalten. Als Referent konnte wie bereits bei bisherigen Workshops Dr. Hinnerk Stüben vom Regionalen Rechenzentrum der Universität Hamburg gewonnen werden, der den Workshop gemeinsam mit dem BremHLR-Fachberater Dr. Lars Nerger abhielt. Für die Studenten der JUB wurde der Workshop auch wieder als offizielle Lehrveranstaltung angeboten. Durch die Bearbeitung eines abschließend bewerteten Programmierprojekts konnten die Studenten Kreditpunkte für ihr Bachelor- und Masterstudium erlangen.

Der sehr gute Zuspruch und der große Erfolg der Veranstaltungen zeigt deutlich den dringenden Bedarf zur Ausbildung im Hoch- und Höchstleistungsrechnen und gibt Anlass dazu solche Workshops auch weiterhin als regelmäßige Ausbildungs- und Schulungsmaßnahme anzubieten.

Neben dem Workshop zur Einführung in die parallele Programmierung beteiligten sich Fachberater des BremHLR an Fachberaterworkshops des HLRN-Kompetenznetzwerks in Göttingen und Hamburg. Bei diesen Workshops wurden unterschiedliche Themen des HLRN-Betriebs und der Nutzerbetreuung besprochen. Eine Übersicht über die Veranstaltungen ist in Abschnitt 4 zu finden.

Des Weiteren waren Mitglieder des BremHLR an der Diskussion zu einem HPC-Konzept der Universität Bremen und beratend an der Arbeit der Arbeitsgruppe der GWK zur Einführung eines nationalen Systems für Hochleistungsrechnen (NHR) beteiligt.

3 Statistische Angaben zu den Bremer Höchstleistungsprojekten

Auch im Jahr 2016 wurde der HLRN intensiv durch Bremer Projekte genutzt. Im Jahresdurchschnitt wurde auf dem HLRN-III System ein prozentualer Anteil von 16,1 % an der gesamten am HLRN-III abgenommenen Rechenleistung erreicht. Dieses liegt deutlich über dem investiven Anteil von etwa 3,5% des Landes Bremen am HLRN. Über die gesamte Laufzeit seit Einrichtung des HLRN-Verbunds wurde durch Bremer Projekte ein Anteil von 7,2% der verfügbaren Rechenzeit abgenomen.

Wie schon das Jahr 2015 war auch das Jahr 2016 durch einen stabilen Betrieb des HLRN-III Systems ohne längere Ausfallzeiten geprägt.

Insgesamt wurden im Jahr 2016 etwa 7.700.000 NPL[1] durch Bremer Projekte am HLRN-III System abgenommen. **Dieses ist die größte Nutzung seit Einrichtung des HLRN-Verbunds.** Abbildung 3.1 zeigt den monatlichen Verbrauch der Bremer Projekte an den HLRN-II und HLRN-III Systemen. Deutlich sichtbar ist die starke Zunahme der genutzen Rechenzeit die durch die Verfügbarkeit der zweiten Ausbaustufe von HLRN-III im Jahr 2015 möglich wurde und sich im Jahr 2016 fortgesetzt hat.

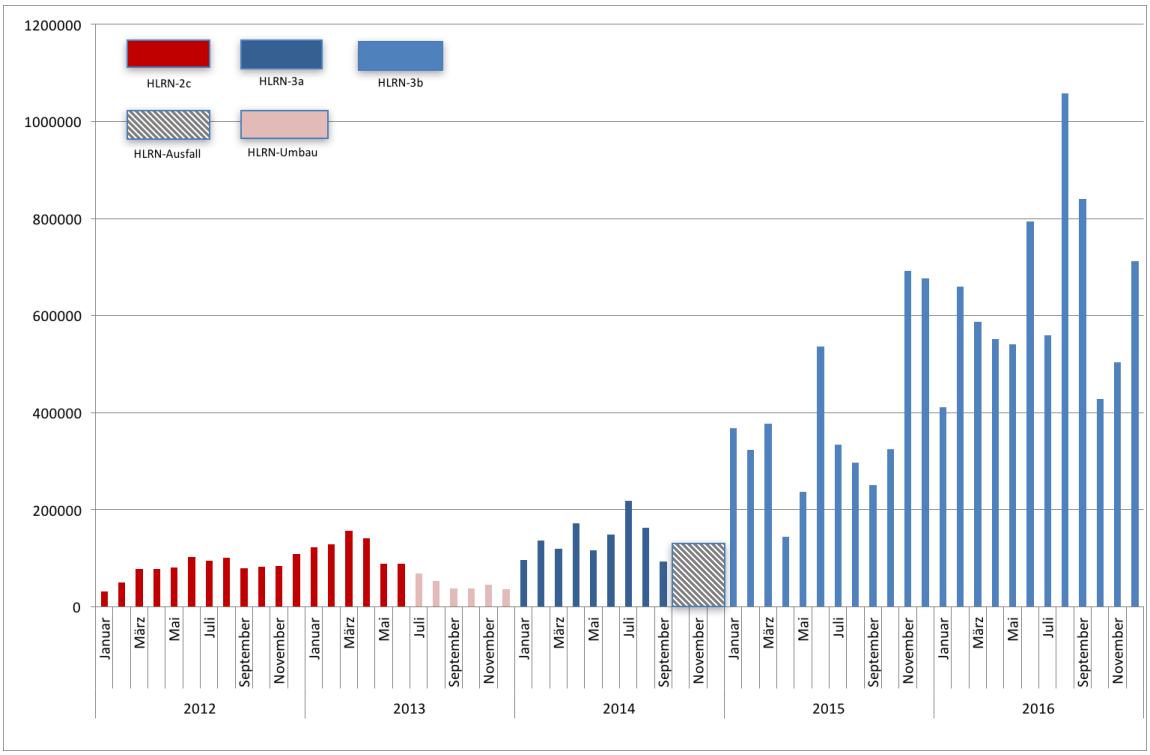

Abbildung 3.1: Monatliche Rechenzeitnutzung der Bremer HLRN-Großprojekte auf den HLRN-II (bis Dezember 2013) und seit Januar 2014 HLRN-III Systemen in der HLRN-Leistungseinheit NPL. Die Farben zeigen die Verfügbarkeit der unterschiedlichen Ausbaustufen der HLRN-Systeme. Von Oktober bis Dezember 2014 waren die HLRN-Systeme nicht bzw. nur teilweise nutzbar. Von Juli bis Dezember 2013 kam es zu Einschränkungen durch den Aufbau des neuen HLRN-III Systems.

[1]Norddeutsche Parallelrechner-Leistungseinheit: Auf den Systemen der ersten Ausbaustufe des HLRN-III entspricht 1 NPL einer halben CPU-h auf einem Knoten mit je 24 Prozessorkernen.

Eine Übersicht zu allen vom BremHLR betreuten Projekten gibt Tabelle 3.1. Im Jahr 2016 wurden vom BremHLR 35 Projekte am HLRN betreut. Die Projekte werden von über 100 akkreditierten Nutzern durchgeführt. 9 neue Projekte mit teilweise sehr großem Rechenzeitbedarf wurden im Jahr 2016 beantragt und vom Wissenschaftlichen Ausschuss des HLRN bewilligt. 11 Projekte wurden im Berichtsjahr beendet.

4 Veranstaltungen mit Beteiligung des BremHLR

11. BremHLR-Workshop *Einführung in die Programmierung mit MPI und OpenMP*

Veranstalter: BremHLR

Datum: 18. – 22. Januar 2016

Ort: Jacobs University Bremen

Beschreibung: In dem Workshop wurden die Grundlagen der parallelen Programmierung vermittelt. Der Schwerpunkt lag auf den Programmiermodellen MPI und OpenMP. Praktische Übungen bildeten einen wesentlichen Teil des Workshops.

Referenten: Dr. Hinnerk Stüben (Regionales Rechenzentrum der Universität Hamburg) und Dr. Lars Nerger (BremHLR).

Teilnehmerzahl: 23

Teilnehmende Institutionen: AWI, JUB, UB (Informatik, MARUM, Physik), FU Berlin, TU Hamburg-Harburg, Uni Hannover, Uni Oldenburg, ZIB

29. HLRN-Fachberater-Workshop

Veranstalter: GWDG Göttingen

Datum: 21. – 22. April 2016

Ort: GWDG Göttingen

Teilnehmerzahl:19

Teilnehmende Institutionen: BremHLR (AWI, ZARM), BTU Cottbus-Senftenberg, Cray, FU Berlin, GWDG Göttingen, HU Berlin, IOW, LUIS Uni Hannover, RRZ Uni Hamburg, TU Braunschweig, TU Clausthal, Uni Kiel, Uni Oldenburg, Uni Rostock, ZIB

30. HLRN-Fachberater-Workshop

Veranstalter: Rechenzentrum der Universität Hamburg

Datum: 9. – 10. November 2016

Ort: Uni Hamburg

Teilnehmerzahl:16

Teilnehmende Institutionen: BremHLR (AWI, ZARM), FU Berlin, GWDG Göttingen, HU Berlin, IOW, RRZ Uni Hamburg, Sternwarte Uni Hamburg, TU Hamburg, Uni Kiel, ZIB

Tabelle 3.1: Übersicht der Bremer HPC-Projekte, die innerhalb des Berichtszeitraums vom BremHLR betreut wurden. Status: F = Fortsetzung, E = Erstantrag; NPL: Kontingent in NPL im Jahr 2015

Kennung	Projektleiter	Institut	Laufzeit	NPL	Status
hbc00012	Prof. Dr. L. Colombi-Ciacchi	UB/BCCMS	IV/12 – I/17	234370	F
hbc00013	Dr. J. Larrucea	UB/BCCMS	IV/12 – I/17	242140	F
hbc00014	Prof. Dr. L. Colombi-Ciacchi	UB/BCCMS	IV/13 – III/16	240700	F
hbc00015	Dr. M. Fischer	UB/FB 5	II/15 – I/16	29450	E
hbc00016	Dr. S. Köppen	UB/BCCMS	II/15 – I/16	9790	E
hbc00017	Prof. Dr. P. Deák	UB/BCCMS	IV/15 – IV/16	155230	F
hbc00018	Dr. L. Moskaleva	UB/Chemie	I/16 – IV/16	302850	E
hbc00020	Dr. M. Delle Piane	UB/BCCMS	III/16 – II/17	80000	E
hbi00024	Dr.-Ing. R. Groll	UB/ZARM	II/14 – II/17	196910	F
hbi00026	Dr.-Ing. R. Groll	UB/ZARM	II/15 – I/17	15910	F
hbi00027	Dr.-Ing. R. Groll	UB/ZARM	IV/15 – II/17	156000	F
hbi00030	Dr.-Ing. R. Groll	UB/ZARM	II/16 – I/17	90000	E
hbi00032	Dr.-Ing. R. Groll	UB/ZARM	III/16 – II/17	80000	E
hbk00018	Dr. K. Weigel	UB/IUP	I/11 – III/17	272310	F
hbk00028	Prof. Dr. P. Lemke	AWI & UB	IV/11 – I/17	87870	F
hbk00032	Prof. Dr. T. Jung	AWI & UB	II/12 – II/17	1598640	F
hbk00034	Prof. Dr. T Kanzow	AWI & UB	III/13 – III/17	1256760	F
hbk00038	Prof. Dr. T. Kanzow	AWI & UB	III/14 – II/17	150000	F
hbk00040	Prof. Dr. T. Jung	AWI & UB	III/14 – II/16	12080	F
hbk00042	Prof. Dr. G. Lohmann	AWI & UB	I/15 – IV/17	446840	F
hbk00044	Prof. Dr. T. Jung	AWI & UB	II/15 – II/17	397440	F
hbk00045	Dr. A. Rozanov	UB/IUP	IV/15 – II/17	342550	F
hbk00046	Prof. Dr. A. Bracher	AWI & UB	IV/15 – III/16	51000	E
hbk00055	Prof. Dr. A. Bracher	AWI & UB	III/16 – II/17	100000	E
hbk00056	Prof. Dr. M. Schulz	UB/MARUM	III/16 – II/17	244000	E
hbp00003	Prof. Dr. C. Lämmerzahl/ Prof. Dr. S. Rosswog	UB/ZARM	IV/10 – IV/16	200000	F
hbp00021	Dr. L.-M. Yang	UB/BCCMS	IV/14 – I/16	20	F
hbp00024	Prof. Dr. T. Wehling	UB/Physik	IV/14 – IV/16	44580	F
hbp00027	Dr. L. Zhou	UB/BCCMS	I/15 – I/16	2740	E
hbp00028	Prof. Dr. T. Frauenheim	UB/BCCMS	III/15 – II/17	148000	F
hbp00029	Dr. M. Lorke	UB/Physik	IV/15 – I/17	445114	F
hbp00030	Prof. Dr. T. Wehling	UB/Physik	IV/15 – III/17	165940	F
hbp00034	Dr. B. Shao	UB/BCCMS	I/16 – I/17	160040	E
hbp00035	Prof. Dr. C. Lämmerzahl	UB/ZARM	I/16 – IV/17	121630	F
hbp00038	Dr. M. Lorke	UB/Physik	II/16 – I/17	80020	E

5 Informationen zur Infrastruktur: Das HLRN-III System im Endausbau

Das HLRN-III System wurde im September 2013 mit der ersten Ausbaustufe in Betrieb genommen und für die Nutzer geöffnet. Die zweite Ausbaustufe wurde ab September 2014 installiert und hat die verfügbare Rechenleistung um einen Faktor von etwa 3 vergrößert. Das HLRN-III System ist ein massiv paralleler (MPP) Hochleistungsrechner der Typen Cray XC30 und XC40. Ferner sind in Hannover 64 Rechenknoten des Herstellers MEGWARE mit großem Hauptspeicher installiert.

Das MPP-System Cray XC30 der ersten Ausbaustufe besteht pro Standort aus:

- 744 Dual-Socket Knoten, jeweils mit Intel Xeon IvyBridge (E5-2695v2) Prozessoren mit 2,4 GHz Taktung und jeweils 12 Prozessorkernen
- 17856 Prozessorkerne pro Standort
- 64 GB Hauptspeicher pro Knoten (46,5 TByte Gesamtspeicher)
- Netzwerk: Cray Aries Interconnect mit Dragonfly Topologie
- Peak-Performance: 342,8 TFlop/s
- 1,4 PB paralleles Lustre-Dateisystem (“WORK” zur Speicherung von Simulationsdaten) über FDR Infiniband-Netzwerk
- 0,5 PB Heimat-Dateisystem angebunden an die Knoten per NFS über 10 Gigabit-Ethernet Netzwerk.

Die MPP-Systeme Cray XC40 der zweiten Ausbaustufe sind pro Standort leicht unterschiedlich ausgebaut:

- Rechenknoten:
  - Berlin: 1128 Dual-Socket Knoten, jeweils mit Intel Xeon Haswell (E5-2680v3) Prozessoren mit 2,4 GHz Taktung und jeweils 12 Prozessorkernen
  - Hannover: 936 Dual-Socket Knoten, jeweils mit Intel Xeon Haswell (E5-2680v3) Prozessoren mit 2,4 GHz Taktung und jeweils 12 Prozessorkernen
- Gesamtanzahl Prozessorkerne:
  - Berlin: 27072 Prozessorkerne
  - Hannover: 22464 Prozessorkerne
- 64GB Hauptspeicher pro Knoten:
  - Berlin: 117 TByte Gesamtspeicher
  - Hannover: 105 TByte
- Netzwerk: Cray Aries Interconnect mit Dragonfly Topologie
- Peak-Performance:
  - Berlin: 1,1 PFlop/s
  - Hannover: 0,9 PFlop/s
- 2,3 PB paralleles Lustre-Dateisystem (“WORK” zur Speicherung von Simulationsdaten) über FDR Infiniband-Netzwerk

In Hannover wurden zusätzlich in der ersten und zweiten Ausbaustufe SMP-Systeme der Firma Megware mit großem RAM-Speicher installiert. Sie bestehen aus

- 1. Ausbaustufe:
  - 32 Quad-Socket Knoten mit Intel Xeon SandyBridge (E5-4650) Prozessoren mit 2,7 GHz Taktfrequenz und jeweils 8 Prozessorkernen
  - 256 GB Arbeitsspeicher pro Knoten
- 2. Ausbaustufe:
  - 32 Quad-Socket Knoten mit Intel Xeon IvyBridge (E5-4650v2) Prozessoren mit 2,4 GHz Taktfrequenz und jeweils 10 Prozessorkernen
  - 512 GB Arbeitsspeicher pro Knoten
- Dual FDR Infiniband Netzwerk

In der Top500 Liste der weltweit schnellsten Supercomputer vom November 2016 befinden sich die beiden MPP-Systeme auf den Plätzen 118 und 150. In Deutschland finden sich die beiden Systeme auf den Plätzen 9 und 12.

Abbildung 5.1: Frontansichten der Cray XC30/XC40 Systeme nach der zweiten Ausbaustufe des HLRN-III. Oben: System „Konrad“ am ZIB in Berlin; unten: System „Gottfried“ an der Universität Hannover

6 Projektberichte[2]

6.1 HLRN Projects of the Hybrid Materials Interfaces Group (HMI)

Technical Details:

HLRN Project ID: **hbc00012**

Title: All-atom moleculardynamic investigations of the adhesion mechanisms at the contact interface of TiO_2 nanoparticles in films and aggregates

Run time: IV/2012 – I/2017

Project Leader: Prof. Dr. Lucio Colombi Ciacchi

Project Scientists: Jens Laube, Valentin Baric, Dr. Julian Schneider

HLRN Project ID: **hbc00013**

Title: Fabrication of multishaped magnetic structures via a knowledge based biomimetic approach

Run time: IV/2012 – I/2017

Project Leader: Dr. Susan Köppen

Project Scientists: Steffen Lid

HLRN Project ID: **hbc00014**

Title: Molecular Dynamic Simulations of the Adsorption of Lysozyme and Chymotrypsin on Silica and Titania

Run time: IV/2013 – III/2016

Project Leader: Prof. Dr. Lucio Colombi Ciacchi

Project Scientists: Nils Hildebrand, Dr. Susan Köppen, Simon Kunze, Johannes Stoedter

[2] Für den Inhalt der Projektberichte sind ausschließlich die genannten Projektleiter bzw. die Projektbearbeiter verantwortlich.

HLRN Project ID: **hbc00020**

Title: Silica: both friend and foe. Is molecular regognition the answer?

Run time: III/2016 – II/2017

Project Leader: Dr. Massimo Delle Piane

Project Scientists: Prof. Dr. Lucio Colombi Ciacchi, Dr. Jens Laube

Affiliation: Hybrid Materials Interfaces Group, Bremen Center for Computational Materials Science, Faculty of Production Engineering, University of Bremen, Germany

hbc00012: All-atom moleculardynamic investigations of the adhesion mechanisms at the contact interface of TiO_2 nanoparticles in films and aggregates

Overview:

Aggregated nanoparticle films show promising results in many applications, including catalysis and gas sensors. The nanoparticle films can provide a high specific surface area for chemical reactions and a pore structure, suitable to provide access for gas molecule to diffuse to these adsorption sites.

However, this highly porous structure often comes with a low mechanical stability. To fully understand the interplay of these properties that determine the mechanical properties of the film, it is important to understand the interactions on the smallest scale, the individual primary particles. However, the experimental investigation remains difficult, therefore the goal of this project is to apply simulations based on all-atom molecular dynamics to provide these informations.

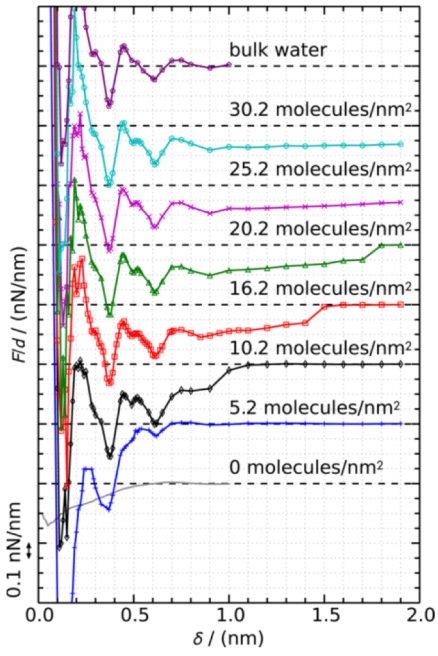

Fig 1: Force−displacement curves calculated for 4 nm TiO2 particles facing each other along the (110) direction with different numbers of adsorbed water molecules. The curves are shifted along the y axis with respect to their respective zero-force lines (dashed) and divided by the particle diameter d.

Latest Results:

This project is running in its third extension on the HLRN. In the first phases of this project the interactions between two individual TiO_2 nanoparticles in a humid environment have been investigated [1]. It was found that the forces can be described using the combination of humidity dependent capillary and humidity independent solvation forces. The linear superposition approximation of the two water structures over the single particle surfaces led to the

oscillatory solvation forces between two particles. This was combined with a modification of the continuum capillary forces to account for the adsorbed water layer.

In the latest project phase a coarse grained model was derived to implemented the force-distance curves into discrete element methods to be able to simulate whole particle films. The humidity was chosen to match thermogravimetric analyses of flame-sprayed TiO_2 [1], however it can be adjusted to match the individual application (fig 1). The capillary forces were approximated by consideration of the circular approximation to represent the meniscus and the Kelvin equation to calculate the pressure within the liquid bridge. This was superimposed by the solvation forces, represented by a semi-empirical decaying cosine function and a hertz model implemented in LIGGGHTS. Furthermore, the friction forces were parameterized by the application of atomistic simulations.

Particles under a defined particle load were dragged over a surface from which friction coefficients as well as damping coefficients for rolling and sliding friction were derived. These values have also been implemented into the discrete element method simulations to provide rolling and sliding friction models, respictively.

Outlook:

In the present and further application periods, the developed interaction potentials implemented into discrete element methods will be used to throroughly investigate particle films. Therefore, existing particle formation models will be used to provide porous nanoparticle structures that represent nanoparticle films prepared by flame spray pyrolysis [2]. The derived interaction potentials help to examine the particle structure properties that determine the mechanical stability of particle films, such as particle size distribution, porosity and pore size distribution. The results will help to design nanoparticle films with a high mechanical stability while preserving crucial particle film features, such as pore structure and specific surface area.

hbc00013: Fabrication of multishaped magnetic structures via a knowledge-based biomimetic approach

Overview:

In complex hybrid systems, the description of the constituent parts sometimes has to be done from scratch. In the project first two application periods of **hbc00013** an intermolecular force field for the FeO(OH) – water interface and an intramolecular force field for a Ferrihydrite structure had to be established to describe the interaction of iron oxide clusters with ferritin subunits.

With the developed force field, significant larger systems of FeO(OH) clusters and Ferritin subunits could be treated [3]. As a next step, simulations in which the subunit arrangements around the iron oxide cluster were fixed on a substrate material. A first outcome of the simulations is the change of the used carrier material due to higher interaction forces of the ferritin subunits on silica with respect to alumina surfaces. The stepwise evaluation of the

multishaped magnetic structure model is almost completed now and in the running period, the focus is set on the crystal growth of the iron oxyhydroxide phase.

Latest Results:

This project is running in its third extension on the HLRN. Based on our preliminary classical intra- and intermolecular force fields (FF) [4] developed in the first to application periods, crystal growth simulation of iron oxyhydroxides are in the focus of the present project. These simulations based on the Kawska-Zahn approach [Ref. 1] which combines a Monte-Carlo type scheme for the adsorption sites and structural optimization of the ion cluster cluster after individual growth steps.

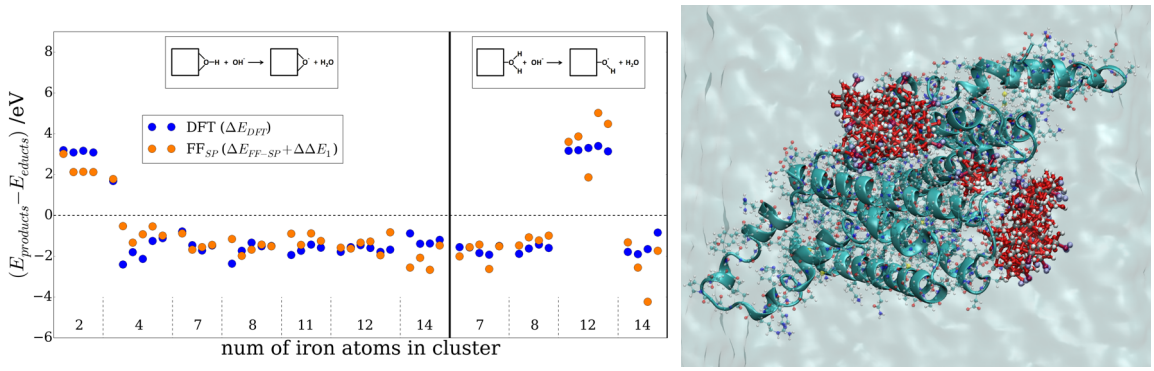

Fig. 2 (left) DFT and FF based energy differences of possible PT reactions for different sized iron oxyhydroxide clusters. A estimated energy correction term is added to all FF based energies. (right)

An important part of this simulation is the treatment of proton transfer (PT) reactions to receive more realistic crystals. Density Functional Theory (DFT) based calculations of different sized clusters before and after possible PT reactions have to be performed first. The energy difference between educts and products provides the possibility to easily decide whether the respectively reaction takes place or not. Nevertheless, the enormous number of simulations necessary to sample the crystal growth slows down the insight into the growth mechanism drastically. In the present application period a lot of effort was put into the speed up the simulation scheme.
Different possibilities to describe these reactions by our further developed classical FF were evaluated. Finally we are able to reproduce the DFT based energies for products and educts of possible PT reactions by classical FF based calculations by adding an energy correction term to all FF reactions (Fig. 2, left) [5]. Based on this groundwork crystal growth simulations of iron oxyhydroxides in water and on Ferritin subunits are started and a received crystal which grew in water is represented in Fig. 2 (right).
The next and last step of the present project is the crystal structure determination of the received structures as well as the investigation of structural changes.

Ref. 1: A. Kawska, J. Brickmann, O. Hochrein, D. Zahn, “From Amorphous Aggregates to Crystallites: Modelling Studies of Crystal Growth in Vacuum”, Z. Anorg. Allg. Chem. 631, 1172-1176, 2005

hbc00014: Molecular Dynamic Simulations of the Adsorption of Lysozyme and Chymotrypsin on Silica and Titania

Overview:

The goal of this project is the development and evaluation of simulation methods to analyze the protein adsorption process on oxide surfaces used e.g. in carrier systems or nanotechnology medical applications.

Latest Results:

This project is running in its second extension on the HLRN. The first phase of the project included the development of methods to identify binding motifs of proteins on surfaces [6]. Chymotrypsin as an example protein adsorbs in a very distinct way with its helix structure towards the negatively charged silica surface (Fig. 3 a). Direct surface contacts are predominantly positively charged and polar amino acids. In this case, the adsorption is dominated by the dipole moment of the protein. Further investigations of other proteins and surfaces reveal crucial effects on the adsorption process such as the protein dipole value, multi-protein influences and the hydration shell around the oxide and protein surface [7].

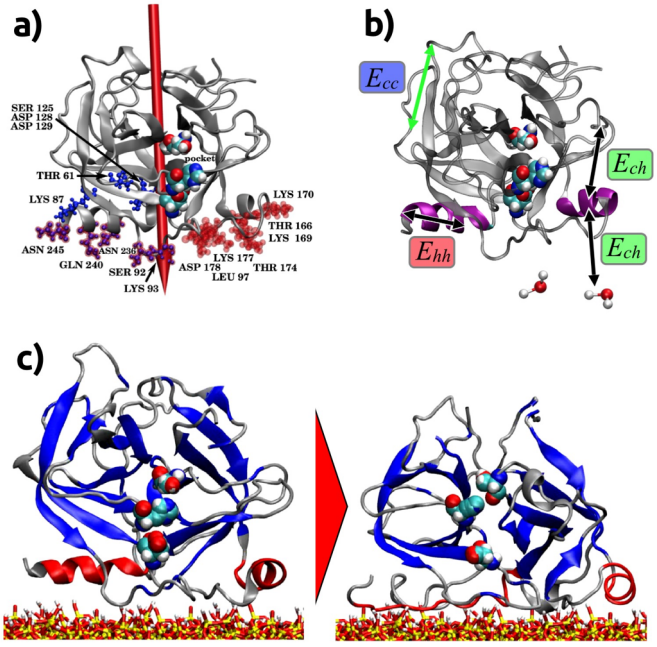

Fig 3: a) Identified binding motifs of chymotrypsin on a silica surface with the protein dipole moment shown in red. b) Development of an advanced molecular dynamics free energy sampling method for an accelerated simulation of one part of a macromolecule. c) Application of the developed methods to the surface-induced conformational change of chymotrypsin on silica.

The usage of a protein functionalized technical surface also requires the preserved activity of the protein. It is assumed that the activity is directly related to the surface-induced denaturation of the protein. Therefore, we have developed a method to investigated the protein conformational change on one specific part of a protein (Fig. 3 b). This free energy sampling method allows the calculation of the free energy landscape along a chosen collective variable [Ref. 2]. We have applied this method to investigate the helicity change of chymotrypsin during adsorption (Fig. 3 c).

Outlook:

The developed methods model the complete protein adsorption process and enable direct access to an atomistic resolution of this process. The procedure can easily be transferred to any investigations of the interaction of micro- and macromolecules. Further steps in the project include the application of these methods to another protein - surface system and to study the atomistic interactions in a ceramic based virus - filtration system.

Ref. 2: R.H Meißner, J. Schneider, P. Schiffels, L. Colombi Ciacchi, *Computational prediction of circular dichroism spectra and quantification of helicity loss upon peptide adsorption on silica* Langmuir 30, 3487-3494 (2014)

hbc00020: Silica: both friend and foe. Is molecular regognition the answer?

Overview

The interaction of silica with biological systems is complex and contradictory: it is at the basis of many biomineralization processes and, at the same time, some forms of silica induce toxic effects at the cellular level. It has been suggested that silica behavior is dependent on the interaction between epitopes of the cellular membranes with specific patterns on the silica particles' surface.This project aim is to investigate these interactions using all-atom MD simulations, coupled to techniques that enable a computational prediction of free energy profiles across hybrid interfaces.

Current results

This project is currently running in its first application period. So far, realistic models of cell membranes of various compositions up to a realistic erythrocyte cell membrane, together with both fumed and colloidal silica nanoparticles models (Fig. 4) were built. Free energy profiles of some of these models across the membranes could be predicted, to achieve an atomistic picture of the interactions between different types of silica and the membrane of erythrocytes.

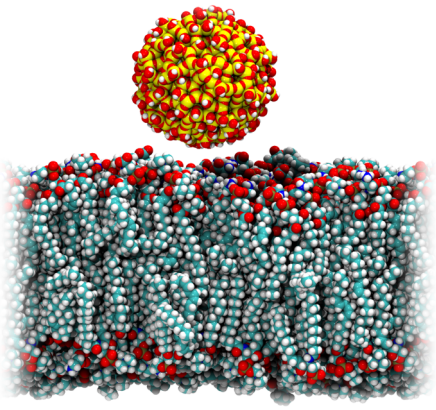

Fig. 4: Silicon oxide nanoparticle on a phospholipid bilayer model

Outlook

We plan to simulate the interaction of silica agglomerates with increasing size with the membrane, trying to determine at which nuclearity the segregation at the membrane/water interface takes place, investigating the energetics of adsorption or translocation.

Publications

1. Laube, J., Salameh, S., Kappl, M., Mädler, L., & Colombi Ciacchi, L. (2015). *Contact Forces between TiO_2 Nanoparticles Governed by an Interplay of Adsorbed Water Layers and Roughness*. Langmuir, 31(41), 11288–11295. http://doi.org/10.1021/acs.langmuir.5b02989

2. Mädler, L., Lall, A. A., & Friedlander, S. K. (2006). *One-step aerosol synthesis of nanoparticle agglomerate films: simulation of film porosity and thickness*. Nanotechnology, 17(19), 4783–4795. http://doi.org/10.1088/0957-4484/17/19/001

3. S. Lid, L. Colombi Ciacchi, *FeO(OH) particles and characteristic Ferritin binding sites: a theoretical investigation*, to be submitted

4. J. Larrucea, S. Lid, L. Colombi Ciacchi (2014) *Parametrization of a classical force field for iron oxyhydroxide/water interfaces*; *Comp. Mat. Sci.* 92, 343-352

5. S. Lid, T. Kollmann, D. Zahn, L. Colombi Ciacchi, *Molecular mechanisms of crystal nucleation and growth at ferritin/oxide interfaces: a theoretical investigation*, to be submitted

6. Hildebrand, N.; Köppen, S.; Derr, L.; Li, K.; Koleini, M.; Rezwan, K.; Colombi Ciacchi, L., *Adsorption orientation and binding motifs of lysozyme and chymotrypsin on amorphous silica.* The Journal of Physical Chemistry C 119, 7295-7307 (2015)

7. L. Derr, N. Hildebrand, S. Köppen, S. Kunze, L. Treccani, R. Dringen, K. Rezwan, L. Colombi Ciacchi, *Physisorption of α-chymotrypsin on SiO_2 and TiO_2: A comparative study via experiments and molecular dynamics simulation*s, Biointerphases 11, 011007 (2016)

Funding:

The project **hbc00012** will be worked out within the framework of the DFG priority program SPP 1486 "Partikel im Kontakt (PIKO) -Mikromechanik, Mikroprozessdynamik und Partikelkollektive". The project **hbc00013** is embedded within the framework of the DFG priority programme SPP 1569, entitled: “Generation of multifunctional inorganic materialsby molecular bionics”. The project **hbc00014** is funded by the DFG with the project ID: KO3811/3-1 and is entitled “Theoretical investigation of the adsorption of lysozyme on different oxide materials forthe development of antibacterial hybrid materials”. The HLRN provides computational resources for several projects in the hybrid materials interfaces group in the **magnitude of 2000 kCPU - hours/year**.

6.2 *hbc00015:* Structure and dynamics of ammonium cations in NH_4-exchanged zeolites

HLRN Project ID:	hbc00015
Run time:	II/2015 – I/2016
Project Leader:	Dr. Michael Fischer
Project Scientists:	Dr. Iris Spieß, Prof. Dr. Reinhard X. Fischer
Affiliation:	Fachgebiet Kristallographie, Fachbereich Geowissenschaften, Universität Bremen

Overview

In this project, the behavior of ammonium cations (NH_4^+) in zeolites is studied with molecular dynamics calculations based on density-functional theory (DFT). A particular emphasis is placed on the development of an atomistic explanation for the observed instability of NH_4-exchanged zeolite LTA towards deammoniation.

Introduction

Zeolites are crystalline inorganic materials with intrinsic porosity that have found a number of technological applications, e.g. in catalysis, adsorption, and ion exchange. Structurally, zeolites consist of a three-dimensional framework of tetrahedrally coordinated atoms (T atoms, primarily silicon and aluminium), which are connected by oxygen atoms. More than 200 different zeolite frameworks have been reported to date, with each topologically distinct system being designated by a three-letter code like LTA, FAU, or RHO. In most cases, the zeolite framework is negatively charged, and extra-framework cations balance the charge.

Ammonium-exchanged zeolites (NH_4-zeolites) are of particular interest as precursor materials for the production of protonated zeolites (H-zeolites). H-zeolites are very important catalysts that are employed on an industrial scale in a variety of processes, e.g. in the fluid catalytic cracking of heavier oil fractions to produce lighter hydrocarbons.[1] The crystal structures of approximately twenty NH_4-zeolites with distinct framework topologies have been reported.[2] It has been found that structurally different systems differ considerably in their behaviour upon the removal of the ammonium cations from the structure (deammoniation): For example, deammoniation of NH_4-RHO at high temperatures produces highly crystalline H-RHO,[3] whereas fully ammonium-exchanged LTA is unstable towards deammoniation.[4]

Motivation and computational approach

Experimental efforts in our group aim at a detailed characterisation of the deammoniation behaviour of partially and fully ammonium-exchanged LTA as well as some other NH_4-zeolites. The portfolio of experimental methods comprises X-ray diffraction using single crystal and powder samples, thermal analysis, and spectroscopic measurements. The investigations performed in the context of the PhD thesis of Dr. Li Wang, completed in autumn 2016, have corroborated the previously observed instability of NH_4-LTA towards deammoniation:[5] Both in air and in vacuum, amorphisation occurs already at temperatures slightly above room temperature (between 50 and 100 °C). A weight loss that is attributed to concurrent deammoniation and dehydration occurs in the same temperature range. In

contrast, hydrated potassium-exchanged LTA (K-LTA) can be dehydrated without appreciable loss in crystallinity, being stable up to temperatures of ~900 °C.

Since none of the experimental methods can deliver direct insights into the structural changes that occur upon deammoniation, computational chemistry methods were used in this project to develop an atomic-level understanding of the underlying processes. The calculations were performed in the framework of density-functional theory (DFT). DFT has developed into a powerful and versatile electronic structure method that is particularly well suited for the treatment of periodic systems. With efficient DFT codes like the program CP2K, which was used in this project, systems that contain thousands of atoms per unit cell can be treated on high-performance computing facilities.[6]

The calculations carried out within the project focused on zeolites LTA and RHO. The structure of LTA contains larger *grc* cages, connected by windows formed of eight T atoms (eight-ring windows), and smaller *toc* (sodalite) cages, bordered by six-ring windows. In zeolite RHO, *grc* cages are connected by double-eight-ring units (Fig. 1). For the case of LTA, fully ammonium-exchanged LTA (NH_4-LTA) and a (hypothetical) fully protonated H-LTA were considered. For H-LTA, the energetically most favourable proton position was determined from structure optimisations of different models (the oxygen atom to which the proton is attached is referred to as O_H). Furthermore, K-LTA was included as reference system. Calculations for zeolite RHO consideredammonium-exchanged and protonated zeolite models (NH_4-RHO and H-RHO). For each system, DFT structure optimisations were performed for systems with and without adsorbed water molecules. These were followed by DFT-based Molecular Dynamics (MD) calculations for temperatures of 100 K, 298 K, and 500 K (total duration 5 ps, timestep 0.5 fs).

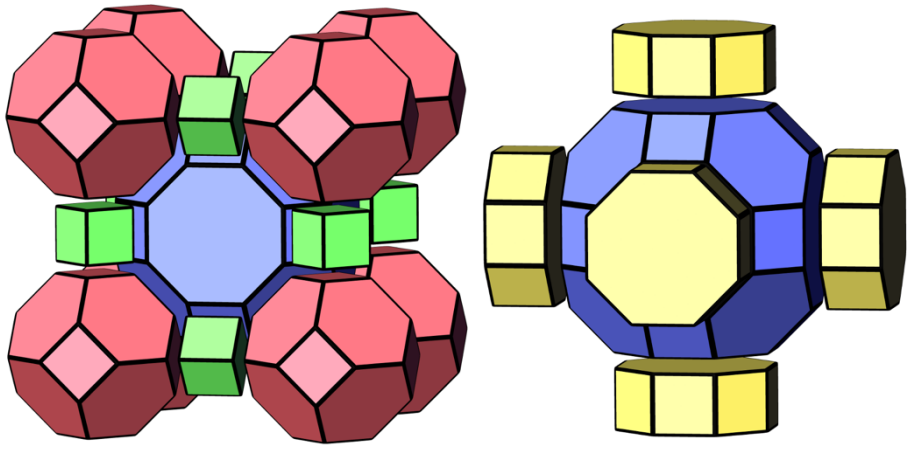

Fig.1: Natural tiling representation of LTA (left) and RHO (right) frameworks. The *grc* cages are shown in blue, *toc* cages are shown in red, double four-ring units are green and double eight-ring units are yellow. The full unit cell of LTA used in the simulations contains a 2x2x2 array of *grc* cages.

Results

MD simulations for water-free models of NH_4-LTA and NH_4-RHO revealed a much higher mobility of the cations in the former system: While the ammonium cations in NH_4-RHO mainly oscillate about their equilibrium positions, the cations in NH_4-LTA exhibit a larger freedom of movement. During the simulation run performed for the highest temperature (500 K), some of the ammonium cations in NH_4-LTA dissociate into a framework proton and an ammonia (NH_3) molecule. Such dissociation constitutes the first step of deammoniation,

which would then be followed by the diffusion of ammonia molecules out of the structure (however, this second step is not accessible with the current modelling strategy). In NH_4-RHO, no dissociation was observed at the timescale of the simulation, even at a temperature of 500 K. This is in accordance with the rather high temperatures needed for the deammoniation of this material (which are in the range of 700 to 1000 K).[3]

In the simulations for water-free models of LTA, no breaking of T-O bonds (intra-framework bonds) was observed throughout the MD simulations: The T-O bond lengths oscillate about their equilibrium value due to thermal motion, but no exceptionally large elongation occurs. Even at an elevated temperature of 500 K, the water-free form of H-LTA should be stable according to the MD simulations. At first sight, this observation appears to be in disagreement with the experimentally observed instability of NH_4-LTA towards deammoniation. However, it has to be considered that an as-synthesised sample of NH_4-LTA will also contain water, and that the presence of water might promote the amorphisation upon ammonia removal. To study the effect of water in more detail, additional MD simulations were run for models of K-LTA, NH_4-LTA, and H-LTA with 96 water molecules per unit cell (equivalent to 12 molecules per *grc* cage). For K-LTA and NH_4-LTA, no breaking of intra-framework bonds was observed. For H-LTA, the first set of simulations was run for a model in which water is located exclusively in the large *grc* cages. Again, no unusual elongation of the T-O bonds occurred. However, simulations for a second model, in which some of the water molecules were placed in the smaller *toc* cages, showed a completely different behavior: Here, some of the water molecules inside the *toc* cages coordinate to framework aluminium atoms. Concomitantly, one of the Al-O intra-framework bonds, more specifically the bond to the oxygen atom that carries the framework proton (Al-O_H bond), is strongly elongated. In many cases, the Al-O_H distance becomes so large that the bond can be considered as broken. The breaking of Al-O_H bonds is accompanied by a reorientation of the framework proton, which tends to form an intra-framework hydrogen bond. A representative example is shown in Fig. 2. As is visible in the figure, the whole structural environment is strongly distorted after the coordination of water to aluminium has occurred. This distortion can be interpreted as the very onset of the amorphisation of the structure, which would be observed on a longer timescale. In addition to these qualitative observations, an analysis of the radial distribution function (RDF) of Al-O distances provides a more quantitative way to analyse the coordination of water to framework Al atoms (Fig. 2, right).

While the MD simulations cannot model the full process of the structural decomposition of NH_4-LTA upon deammoniation, a model that is based on two central steps can be proposed from the calculations:

1) Initially, some of the NH_4 cations dissociate into framework protons and ammonia molecules. The presence of framework protons is a prerequisite for step 2.
2) If water is present in the small *toc* cages, some of the water molecules will coordinate to framework aluminium atoms, provided that these are also bonded to an O_H oxygen atom. Upon formation of the H_2O-Al bond, the Al-O_H bond is broken, leading to severe structural distortions and, eventually, collapse of the long-range order.

With increasing temperature, the increased motion of the extra-framework species makes both steps more probable, explaining – at least qualitatively – the observed amorphisation of NH_4-LTA upon heating to relatively mild temperatures.

In zeolite H-RHO, no significant elongation of the intra-framework bonds was observed, even in the presence of 12 water molecules per unit cell. This finding points to a rather high stability of the deammoniated zeolite, in line with experimental observations.

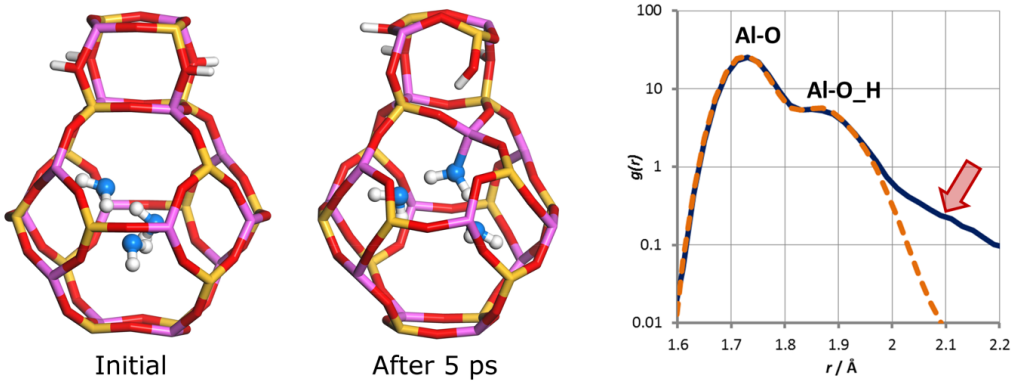

Fig. 2: *Left:* Visualisation of a water-containing *toc* cage in H-LTA at the beginning of an MD run and after a run of 5 ps. The coordination of one water molecule to a framework Al atom, with the concomitant breaking of the Al-O_H bond and reorientation of the framework proton, is clearly visible in the upper right-hand corner of the cage. *Right:* Radial distribution function of Al-O distances obtained from MD simulations (T = 298 K) for H-LTA with 96 water molecules per unit cell, with water occupying only the *grc* cages (orange) or water in *grc* and *toc* cages (blue). The occurrence of elongated Al-O distances in the latter case, highlighted by a red arrow, reflects the coordination of water to framework Al atoms and the concurrent elongation of Al-O_H bonds. To highlight this, a logarithmic scale is used for the y-axis.

Outlook

In addition to the different topology of LTA and RHO, the models used for the two zeolites also have different Si:Al ratios. While the LTA models contain equal amounts of silicon and aluminium, RHO has an Si:Al ratio of 3:1. Therefore, H-LTA contains a considerably larger number of protons (per formula unit) than H-RHO. The present study points to a crucial role of the topology, as only water molecules confined to the small toc cages in LTA are observed to coordinate to framework Al atoms. However, an additional impact of the Si:Al ratio cannot be ruled out on the basis of the present results. Therefore, the inclusion of a series of models of LTA with different Si:Al ratios could be envisaged for future work.

Originally, it was also planned to extend the present study to other ammonium-exchanged zeolites that are currently investigated in our lab (chabazite, merlinoite). However, difficulties in the experimental structure determination have prevented their inclusion in this proect.

Presentations

I. Spieß, M. Fischer, L. Wang, W. H. Baur, R. X. Fischer, *Crystallographic characterization and thermal decomposition behavior of ammonium exchanged zeolites*, presented at the 24th Annual Meeting of the German Crystallographic Society (DGK), Stuttgart, March 2016

References

(1) Rabo, J. A.; Schoonover, M. W. *Appl. Catal. A Gen.* **2001**, *222*, 261–275.
(2) Baur, W. H.; Fischer, R. X. *Zeobase, a new kind of structure database*, in *Proc. 16th Int. Zeolite Conf.*; De Frede, A. (ed.); Sorrento, Italy, 2010; p 457.
(3) Fischer, R. X.; Baur, W. H.; Shannon, R. D.; Staley, R. H.; Vega, A. J.; Abrams, L.; Prince, E. *J. Phys. Chem.* **1986**, *90*, 4414–4423.
(4) Kühl, G. H. *J. Catal.* **1973**, *29*, 270–277.
(5) Wang, L. *Crystal-chemical studies of cation-exchanged zeolite A,* PhD thesis, University of Bremen, **2016**.
(6) Hutter, J.; Iannuzzi, M.; Schiffmann, F.; VandeVondele, J. *WIREs Comput. Mol. Sci.* **2014**, *4*, 15–25.

6.3 *hbc00017:* Simulating Local Phenomena in and on Solids at the Atomic Level

Modeling charge-carrier assisted reactions on the surface and in the bulk of transition metal oxides

HLRN Project ID:	hbc00017
Run time:	IV/15 – III/16
Project Leader:	Prof. Dr. P. Deák
Project Scientists:	P. Deák, B. Aradi, Quoc Duy Ho
Affiliation:	Bremen Center for Computational Materials Science, University of Bremen

In Short

- Developing electron self-interaction corrections for the proper description of small polaron states in wide band gap materials.
- Development and programming of a correction scheme for periodic low-dimensional charged systems.
- Simulation of photocatalytic oxidation/reduction of CO_x and NO_x species on anatase-TiO_2
- Calculation of defect reactions in and water splitting on β-$Ga_2\ O_3$
- Defect studies in CuGa(In)$S(Se)_2$solar cell materials.
- Investigation of the electronic phase transition in VO_2(B).

Our project (hbc00017) is a continuation of earlier work (hbc00001, hbc00011) on highly accurate theoretical simulation of defects in/on solids at the atomic level. The present project concentrates primarily on wide band-gap (WBG) transition metal oxides. These materials have a wide range of practical applications but cannot be well described by the standard local and semi-local approximations of density functional theory (DFT), which have been the work horse of theoretical solid state physics for electronic structure calculations in the past decades. Therefore, our work encompasses -- beside simulations for practical purposes -- also method development and testing.

One of the methodical problems we are considering is the inclusion of self-energy correction into DFT for calculations on supercells with hundreds of atoms. We have shown that the error compensation between semi-local (GGA) and non-local (Hartree-Fock) exchange makes the screened hybrid functional HSE06 (of Heyd, Scuseria and Ernzerhof) almost self-interaction free in TiO2 (see [1] and references therein). Unfortunately this is not the case in many other WBG materials. In the first year of the project we have shown that following proper theoretical guidelines in selecting the parameters of an HSE hybrid, the electronic structure can very accurately be reproduced in materials where the screening is weakly orbital- and direction-dependent. We have demonstrated this on β-Ga2O3, providing also for

the first time a consistent interpretation of the experimental spectra of defects in this important material [2], which is being considered (among others) as a transparent electrode but also as photo-electrode for water splitting. In the continuation of the project, we would like to prove the efficiency of our method for other WBG materials, like $CuGa(In)S(Se)_2$, used in thin film solar cells. At the same time, since HSE calculations for surfaces are much too costly even on a supercomputer, we are developing "low-budget" corrections to standard semi-local (GGA) DFT calculations, which satisfy at least approximately the criteria used in parameterizing the hybrids. In the first year, we have done this for the (101) surface of anatase- TiO_2 and succeeded in describing small electron- and hole-polaron states, localized either in the bulk or on the surface [3]. (Note that this is a crucial requisite to simulate charge assisted reactions on the surface, like photocatalytic processes.) In the continuation, we would like to carry out the same work for β-Ga_2O_3 .

Charge transport across phases plays an important role in photocatalysis, where the electron or the hole, generated by photo-excitation, promotes the chosen reaction, while the other carrier gets trapped, e.g., by scavenger molecules. In both processes, it is a crucial question whether the molecule is adsorbed or desorbed after charge transfer. Atomistic modelling via electronic structure calculations on periodic models has become a vitally important part of R&D also in these areas. Modelling of photo-catalytic reactions typically involves only one of the photo-excited carriers, since the other member of the electron-hole pair must be outside the explicitly treated (relatively small) system, to prevent recombination. Supercells with a net charge require corrections because of the interaction between artificially repeated charges. While various schemes have been proposed for correcting the total energy of charged defects in the bulk, gas/solid interfaces, where the charge can be located in either phase, remain a challenge. Solutions suggested so far are either restricted to special cases (making assumptions on the location of the charge) or do not correct the selective effect of the spurious electrostatic potentials on the individual one-electron states (i.e., are not self-consistent). The latter effect is demonstrated in Fig. 1. In this project we develop a general and self- consistent charge correction scheme for supercell calculations in charged 1D, 2D and 3D systems. Our test system is the anatase-TiO_2 (101) surface, where we investigate reactions relevant to the photocatalytic oxidation/reduction of CO_x and NO_x species. In the first year of the project, we have discovered that, upon electron scavenging by O_2 molecules (a crucial reaction in the photo-assisted oxidation of CO), the negatively charged O_2^- desorbs from the surface [4]. In the following we will investigate, how this process contributes to the full photocatalytic (i.e. cyclic) oxidation of CO. We will also investigate hole scavenging by H_2O and its role in the electron-assisted adsorption of NO_2 on the anatase-TiO_2 (101) surface.

In addition to the above investigations, we have also studied the relation between the band edge positions in TiO_2 and the efficiency of photocatalytic water splitting. We have found that the observed trends can be interpreted in terms of H^+ / OH^- adsorption, and shifting this ratio allows to increase the water splitting efficiency [5,6].

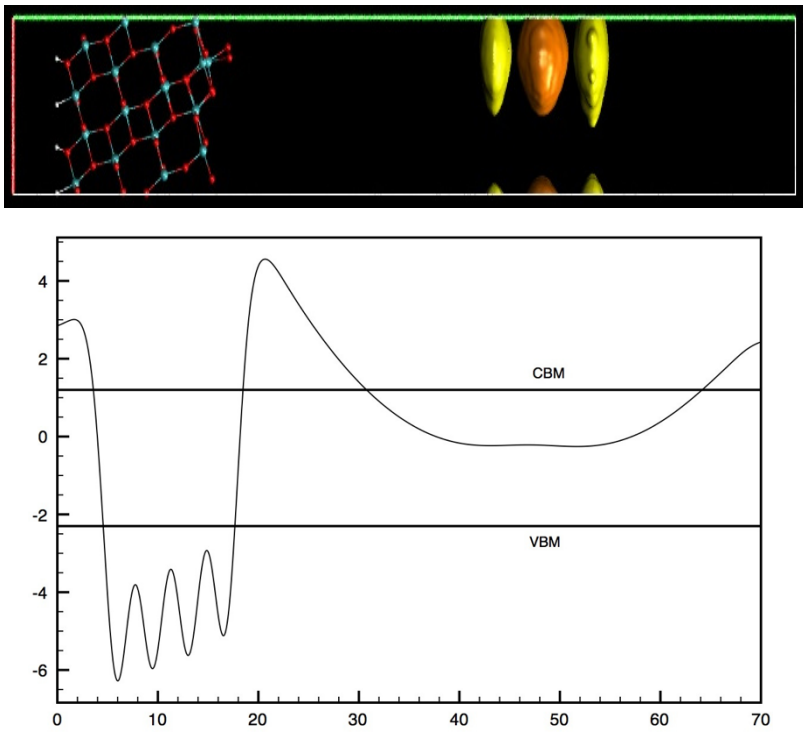

Figure 1: Probability distribution of artificial states (top) arising in a periodic slab model of an O_2^- molecule, adsorbed on the anatase (101) surface, due to the spurious electrostatic potential (bottom) arising in lack of a self-consistent charge correction. (N.B.: the potential ought be constant in the vacuum region. Instead it drops below the conduction band edge of anatase.)

Finally, we have started the investigation of the electronic phase transition observed in the B-phase of VO_2 which is not accompanied by a structural transition. This is a benchmark case for electronic structure theory and has also the potential for application in resistive switches. Our study in the first year has shown that the transition is not connected to thermal expansion, and is entirely an electron correlation effect. Preliminary investigations have shown that a correct description requires the application of a self-consistent cluster- mean-field-theory. Programming that is under way.

WWW

http://hjkwww.bccms.uni-bremen.de/cms/people/p_deak/

More information

[1] P. Deák, B. Aradi, and T. Frauenheim, *Oxygen deficiency in TiO2: Similarities and differences between the Ti self- interstitial and the O vacancy in bulk rutile and anatase*, Phys. Rev. B **92**, 045204 (2015). doi 10.1103/PhysRevB.92.045204

[2] P. Deák, Quoc Duy Ho, F. Seemann, B. Aradi, M. Lorke, and T. Frauenheim, *Choosing the correct hybrid for defect calculations: a case study on intrinsic carrier trapping in* β-Ga_2O_3 , Phys. Rev. B, submitted.

[3] M. F. Tabriz, B. Aradi, T. Frauenheim, and P. Deák, *Application of the Lany-Zunger polaron correction for calculating surface charge trapping*, J. Phys.: Condens. Matter., invited paper (to be published)

[4] M. F. Tabriz, B. Aradi, T. Frauenheim, and P.~Deák, *Electron scavenging by O_2 from the anatase-TiO_2 (101) surface*, J. Chem. Phys., in preparation.

[5] J. Kullgren, B. Aradi, T. Frauenheim, L. Kavan, and P.~Deák, *Resolving the controversy about the band alignment between rutile and anatase: the role of OH^-/H^+ adsorption*, J. Phys. Chem. C **119**, 21952 (2015). doi:10.1021/acs.jpcc.5b04821

[6] P. Deák, J. Kullgren, B. Aradi, T. Frauenheim, and L. Kavan, *Water splitting and the band edge positions of TiO_2* Electrochim. Acta **199**, 27 (2016). doi: 10.1016/ j.electacta.2016.03.122

6.4 *hbc00018:* Electrochemical oxidation of methanol on bimetallic gold-based catalysts: Quantum-chemical modeling

HLRN Project ID:	hbc00018
Runtime:	I/2016 – IV/2016
Project Leader:	Dr. Lyudmila Moskaleva
Project Scientists:	Yong Li, André Wark, Wilke Dononelli
Affiliation:	Institute of Applied and Physical Chemistry, University of Bremen

Overview

Free, ligand-stabilized, andoxide-supported gold nanoparticles have been most active domains of research related to gold catalysis. Different from the well-studied gold-nanoparticle catalysts, the mechanistic understanding of catalytic processes on nanoporous gold, a sponge-like monolithic material, is far less developed.

The present project is a part of the DFG Research Unit FOR 2213 “Nanoporous gold: A prototype for a rational design of catalysts” whose aim is to develop nanoporous gold (npAu) as a prototype for a rational design of catalysts. To this end, we study the interplay between the composition and structural parameters and the catalytic properties of npAu.The selected canonical reaction studied within the Research Unit is oxidation/ electrooxidation of methanol. The current theoretical contribution is devoted to study the detailed reaction mechanisms involved in the oxidation of methanol on model Au catalysts. It will help gaining atomistic insight into complex chemical processes occurring on nanoporous gold and will assist in the interpretation of the experimental results of our project partners.

During the current funding period we focused on the two main aspects described in the following: the first steps of methanol oxidation on nanoporous gold and oxygen-induced surface reconstruction and dynamics of nanoporous gold. We applied quantum-chemical methods based on density-functional theory (DFT), including static DFT computation as well as ab initio molecular dynamics (AIMD) simulations. The curved ligaments of nanoporous gold were represented by stepped Au(310) and Au(321) substrates using periodic slab models.

Results

Mechanistic picture of methanol oxidation on npAu. One of the most crucial questions addressed by the project is the nature of the active oxygen species on npAu under real-catalysis conditions. The O_2 dissociation to atomic O on npAu occurs at ambient conditions but not in ultrahigh vacuum due to a relatively high barrier for this process. Therefore, atomic oxygen on npAu is a probable active species but other possible reactive forms of oxygen to be considered are molecular oxygen (O_2), hydroxo (OH) and hydroperoxo (HOO) species. The latter species can be formed by a reaction of O_2 with water or methanol [1,2]. We have calculated the corresponding transition states and demonstrated that the activation barriers are quite low, 0.3-0.5 eV, much lower than for O_2 dissociation to atomic O, > 1 eV. Figure 1

shows the reaction path for methanol oxidation by O_2 on the model Au(321) surface. A very similar profile was also calculated on the Au(310) surface, and hence, we show that our findings could be generalized to stepped surfaces of different kinds and possibly also to gold nanoparticles. Adsorbed OH groups formed along with the methoxy species can recombine with a low barrier of only 0.1 eV forming surface atomic O and water. The active surface oxygen species can in subsequent steps react with methanol and methoxy, finally producing a weakly adsorbed formaldehyde, Fig. 2.

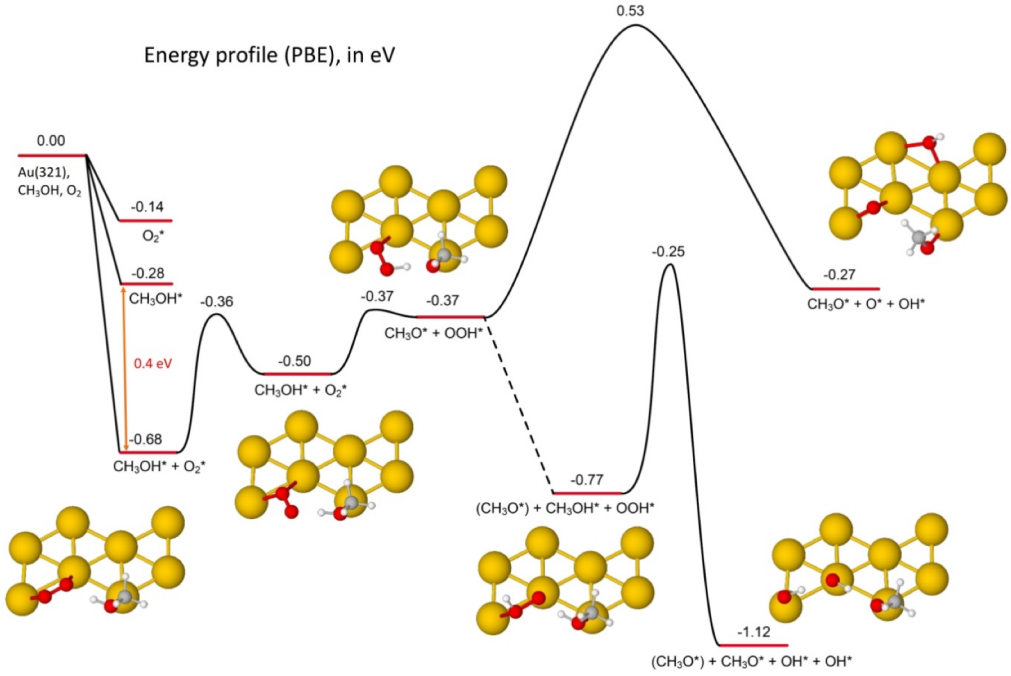

Fig. 1. Calculated reaction path for methanol oxidation to CH_3O and formation of surface O and OH species on the step sites of the Au(321) surface [1].

The influence of admetals– either being residuals from the dealloying process or deposited deliberately (e.g. by underpotential deposition) – for the catalytic performance and, in particular, for the activation of molecular oxygen can be significant. We therefore studied the reaction pathways shown in Figs. 1 and 2 in the presence of Ag impurity atoms. We have shown that silver facilitates adsorption and dissociation of O_2 but increases barriers for the direct reaction of methanol or water with O_2.

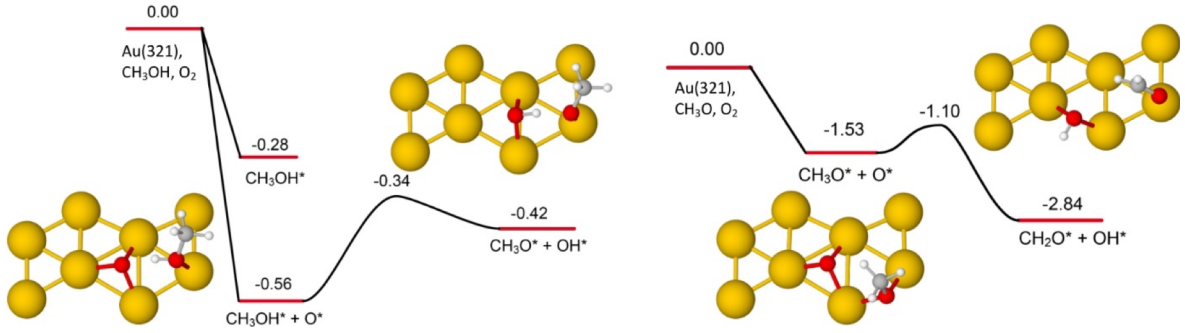

Fig. 2. Calculated reaction path for the reaction of surface atomic O with methanol (left) and methoxy (right) on the step sites of the Au(321) surface [1].

Oxygen-induced surface reconstruction and dynamics .Surface composition of nano-structured gold catalysts plays an important role in determining their catalytic activity and selectivity. Therefore, determining the microstructure and chemical composition of a gold surface under oxidation conditions becomes a fundamental, urgent and important task. However, because of the inertness of bulk gold, surface science studies of gold oxidation are rather scarce. For example, it is still debated whether subsurface O on gold is stable and what type of surface oxide species are formed on gold. In our recent publication [3] we have studied various forms of adsorbed oxygen on pure gold as well as gold-silver alloys. We have shown by using *ab initio* thermodynamycs approach that subsurface oxygen could be stabilized if it is involved in the formation of –(O-Au)- chain structures. Such chain structures of various lengths (examples are shown if Figs. 3,4) were found to be the most stable forms of adsorbed oxygen on gold. Their stability increases on Au surfaces with silver impurities.

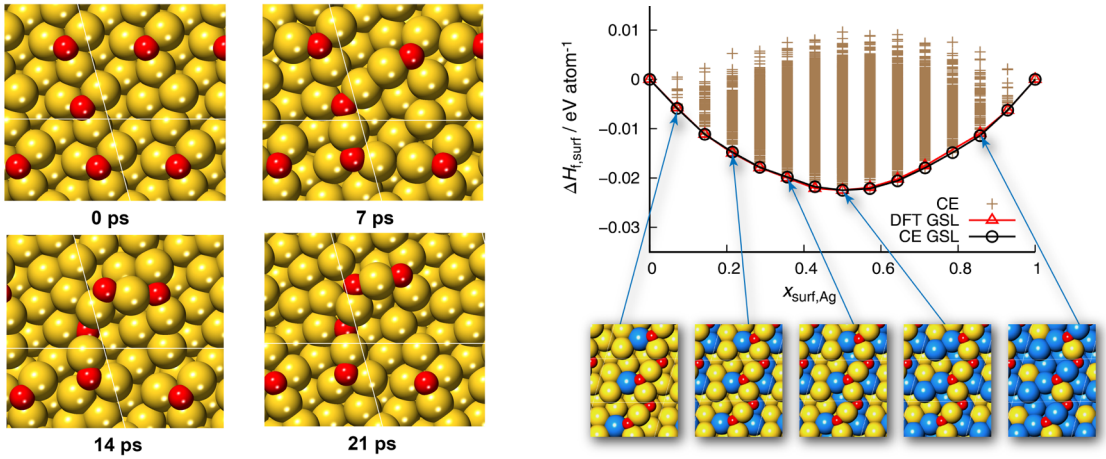

Fig. 3. An AIMD simulation (700 K) showing –(Au-O)- chain formation from individually adsorbed O atoms on Au(321) [4] (left) and surface stability diagram for the bimetallic Au-Ag(321) surface with an infinite oxide chain [5] (right). Au atoms are depicted in yellow, Ag atoms in blue and O atoms in red.

Very recently [4] we studied the formation of oxygen chain structures on pure gold and gold with impurity silver atoms using the stepped Au(321) surface as a model. The results of an AIMD simulation are shown in Fig. 3. Calculations show that individually adsorbed O atoms on the step edges of Au(321) start to build chains consisting of linear O-Au-O units. We have shown [2,4] that the Au-O bond within such units are unusually strong due to s-d hybridization of Au levels caused by relativistic effects.

Oxygen induced silver segregation in AuAg alloys has been anticipated but not systematically addressed until now. Indeed, our calculations predict Ag–O bonds to be stronger than Au–O bonds by ~ 0.12-0.15 eV (estimated from adsorption energy of O on pure Au and mixed Au-Ag three-fold sites). Hence, one would expect that on Au-Ag surfaces with adsorbed O species structural rearrangements should happen, allowing for silver diffusion to the top layer replacing gold atoms at those positions where adsorbed O species are located. However, our recent study of silver segregation using static and dynamic approaches [5] has shown that, although silver indeed prefers positions close to oxygen,

surprisingly, it does not replace gold within the –(Au-O)- chains until very high concentrations of silver, Fig. 3 (left). AIMD simulations supported that finding by demonstrating that silver atoms can easily diffuse along the gold surface toward oxygen as well as the –(Au-O)- chain themselves can also diffuse as a unit [5].

AIMD simulations provide microscopic insight into the dynamical evolution of the surface structure in the process of silver atoms diffusion and show probable surface reconstruction pathways. In addition to the diffusion of Ag atoms on the surface, we were able to show that vertical diffusion of Ag atoms located in deeper layers should also be feasible, Fig. 4. Importantly, no Ag diffusion happened on the time scale of 24 ps in reference systems not containing surface oxygen.

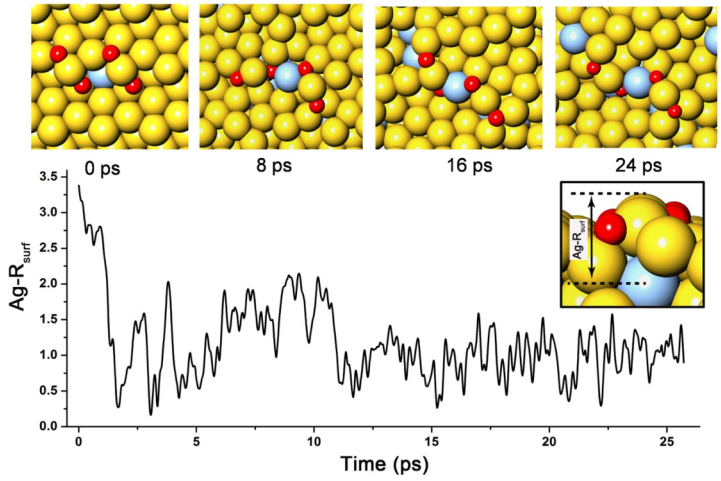

Fig. 4. An AIMD simulation showing vertical Ag diffusion from a subsurface layer to the surface. Ag-R_{surf} represents the distance of Ag atom initially located near the step edge to the reference point on the surface and is plotted along the whole simulation trajectory.

Outlook

We plan to continue our study of methanol oxidation on bimetallic Au-M systems, extending the scope to other admetals (M = Cu, Pt, Ni) and to further oxidation steps up to total oxidation products CO and CO_2. Solvent effects will be taken into account and we will calculate the Gibbs free energies of the important redox steps as a function of the electrostatic potential by using the concept of the computational standard hydrogen electrode.

Publications

1. W. Dononelli, T. Klüner, L. V. Moskaleva, *A mechanistic study of aerobic methanol oxidation on nanoporous gold*, in preparation.
2. L. V. Moskaleva, *Theoretical mechanistic insights into propylene epoxidation on Au-based catalysts: Surface O versus OOH as oxidizing agents*, Catal. Today, *278*,45-55 (2016).
3. L. V. Moskaleva, *Chemisorbed Oxygen on the Au(321) Surface Alloyed with Silver: A First-Principles Investigation*, J. Phys. Chem. C, *119*, 9215-9226(2015).
4. Y. Li, L. V. Moskaleva, *Formation of oxygen chains and silver segregation on Au-Ag alloy surfaces: Insights from ab initio molecular dynamics*, in preparation.
5. S. Hoppe, Y. Li, L. V. Moskaleva, S. Müller, *How silver segregation stabilizes 1D surface gold oxide: A cluster expansion study combined with ab initio MD simulations*, Phys. Chem. Chem. Phys., submitted.

6.5 *hbi00024:* 3D Simulation einer kompressiblen Edelgasströmung innerhalb eines thermischen Lichtbogentriebwerks

HLRN-Projektkennung:	hbi00024
Laufzeit:	II/2014 – II/2017
Projektleiter:	PD Dr.-Ing Rodion Groll
Projektbearbeiter.	J. Gomez
Institut / Einrichtung:	ZARM – Center of Applied Space Technology and Microgravity, Universität Bremen

Überblick

Im vorliegenden Forschungsprojekt wird das Verhalten eines Lichtbogentriebwerks, welches mit den Edelgasen Neon, Argon, Krypton und Xenon betrieben wird, sowohl experimentell als auch numerisch untersucht. Der experimentelle Versuchsaufbau wird in Abb. 1 schematisch dargestellt. In vorherigen Projektphasen wurde der Fokus auf das Verhalten der kompressiblen Strömung im Kaltgas-Betrieb gelegt. Das Kaltgas-Triebwerk wird unter Vakuumbedingungen betrieben. Bei den Kaltgas-Untersuchungen wurde der Druckverlust für die jeweiligen Gase bei verschiedenen Massenstromwerten zwischen 0,178 mg/s und 3,568 mg/s gemessen. Die Knudsen-Zahlen der untersuchten Betriebspunkte liegen oberhalb der Kontinuumsgrenze 0,01, was zum Auftreten von Verdünnungseffekten führt. Die experimentell ermittelten Druckwerte wurden mit numerischen Simulationsergebnissen verglichen. Als numerischer Ansatz wurde sowohl die kompressible Form der Navier-Stokes-Gleichungen mit gewöhnlichen Haftbedingungen, als auch die kinetische Direct-Simulation-Monte-Carlo (DSMC) Methode berücksichtigt.

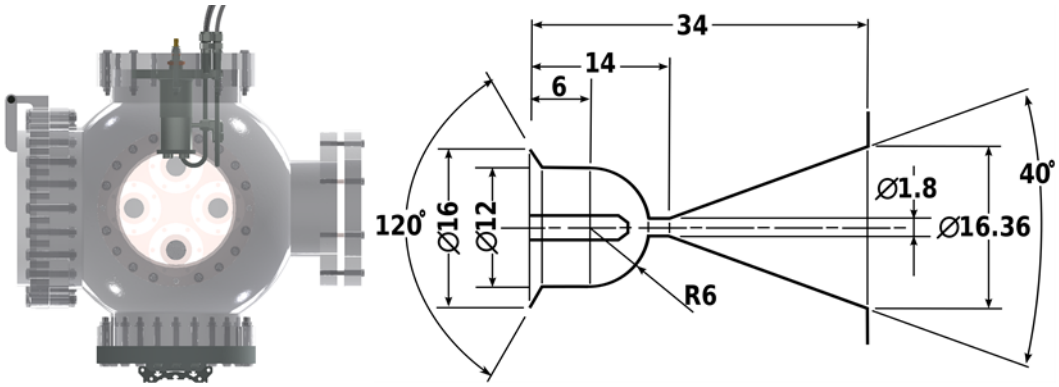

Abb. 1: Schematische Darstellung des Versuchsaufbaus (links) und der eingesetzten Lavaldüse (rechts) mit geometrischen Maßen in mm.

Aus dem Vergleich zwischen den experimentellen Ergebnissen und den Navier-Stokes-Simulationen wurde eine von der Knudsen-Zahl abhängige Korrekturfunktion entwickelt, welche auf vier gasunabhängigen Koeffizienten basiert. Die Knudsenfunktion ermöglicht es, aus Navier-Stokes-Simulationen mit gewöhnlichen Haftbedingungen den korrekten Druckverlust in Abhängigkeit von der Knudsen-Zahl zu bestimmen. Hierbei liegt der Hauptvorteil des Ansatzes an den deutlich niedrigeren Rechenanforderungen im Vergleich zu DSMC-Simulationen.

In der laufenden Projektphase wird der Fokus auf das Verhalten der kompressiblen Strömung im Heißgas-Betrieb gelegt. Hierbei wird das Plasma, welches durch die elektrische Entladung zwischen der Kathode und der Anode des Lichtbogentriebwerks entsteht, mittels eines hauseigenen, kinetischen Ansatzes modelliert. Vorläufige Ergebnisse bestätigen die Anwendbarkeit des entwickelten Modells.

Ergebnisse

In vorherigen Projektphasen konnte eine mathematische Korrekturfunktion entwickelt werden, welche es ermöglicht, die Druckergebnisse der Navier-Stokes-Simulationen mit Haftbedingungen für den Kaltgas-Betrieb des Lichtbogentriebwerks zu korrigieren. Die experimentellen und numerischen Ergebnisse werden in Abb. 2 dargestellt. Aus Abb. 2 ist die sehr gute Übereinstimmung zwischen den korrigierten, numerischen Ergebnissen und den experimentell ermittelten Druckwerten ersichtlich.

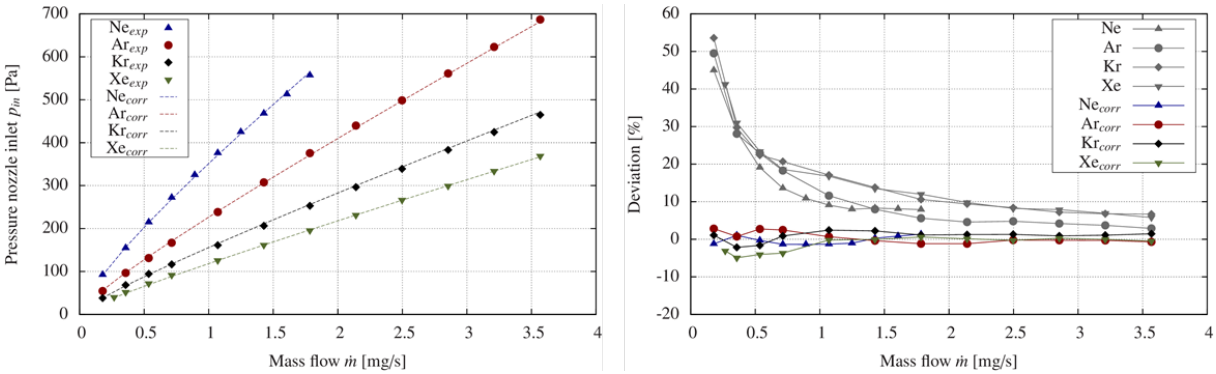

Abb.2: Experimentelle und korrigierte Navier-Stokes-Ergebnisse für den Inletdruck in Abhängigkeit vom Massenstrom. Links: Absolute Druckwerte; rechts: Relative Abweichungen.

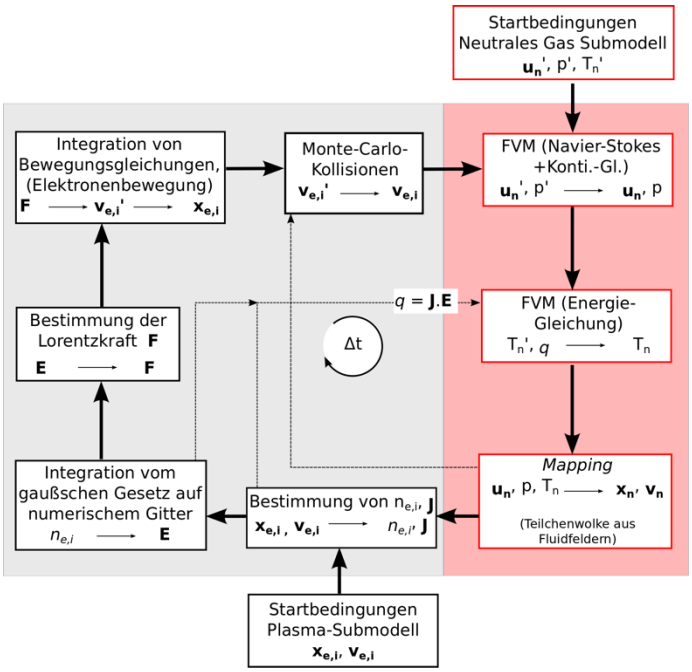

Abb. 3: Konzept eines Plasmamodells. Grau: Kinetisches Submodell für Elektronen und Ionen. Rot: Fluid-Submodell für neutrales Gas. u: Geschwindigkeitsfeld; p: Druck; T: Temperatur; q: Quellterm (Joule'sche Erwärmung); x: Position (Testpartikel/kinetisch); v: Geschwindigkeit (Testpartikel/kinetisch); Indizes: n: neutrales Gas; e: Elektronen; i: Ionen.

In der laufenden Projektphase wird ein neuartiges Konzept zur Modellierung vom Plasma innerhalb des Lichtbogentriebwerks beim Heißgas-Betrieb entwickelt und erprobt. Aufgrund der sehr hohen Rechenanforderungen wird auf einen vollständig kinetischen Ansatz verzichtet und ein hybrides Modell angestrebt. Das Modell besteht aus einer kinetischen Behandlung der Elektronen und Ionen und einer fluiddynamischen Betrachtung des neutralen Gases im Plasma. Durch die kinetische Betrachtungsweise der Elektronen kann die Nutzung empirischer Parameter zur Beschreibung der Elektronenbeweglichkeit und der elektrischen Leitfähigkeit vermieden werden. Da die direkte, kinetische Betrachtungsweise grundsätzlich annahmenfrei ist, bietet dieser Ansatz die Möglichkeit, wichtige und neuartige Erkenntnisse bezüglich der Energieaustausch- und Transportmechanismen für Elektronen innerhalb eines elektrischen Antriebssystems zu gewinnen. Das zu entwickelnde Modell ist in Abb. 3 schematisch dargestellt. Im Rahmen der laufenden Projektphase konnten erste Ergebnisse für das kinetische Submodell für Elektronen und Ionen(s. Abb. 3, grau) gewonnen werden.

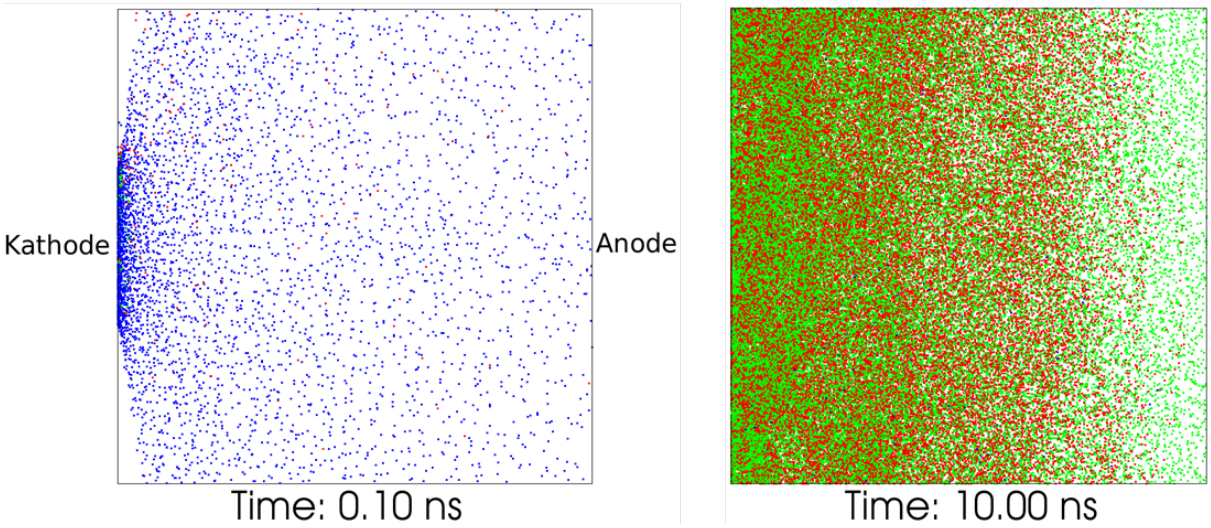

Abb. 4: Vorläufige Ergebnisse für die elektrische Entladung zwischen der Kathode und der Anode eines Lichtbogentriebwerks zu dem Zeitpunkt t = 0,10 ns (links) und t = 10 ns (rechts). Blau: Elektronen aus der Kathode (Primärelektronen); rot: Durch Ionisierung entstehende Elektronen (Sekundärelektronen); grün: Durch Ionisierung entstehende Ionen.

Vorläufige Ergebnisse für die elektrische Entladung innerhalb des Lichtbogentriebwerks werden in Abb. 4 dargestellt. Bei dieser Simulation wird Argon als neutrales Gas modelliert und eine elektrische Stromstärke von 30 Azwischen Kathode und Anode vorgegeben. Zu dem Zeitpunkt t = 0,1ns ist eindeutlicher Überschuss an Primärelektronen (blaue Punkte) zu erkennen. Darüber hinaus befinden sich nur wenige Ionen (grün) und Sekundärelektronen (rot) im Berechnungsraum. Die Elektronen werden auf Grund des entstehenden, elektrischen Feldes in Richtung der Anode beschleunigt. Dabei kollidieren sie mit neutralen Argon-Atomen in der Brennkammer des Lichtbogentriebwerks. In Abhängigkeit von der Kollisionsenergie können diese Kollisionen zur Ionisierung des neutralen Atoms und zur Bildung eines Elektron-Ion-Paares führen. Die entstehenden Sekundärelektronen werden ebenfalls in Richtung der Anode beschleunigt und können selbst weitere Ionisierungskollisionen einleiten. Die resultierende Elektronenlawine hat die Bildung eines elektrischen Lichtbogens zwischen der Kathode und der Anode des Lichtbogentriebwerks zur Folge. Abb. 4 (rechts) zeigt die Simulation zu dem Zeitpunkt t = 10 ns. Man beachte die

sehr große Anzahl an Ionen und Sekundärelektronen im Vergleich zur Anfangsphase t = 0,1 ns.

Anhand der räumlichen Verteilung der Ladungsträger können mittels des entwickelten Solvers die elektrische Feldstärke, die Stromdichte und das elektrostatische Potentialfeld ermittelt werden. Der zeitliche Verlauf des elektrostatischen Potentials an der Kathodenoberfläche wird beispielsweise in Abb. 5 dargestellt. Aus der Abbildung ist ersichtlich, dass die elektrische Entladung ein hoch instationärer Vorgang ist. Ein quasistationärer Zustand kann jedoch nach ca. 5 ns beobachtet werden. Die gewonnen Werte für das elektrische Potential und die Stromdichte können zur Bestimmung der Joule'schen Erwärmung und zur Modellierung des gesamten Triebwerks genutzt werden.

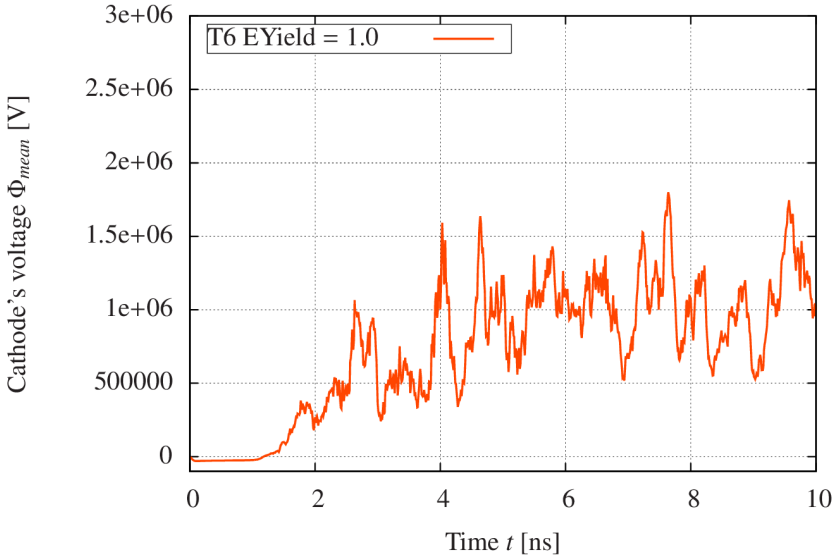

Abb. 5: Zeitlicher Verlauf des elektrischen Potentials [V] an der Kathodenoberfläche.

Ausblick

Mit Hinblick auf die Simulation des Lichtbogens ist die Untersuchung der Entstehungsmechanismen von Elektronen an den Triebwerkswänden von zentraler Bedeutung. Auf diese Weise könnte eine gute Übereinstimmung zwischen den numerischen und den experimentellen Ergebnissen für den Spannungsabfall zwischen Kathode und Anode erreicht werden.

Publikationen

1. J. Gomez, R. Groll, Pressure drop and thrust predictions for transonic micro nozzle flows, Physics of Fluids (1994-present), 28, 022008 (2016)

2. J. Gomez, R. Groll, Experimental and numerical study of the pressure drop in transonic micronozzle flows across multiple flow regimes, ASME 2016 14th International Conference on Nanochannels, Microchannels, and Minichannels, Washington DC, July 10-14 2016, American Society of Mechanical Engineers

6.6 *hbi00026:* DSMC-Simulation einer verdünnten Edelgasströmung innerhalb eines Kaltgas-Arcjets

HLRN-Projektkennung:	hbi00026
Laufzeit:	II/2016 – I/2017
Projektleiter:	Dr.-Ing. habil. Rodion Groll
Projektbearbeiter.	Till Frieler, M.Sc.
Institut / Einrichtung:	ZARM – Zentrum für angewandte Raumfahrttechnologie und Mikrogravitation

Überblick und Projektbeschreibung MOLETHRUSTBALANCE

Elektrische Raumfahrtantriebe sind heutzutage bereits in einer Vielzahl von Weltraummissionen erfolgreich im Einsatz und werden beispielsweise zur Bahn- und Lageregelung auf geostationären Kommunikationssatelliten oder für interplanetare Langzeitmission genutzt. Für die Entwicklung neuer Triebwerke sind unter anderem Leistungsmerkmale, wie Antriebsleistung (spezifischer Impuls), Treibstoffverbrauch (Treibstoffeffizienz) und Regelverhalten (Schubcharakteristik) von großer Bedeutung.

Um eine Aussage über die Treibstoffeffizienz und die Schubcharakteristik eines Triebwerks machen zu können, ist es sinnvoll die Schubkraft F_s bestimmen zu können. Im Rahmen des Forschungsprojektes MOLETHRUSTBALANCE wird einerseits ein Versuchsstand zur experimentellen Messung und Untersuchung der Schubkraft von elektrischen Triebwerken niedriger Leistungsklasse entwickelt und aufgebaut, sowie andererseits numerische Kaltgas-Simulationen mittels DSMC-Methoden durchgeführt. Die Ergebnisse aus den Simulationen und den durchgeführten Versuchen sollen anschließend verglichen werden, um so Erkenntnisse für die weitere Optimierung des Triebwerks sammeln zu können.

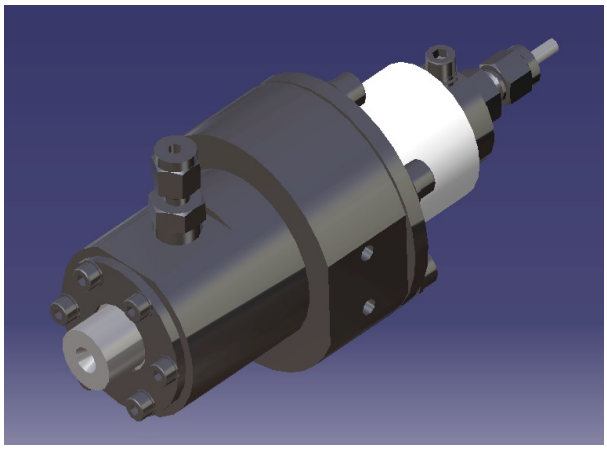

Abb. 1: Gerenderte, isometrische Ansicht des INGA IV Lichtbogentriebwerks.

Das in dem Projekt MOLETHRUSTBALANCE untersuchte Triebwerk ist das am ZARM neu entworfene Lichtbogentriebwerk INGA IV. Das Triebwerkist in Abbildung 1 dargestellt. Mit dem vorgestellten Triebwerk INGA IV können Differenzdrücke zwischen dem Inneren des Triebwerks und der Vakuumkammer aufgezeichnet und untersucht werden. Aus den gemessenen Drücken und dem Massenstrom des eingeleiteten Gases können, unter Verwendung der numerischen Methoden, Rückschlüsse auf die Antriebsleistung gezogen werden.

Technische und mathematische Aspekte

Für die, in dem Projekt MOLETHRUSTBALANCE durchgeführten, numerischen Berechnungen wurden an der Standardimplementierung des DSMC-Solvers in dem Softwarepaket OpenFOAM einige Änderungen vorgenommen. Die Änderungen beinhalteten die Implementierung eines neuen Inflowmodells ZARMInOutflow, welches auf dem InOutflow-Modell der Standardimplementierung aufbaut. Es ermöglicht dem Nutzer die, aus den Experimenten genau definierten, Massen- oder Volumenströme über die Volumenränder des

Inlets vorzugeben. Für die Randflächen des Outletvolumens ist der Druck die vorgegebene makroskopische Größe aus den Experiemten. Dieser wird als Absolutdruck durch die Drucksensoren der Vakuumanlage gemessen und stellt den, sich im stationären Betriebszustand eingestellten, Umgebungsdruck in einiger Entfernung zum Diffusorende (Düsenauslass) dar.

Anders als bei Finite-Volumen-Solvern hängt bei statistischen Methoden, wie der DSMC-Methode, der Rechenaufwand stark von der Gesamtanzahl der simulierten Testpartikel im Simulationsvolumen ab. Der Rechenaufwand für die einzelnen Testpartikel lässt sich hierbei nochmals in die Anteile Molekülbewegung und Kollisionsberechnung unterteilen. Abhängig von der Art der Implementierung der Kollisionsroutine in den numerischen Solver nimmt nach Titov [1] die Berechnung der Kollisionen bis zu 60% der Rechenzeit in Anspruch. Um den numerischen Aufwand der Kollisionsberechnung bei hohen Drücken zu reduzieren, wurde eine Methode zur Begrenzung der Kollisionen nach Titiov [1] implementiert.

Validierung des modifizierten Solvers

Für die Vailidierung der implementierten Änderungen am Code und des neuen Inflowmodells wurde ein bekannter Testcase aus der Literatur herangezogen, welcher bereits durch andere Autoren zur Validierung numerischer Ergebnisse genutzt wurde. Für den B = 590 Testcase von Rothe [2] liegen somit sowohl experimentelle, als auch numerische Ergebnisse anderer Autoren [3] für eine Laval–Düsenströmung vor, an denen die aktuellen numerischen Ergebnisse validiert werden können. Zusätzlich wurde der Testcase noch mit einer nicht modifizierten Variante des OpenFOAM DSMC-Codes berechnet und ebenfalls mit den Ergebnissen der modifizierten Version verglichen.

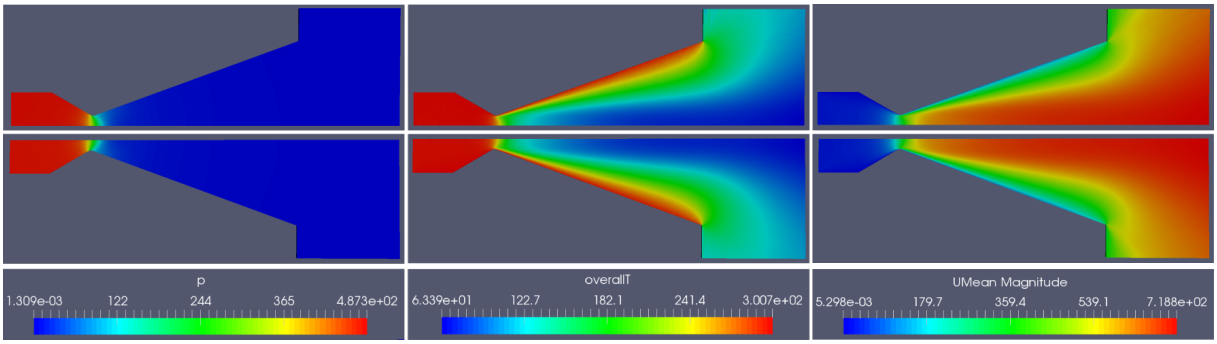

Abb. 2: Von links nach rechts: a) Druckfelder der Rechnung, Ergebnisse des nicht modifizierten DSMC solvers über dem modifizierten Solver, b) Temperaturfelder der Rechnung, Ergebnisse des nicht modifizierten DSMC solvers über dem modifizierten Solver, c) Geschwindigkeitsfelder der Rechnung, Ergebnisse des nicht modifizierten DSMC solvers über dem modifizierten Solver.

In Abbildung 2 sind Druck-, Temperatur- und Geschwindigkeitsfelder des B = 590 Testcases für die modifizierte Variante (untere Bildhälften) sowie für die orginäre Implementierung (obere Bildhälften) des DSMC-Codes in OpenFOAM abgebildet. Gut zu erkennen ist die gute Übereinstimmung der Ergebnisse für beide Solvervarianten. Für eine weitere Validierung wurden die vorliegenden Ergebnisse mit numerischen Ergebnissen anderer Autoren [3], sowie mit den experimentellen Ergebnissen von Rothe [2] vergleichen. In Abbildung 3 sind beispielhaft die Profile der Dichte- und Temperaturverläufe auf der Rotationsachse der Düsengeometrie der Vergleichsfälle und der eigenen Ergebnisse abgebildet. Hierbei wurden sowohl die Temperaturprofile, wie auch die Dichteprofile durch die Ruhegrößen T_0 und ρ_0 aus dem Experiment skaliert. Die axiale Koordinate wurde durch den Düsenhalsradius r* (engster Querschnitt) skaliert um eine Dimensionslose Darstellung zu erhalten. Hierbei stellt

der axilale Wert von x/r* = 0 die Koordiante des Düsenhalses dar und das Ende der Düse (Diffusorende) ist bei x/r* = 18,7 lokalisiert. Gut zu erkennen ist, dass die vorliegenden numerischen Ergebnisse (ZarmdsmcFoam) sowohl gut mit den anderen numerischen Ergebnissen, wie auch mit den experimentellen Ergebnissen übereinstimmen. Im Fall der Temperaturen auf der Rotationsachse (Abbildung 3 rechts) reproduzierten die aktuellen Ergebnisse die experimentellen Ergebnisse von Rothe im Vergleich mit den anderen numerischen Ergebnissen am besten. Bei dem skalierten Verlauf der Dichte kommt es zu einer leichten Unterschätzung der experimentellen Daten für die Dichte, wobei die Ergebnisse, der mit dem SMILE-Solver durchgeführten Rechnungen, exakt reproduziert werden.

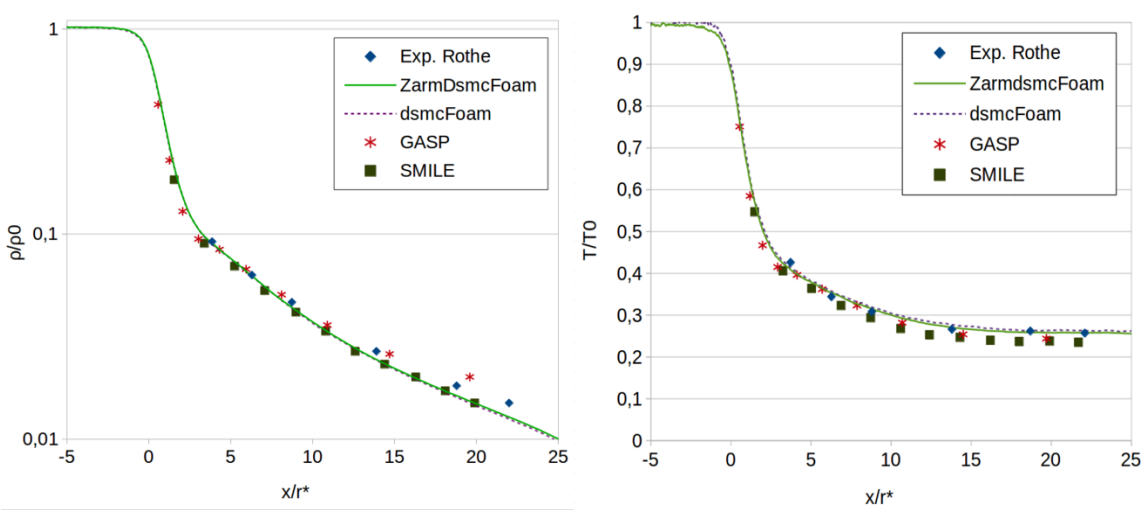

Abb. 3: Dichte- (links) und Temperaturprofile (rechts) auf der Rotationsachse der simulierten Düse. Experimentelle Werte aus [2], numersische Werte für GASP und SIMLE wurden [3] entnommen.

Schub und spezifischer Impuls

Das Schubverhalten und Spezifische Impulse des Triebwerks für verschiedene Argon Massenströme wurden auf numerischer Basis mit dem modifizierten DSMC-Solver ZarmdsmcFoam sowie dem Finite-Volumen Solver rhoCentralFoam aus dem freien Softwarepaket OpenFOAM untersucht. Die Parameterstudie umfasst 30 Massenströme von 0,178 mg/s bis 71,360 mg/s.

In Abbildung 4 sind die berechneten Schubkräfte F_t und Spezifischen Impulse I_{SP} für die beiden numerischen Methoden über den untersuchten Massenstrombereich dargestellt. Für die Schubkräfte wurde eine doppelt logarithmische Darstellung gewählt. Die niedrigsten Schubwerte werden für den kleinsten Massenstrom erreicht. Bei Erhöhung des Massenstroms in das Triebwerk kommt es zu einem Anstieg der Schubkraft, welche für den Größen Massenstrom einen Wert von etwa. 37 mN erreicht. Größere Abweichungen in den Ergebnissen der beiden numerischen Methoden für die Schubwerte sind im niedrigen Massenstrombereich bis 2,854 mg/s zu sehen. Hier werden durch den Navier-Stokes Solver merklich kleinere Schubkräfte vorhergesagt als durch die DSMC Methode, wobei für den kleinsten, dargestellten Massenstrom eine relative Abweichung von 40 % bestimmt wurde. Für Massenströme größer als 2,854 mg/s sinken die Abweichungen zwischen den berechneten Schubkräften unter 3%, wobei für die Größten untersuchten Massenströme nur noch Abweichungen im Promillebereich bestimmt werden konnten. Die numerischen Ergebnisse für den Spezifischen Impuls sind in der rechten Hälfte von Abbildung 4 dargestellt. Gut zu erkennen ist der rapide Anstieg des Spezifischen Impulses I_{SP} im unteren Massenstrombereich. Während für einen Massenstrom von 0,357 mg/s Spezifische Impulse

von 18,1 s (DSMC), bzw. 10,6 s (Navier-Stokes) ermittelt wurden, wurden für einen Massenstrom von 3,568 mg/s bereits Spezifische Impulse von 41,4 s (DSMC) bzw. 41,1 s (Navier-Stokes) berechnet. Für größere Massenströme schwächt sich der Anstieg des Spezifischen Impulses stark ab. So wurden für den 10 mal größeren Massenstrom von 35,680 mg/s nur Spezifische Impulse von 52,2 s (DSMC und Navier-Stokes) ermittelt und für den größten Massenstrom von 71,360 mg/s konnte nur noch ein Anstieg des Spezifischen Impulses von ca. 2 % bestimmt werden.

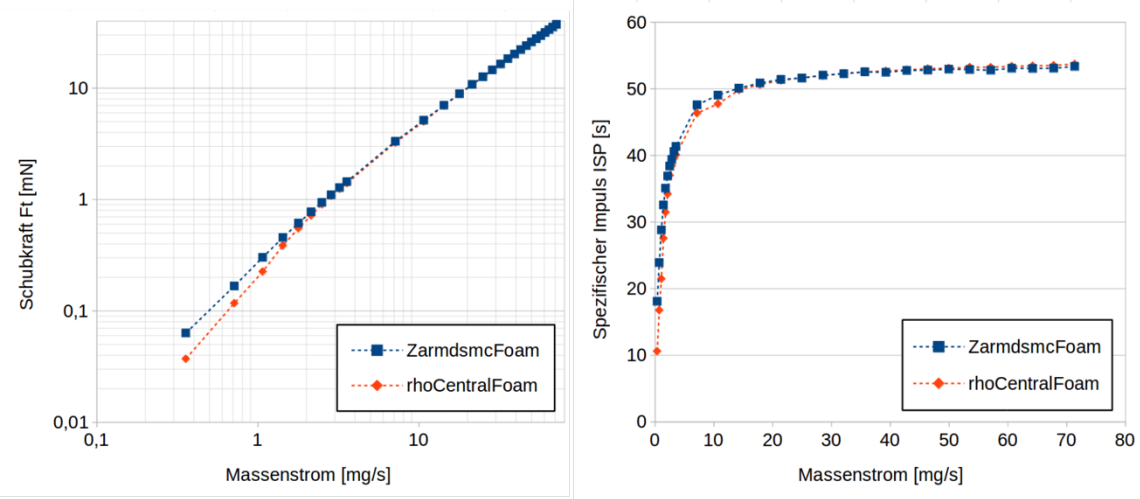

Abb. 4: Berechnete Werte für die Schubkraft F_t und den Spezifischen Impuls I_{SP} über dem Massenstrom.

Ausblick

In dem Forschungsprojekt MoleThrustBalance sollen aus numerischen Bestimmung des Schubs, sowie experimentellen Schubmessungen Erkenntnisse für die Optimierung des INGA IV Triebwerks gesammelt werden. Hierfür sollen sowohl im experimentellen Aufbau, sowie bei den numerischen Berechnungen eine Reihe von Parametern innerhalb einer Parameterstudie variiert und deren Einfluss ausgewertet werden. Im letzten Antragszeitraum wurde das Schubverhalten sowie Spezifische Impulse anhand einer Argon-Gas Messreihe untersucht. Auch wurde das Inflowmodell anhand eines bekannten Testcases validiert. In der zukünftigen Parameterstudie sollen nun die Schubberechnungen auch für die anderen, im experimentellen Aufbau INGA IV zur Verfügung stehenden, Edelgase erweitert werden.

Publikationen

T. Frieler, R. Groll: Using DSMC selection limiter for micronozzle thrust predictions with high density ratios. (inVorbereitung)

WeitereInformationen / Literatur

[1] Titov, Evgeny V., and Deborah A. Levin. "Extension of the DSMC method to high pressure flows." International Journal of Computational Fluid Dynamics 21.9-10 (2007): 351-368.

[2] Dietmar E Rothe. Electron-beam studies of viscous flow in supersonic nozzles. AIAA Journal, 9(5):804–811, 1971.

[3] M. Ivanov, G. Markelov, A. Ketsdever, and D. Wadsworth, “Numerical study of cold gas micronozzle flows”, AIAA paper, 11 (1999).

6.7 *hbi00027:* 3D Simulation of a magnetoplasmadynamic thruster with coaxial induced magnetic field

HLRN Project ID:	hbi00027
Run time:	IV/2015 – II/2017
Project Leader:	PD Dr.-Ing. habil. Rodion Groll
Project Scientists:	Charles Chelem Mayigué, M. Sc.
Affiliation:	ZARM – Center of Applied Space Technology and Microgravity

Overview

The magnetoplasmadynamic (MPD) arcjet is a promising thruster which is developed for exploration missions to the moon and Mars, and for raising orbits of large space structures. The MPD arcjet utilizes mainly electromagnetic force, i.e, Lorentz force, which is generated in this work by interaction between the current density and a coaxial magnetic field azimuthally induced by the total discharge current. In the present work, we developed and used a density-based method associated with a divergence cleaning technique for the simulation of the MPD thrusters under a finite volume formulation. This new algorithm was developed for the single resistive MHD equations and make use of the central-upwind scheme of Kurganov and Tadmor for flux calculation. Electrical conductivity for fully ionized plasma and viscosity are predicted according to the Spitzer-Härm formulation and the Sutherland thermophysical model respectively. The perfect gas equation of state is also considered.

Introduction and motivation

Despite the advances in combustion research, the highest exhaust velocity of a functional chemical propulsion system, 3.600 to 4.500 m/s from sea level to high altitude, is still inadequate for most deep-space missions of interest. The present situation of space exploration calls for missions beyond the moon and for such missions, chemical propulsion is not a viable option, except for the case of launch vehicles where high thrust is required. Functionally, the inability of chemical propulsion systems to achieve higher exhaust velocities is due to limitation in the maximum tolerable temperature in the combustion chamber and to avoid excessive heat transfer to the walls. Both these limitations can be overcome by use of electric propulsion, which can be defined as the acceleration of gases for propulsion by electrical heating and/or by electric and magnetic volume forces. The magnetoplasmadynamic (MPD) thrusters have the unique capability, among all other developed electric propulsion systems, of processing megawatt power levels in a simple, small and robust device, producing thrust densities as high as 100 thousand N/m². These features render it an attractive option for high energy deep space missions requiring higher thrust levels than other electric thrusters. In its basic form, the MPD thruster consists of a cylindrical cathode surrounded by a concentric anode (Figure 1). An electric arc between the electrodes ionizes a gaseous propellant, and the interaction of the current with the self-induced magnetic field accelerates the plasma to produce thrust. The specific impulse of a self-field MPD thruster is related to the parameter I^2/m which is often used to characterize

MPD thruster performance with *I* the discharge current and ***m*** the mass flow rate. High value of ***I²/m*** correspond to predominantly electromagnetic acceleration, and provide higher values of specific impulse. Low values of ***I²/m*** correspond to predominantly electrothermal acceleration, and lower values of specific impulse. MPD efficiency typically increases with increasing ***I²/m***, but this also leads to strong numerical instabilities (The onset phenomena), which makes the solvers unstable and undermines its value. For modeling of the thruster, CFD code is required to understand the complex nature of the coupled electromagnetic and gas dynamic acceleration processes and the effects of relevant flow-field parameters which are otherwise quite hard to analyse with experiments. With the emergence of high-speed computational facilities, CFD code permits model validation using the existing experimental data base. Thus, the ultimate goals of the present project are: Use the developed density-based code to simulate the MPD thrusters in the purpose to obtain insight into the physics of thrust performance and energy dissipation in these devices and also obtain operating conditions and geometrical configurations of a specific type of thruster for which the solver is stable.

Results

A limited set of computer runs were performed to access the effect of geometric scale changes on self-field MPD thruster performance. The first geometry set (MPDT01) consisted of a 0.0095 m radius cathode with 0.264 m length, surrounded by a 0.025 m radius anode. The second set (MPDT02) doubled the anode radius to 0.051 m, but kept the cathode radius at 0.0095 m. The third set (MPDT03) kept the anode radius at 0.051 m, but increased the cathode radius to 0.0181 m. The last set (MPDT04) has the same parameter than MPDT02, but reduce the cathode length to 13.2 cm. For each combination of radii, the anode lengths are scaled from 1 to 5 times the anodes radius (aspect ratio). The argon propellant mass flow rate was kept constant at 6 g/s, and was assumed to be fully ionized for all cases. The five ***I²/m*** values, ranging from 05×10^9 A²s/kg to 62×10^9A²s/kg are evaluated for each geometry. Results of the numerical simulations for MPDT01 are presented below. MPDT01 thruster was not able to converge for aspect ratio la/ra=1. Convergence was obtained for all the ***I²/m*** values with $l_a/r_a > 1$. Thrust and plasma voltage increase with increasing ***I²/m*** (Fig.1). The transition from electrothermal acceleration mode to electromagnetic acceleration mode occur at ***I²/m*** around 18 which correspond to a discharge current value of 10 kA (critical current). The effect of this transition on the MPDT01 thruster performance is well illustrated on Efficiency profil (Fig. 1) which decreases by the electrothermal acceleration mode and starts to increase from the critical current when the electromagnetic thrust becomes dominant. Fig. 2 presents the main flow variables distribution inside and outside the thruster for two different values of ***I²/m*** 18.7 and 62. These results are almost similar for the two other geometry configurations MPDT02 and MPDT03 with different stability range and different critical current value. But most generally, the simulation point out the fact that, at lower ***I²/m,*** thruster operation require larger aspect ratio with shorter cathode length for more stability. For equivalent ***I²/m*** value, small aspect ratio thrusters are required to improve the thruster flow efficiency.

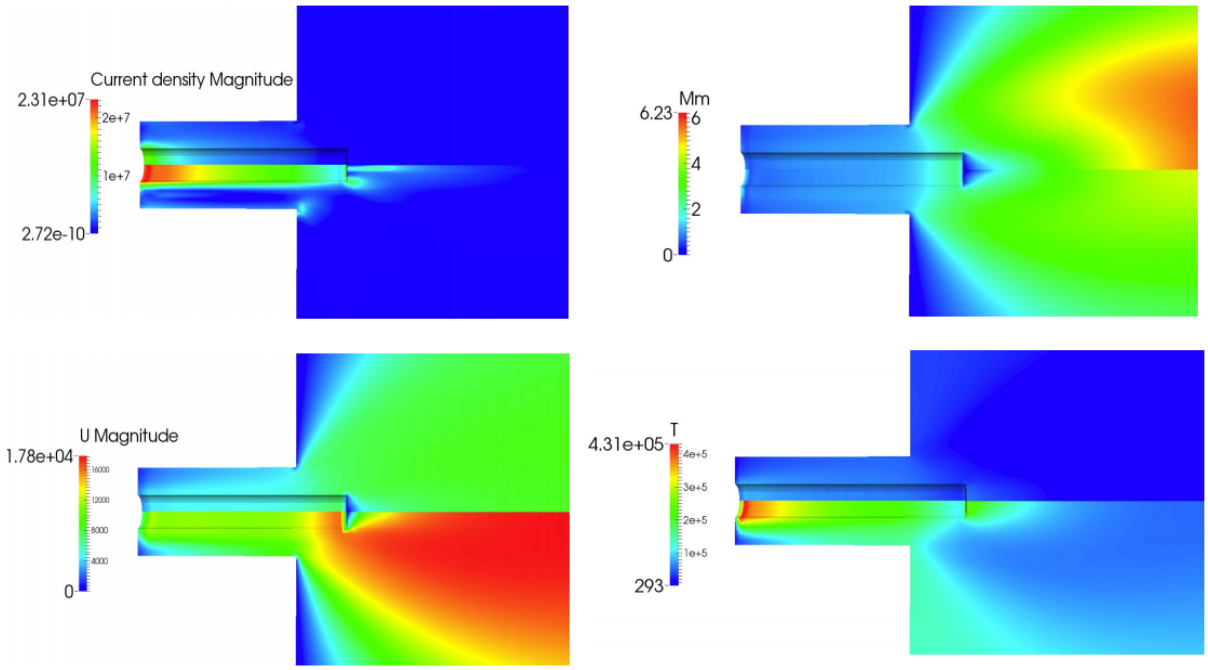

Fig.1: Distribution of current density (Ji) [A/m²], magnetic Mach number (Mm), velocity (U) [m/s] and temperature (T) [K] and for MPDT01 with shorter cathode, 6 g/s mass flow rate and 04 aspect ratio. For each picture, $I^2/m=18.7$ (top) and $I^2/m=62$ (bottom)

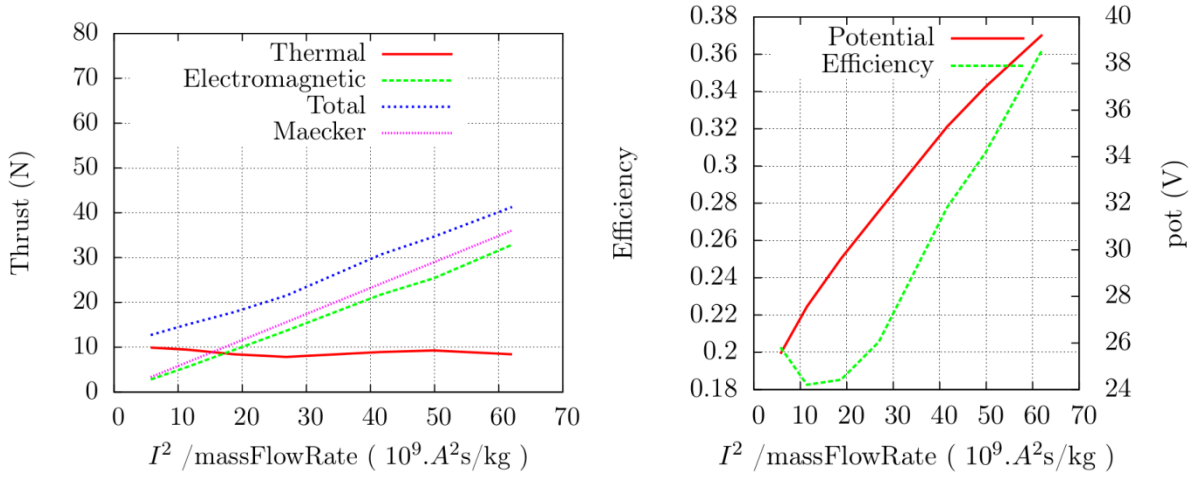

Fig.2: Thrust [N] (left), Efficiency and plasma voltage (right) for MPDT01 with shorter cathode.

Outlook

The results obtained in this project indicate that the semi-discrete density-based central-upwind solver is able to deal with plasma flow simulation in MPD thrusters and therefore will be helpful for their development and designing. However, the code remain unstable by high I^2/m values. Thus, the improvement of the physical model will be an important topic for near future work.

Publications

1. C. Chelem Mayigue, R. Groll, "*A density-based method with semi-discrete central-upwind schemes for ideal magnetohydrodynamics", Arch. Appl. Mech. (2016) doi :10.1007/s00419-016-1216-7.*

2. C. Chelem Mayigue, R. Groll: "*Magneto-Plasmadynamic Thruster modelling with coaxial induced magnetic field*", Int. J. Comp. Meth. and Exp. Meas., Vol. 4, No.*4 (2016) 380–392.*

Presentations

1. C. Chelem Mayigue, R. Groll: 11th International Conference on Advances in Fluid Mechanics in Ancona (Italy), 5-7/09/2016.
2. C. Chelem Mayigue, R. Groll: 4th Northern germany OpenFoam User meetiNg (NOFUN) 2016, Braunschweig, Germany, 29/09/2016.

Acknowledgement

This work is funded by the *Deutscher Akademischer Austauschdienst* (DAAD) through the "Research grants for doctoral candidates and young academics and scientists" programme (grant number 57076385).

References

1. R. G. Jahn, E. Y. Choueiri, *Electric propulsion*, Academic Press Encyclopedia of Physical Science & Technology (2000) 1–17.

2. K. Sankaran, *Simulation of mpd flows using a flux-limited numerical method for the mhd equations*, Ph.D. thesis, Princeton University, Technology and Medicine, Princeton (2005).

5. A. Kurganov, S. Noelle, G. Petrova, Semi-discrete central-upwind schemes for hyperbolic conservation laws and hamilton-jacobi equations, SIAM Journal on Scientific Computations 23 (2001) 707–740.

6. C. J. Greenshields, H. G. Weller, L. Gasparini, J. M. Reese, Implementation of semi-discrete, non-staggered central schemes in a collocated, polyhedral, finite volume framework, for high-speed viscous flows, International journal for numerical methods in fluids 63 (2010) 1–21.

6.8 *hbi00030*: Investigation of performance of an argon fueled magneto-plasmadynamic thruster with applied magnetic fields

HLRN Project ID: hbi00030
Run time: II/2016 – I/2018
Project Leader: PD Dr.-Ing. habil. Rodion Groll
Project Scientists: Charles Chelem Mayigué, M. Sc.
Affiliation: ZARM – Center of Applied Space Technology and Microgravity

Overview

The applied-field magnetoplasmadynamic thrusters (AF-MPDT) are the promising technology for space missions requiring high specific impulse, high thrust density with low on board electric power. In this device, the plasma is accelerated by combining the gas dynamic and the electromagnetic processes. In the present project, the numerical modeling of AF-MPDT is performed using a electromagnetic code to produce external magnetic field and the density-based code, developed in the on going MagJet project, to deal with magnetohydrodynamic (MHD) equations. The magnetic field is axially applied by an external coil surrounding the anode which interacts with the discharge current and the induced azimuthal current to produced thrust. We make used of the Spitzer-Härm formulation for the calculation of electrical conductivity as the plasma in this work is considered fully ionized.

Introduction and motivation

In the electric propulsion systems group, we have the magnetoplasmadynamic thrusters (MPDT), which is classified into two categories; Self-field MPDT (SFMPDT) and applied-field MPDT (AFMPDT). In SFMPDT, the main acceleration mechanism is represented by the interaction between the discharge current and the self-induced magnetic field. That means, high trust level can be obtained only for high discharge current (5-100 kA) and consequently for high power (MWs). Contrary to SFMPDT, the AFMPDT, introduce new acceleration mechanisms that do not directly depend on the discharge current and thus can allow the thruster to effectively operate at lower powers. At all, four acceleration mechanisms have been identified. The relative importance of each depends upon thruster design and operating conditions (current, mass flow rate, applied field strength). The four mechanisms are: Gas dynamic acceleration mechanism: this mode contains the joule heating and the expansion of the plasma through physical and/or magnetic nozzle. Self-field acceleration mechanism: Interaction of discharge current arc and self-induced azimuthal magnetic field lead to axial and radial acceleration. Swirl acceleration mechanism: Interaction of discharge current and applied magnetic fields results in azimuthal force that puts plasma into rotation. The rotation energy can be partly converted to axial acceleration downstream. Hall acceleration mechanism: Interaction of induced azimuthal current (Hall current) and applied magnetic field produces axial and radial lorentz forces.

Other advantages in adopting an AFMPDT is the extension of a significant fraction of the current downstream of the thruster geometry particularly on the pic of the cathode. For the

thruster modeling, CFD code is required to understand the complex nature of the coupled electromagnetic and gasdynamic acceleration processes and the effects of relevant flow-field parameters which are otherwise quite hard to analyse with experiments. With the emergence of high-speed computational facilities, CFD code permits model validation using the existing experimental data base. The main goals of the Applied-MhdJet project are: Optimize the thruster and electrode geometry and particularly the configuration of the applied magnetic field of an AFMPDT. Investigate the influence of externally-applied magnetic fields strength and discharge current on the thruster efficiency. Better understanding of all propellant acceleration mechanisms. The achievement of acceptable thruster performance, especially in terms of thrust efficiency.

Results

A limited set of computer runs were performed to access the effect of external magnetic strength and mass flow rate of Argon on the NASALeRC MPD thruster performance (see Tab.1). For the purpose of comparison of our results with previous study, we decided to change the former geometry with the applied field NASA Lewis Research Center's (NASALeRC) MPD thruster geometry, which in contrary to the Villani-H thruster was typically investigated for applied-field code with a wide range of experimental data. For the same reason, we also decide to replace the geometric scaling analysis based on the ratio of anode over cathode radius by the variation of the mass flow rate of argon which ranging from 0.06 g/s to 0.2 g/s. Thus, the configuration considered (AFMPDT01) consisted of a cathode with 1.27 cm radius, surrounded by an anode with 5.1 cm radius both are 7.6 cm long. For the AFMPDT01 configuration, the magnet coil that provide the applied magnetic field is 15.3 cm long with a 10.15 cm radius. To avoid the creation in the discharge chamber of two magnetic force pointing in opposite direction, the magnet is placed with one end coinciding with the exit plane of the thruster. The second configuration we considered in this work named AFMPDT02, maintains the same geometric dimensions of AFMPDT01 but here, two magnet coils with a 10.15 cm radius have been used instead of one. the first magnet is 11.72 cm long and it is placed one end at 1.6 cm downstream of the inlet. The second one is 3.4 cm long with one end at the thruster exit. For each value of mass flow rate, the discharge current strength are scaled form 750 A to 2000 A. The five values of the applied magnetic field strength was varied from 0.012 T to 0.08 T, as measured at the cathode tip. The most challenging results of the numerical simulations with AFMPDT01 realised at this stage of the project are presented bellow.

The main effect of the application of an axial magnetic field is to put the plasma in rotation inside the discharge chamber of the MPD thruster. Here, for a constant value of applied magnetic field strength, the swirl to self thrust ratio decreases by increasing the current (see Fig. 2). In the other hand for each current value, this ratio increases by increasing the applied magnetic field. Thus, for the case of consideration, it appeared that the swirl component of thrust is dominant and is mostly responsible of the acceleration of the plasma out of the thruster.

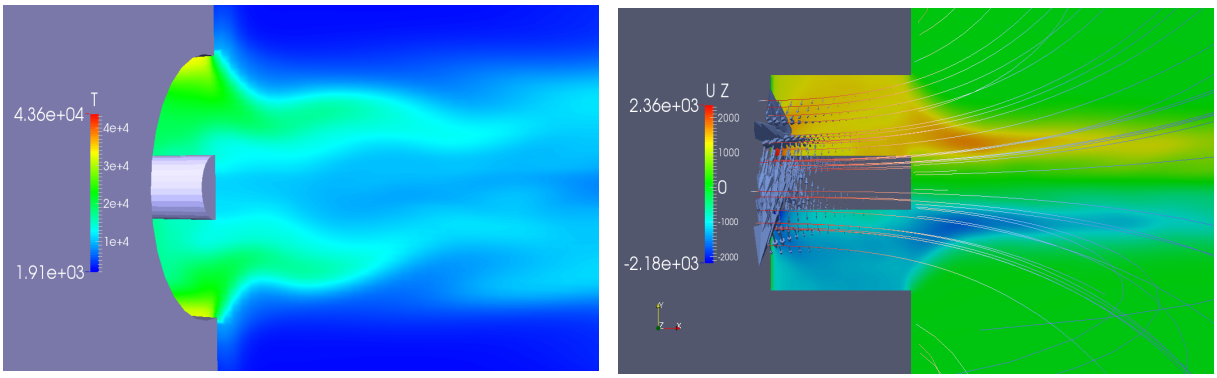

Fig. 1: Temperature distribution (T) [K] outside the discharge chamber (left) and Rotational speed (Uz) [m/s] including applied magnetic field line and induced magnetic field vector (right).

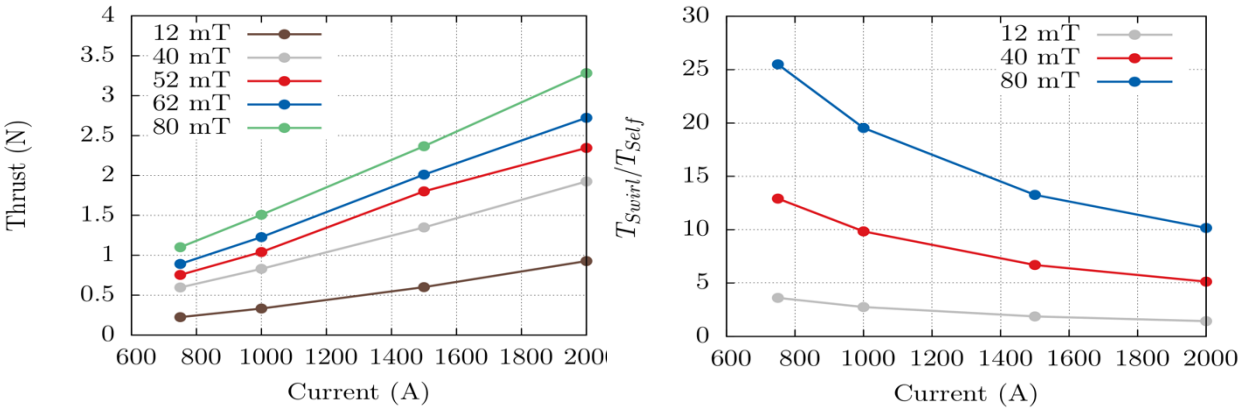

Fig. 2: Thrust [N] (left) and the ratio of swirl over self component of thrust (right) function of discharge current.

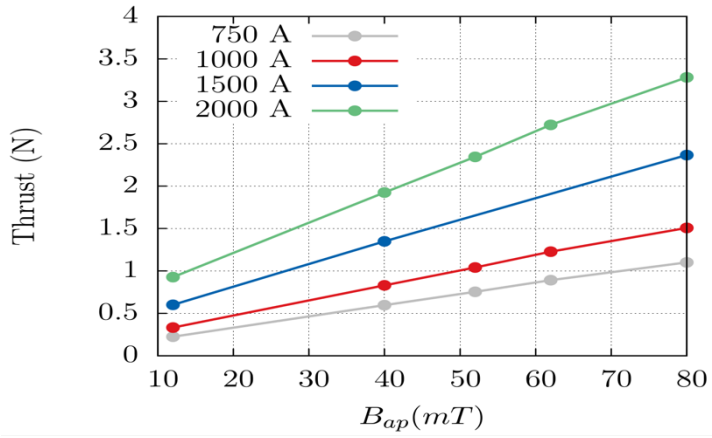

Fig. 3: Thrust [N] function of applied magnetic field strength.

Outside the MPD thruster, the acceleration is based on the conversion of the above mentioned rotational energy via expansion in a magnetic nozzle which is formed by the diverge magnetic field lines. The induced azimuthal currents interact with the applied magnetic field to produce a radially confining electromagnetic force. Fig. 3 presents thrust variation function of the applied magnetic field and discharge current. The code reproduced the increase of thrust for both case as predicted by some previous modelling and analytic works.

Outlook

In this project, we successfully used the developed density-based code for the simulations of the applied-field NASALeRC MPD thruster and the method presents ability to reproduce the theory of thrust production and plasma acceleration. For that we used a configuration with one external magnet and investigated the effect of applied magnetic strength and discharge current on the thruster performance. For the near future work it is planned to investigated the configuration (AFMPDT02) with two external magnets surrounding the discharge chamber in order to obtain a quasi uniform and horizontal applied field distribution near the anode to improve the thrust production as the swirl acceleration appeared as the most important component of thrust.

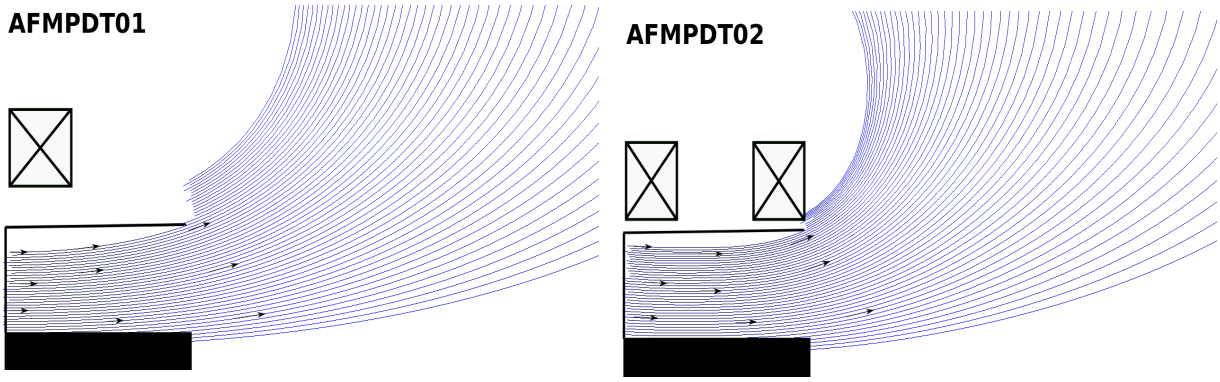

Fig. 4: Applied-field MPD thruster configurations considered in this project: one (left) and two (right) external magnet(s).

Publications

1. C. Chelem Mayigue, R. Groll, "*Performance investigation of an argon fueled magnetoplasmadynamic thruster with applied magnetic fields",* Submitted to Acta Astronautica

Acknowledgement

This work is funded by the *Deutscher Akademischer Austauschdienst* (DAAD) through the "Research grants for doctoral candidates and young academics and scientists" programme (grant number 57076385).

References

1. G. Krülle, M. Auweter-Kurtz, A. Sasoh, *Technology and application 335 aspects of applied field magnetoplasmadynamic propulsion*, Journal of Propulsion and Power 14 (5) (1998) 754–763. doi:10.2514/2.5338.

2. G. P. Mikellides, J. P. Turchi, F. N. Roderick, Applied-field magnetoplasmadynamic thrusters, part 1: Numerical simulations using the mach2 code, Journal of propulsion and power 16 (2000) 887–893. doi:10.2514/2.5656.

3. R. Albertoni, F. Paganucci, M. Andrenucci, A phenomenological performance model for applied-field mpd thrusters, Acta Astronautica 107 (2015) 177–186. doi.:10.1016/j.actaastro.2014.11.017

6.9 *hbk00018:* Berechnung der Wasserdampfkonzentrationen aus Limb-Messungen des Satelliteninstruments SCIAMACHY

HLRN-Projektkennung:	hbk00018
Laufzeit:	I/2012 – II/2017
Projektleiter:	Dr. K. Weigel
Projektbearbeiter.	Dr. K. Bramstedt, Dr. A. Rozanov, Dr. M. Vountas
Institut / Einrichtung:	Institut für Umweltphysik (IUP), Universität Bremen

Überblick

Im Rahmen der DFG-Forschergruppe SHARP (engl.: Stratospheric Change and ist Role for Climate Prediction) und des ESA-Projekte SPIN (engl: ESA SPARC Initiative) und SQWG (engl: SCIAMACHY Quality Working Group) arbeiten wir an einer neuen Version für einen Wasserdampfdatensatz der oberen Troposphäre und unteren Stratosphäre. Grundlage der Berechnung sind SCIAMACHY (engl.: Scanning Imaging Absorption spectroMeter for Atmospheric CHartographY) Messungen. SCIAMACHY, ein Instrument auf dem europäischen Satelliten Envisat, lieferte von August 2002 bis April 2012 Messungen. Die veröffentliche Datenversion V3.01 wurde teilweise auf dem HLRN berechnet, beinhaltet aber nur einen Teil der auswertbaren Daten. Diese Zeitserie wird auch durch die Initiativen SPARC-DI (engl.: Stratospheric Processes and their Role in Climate - Data Initiative) und SPARC - WAVAS (engl.: Water Vapour Assessment) genutzt. Zurzeit berechnen wir die neue Datenversion V4.2 für den kompletten Datensatz. Das ist jetzt mit einer Erweiterung von SCIATRAN, durch die zusätzlich zu openMP auch MPI genutzt werden kann, erstmalig möglich. Gegenüber V3.01 wurde V4.2 zusätzlich insbesondere hinsichtlich der vertikalen Auflösung und der Aerosolkorrektur verbessert.

Ergebnisse

Wasserdampf in der Atmosphäre ist im Gegensatz zu Wassertröpfchen, die man als Wolken oder Nebel sehen kann, für das menschliche Auge unsichtbar. Trotzdem spielt er eine wichtige Rolle für den Strahlungstransport in der Atmosphäre, denn er absorbiert besonders gut Strahlung im infraroten Bereich und somit z.B. die von der Erde emittierte Wärmestrahlung. Für das kurzwelligere, sichtbare Licht ist er dagegen fast vollständig transparent. Dadurch ist er das wichtigste natürliche Treibhausgas. Der Wasserdampfgehalt der Atmosphäre schwankt stark, sowohl örtlich als auch zeitlich. Den höchsten Wasserdampfgehalt findet man üblicherweise nahe dem Erdboden. An der Tropopause, d.h. am Übergang zwischen Troposphäre und Stratosphäre gibt es meist besonders wenig Wasserdampf. Die Troposphäre reicht bis in eine Höhe von etwa 10 bis 18 km und ist die Schicht, in der sich die meisten Wetterphänomene abspielen. Wolken findet man beispielsweise meist in der Troposphäre und nur unter bestimmten Bedingungen in der Stratosphäre. Das Wasserdampfminimum in der Nähe der Tropopause (siehe auch Abb. 1) hat einen großen Einfluss auf den Strahlungstransport. Modellstudien haben gezeigt, dass Änderungen des Wasserdampfgehaltes dort auch das Klima am Boden beeinflussen können. Ziel des DFG Projektes SHARP (siehe auch: www.fu-berlin.de/sharp/) ist es, zu einem besseren Verständnis über die Verteilung und die zeitliche Änderung des Wasserdampfgehaltes in der Atmosphäre und dessen Wirkung auf das Klima beizutragen.

Um dieses Wasserdampfminimum beobachten zu können braucht man sehr empfindliche Instrumente. Bodengebundene Messverfahren erreichen diesen Höhenbereich oft nur schlecht, Messungen von Ballonen und Flugzeugen sind nicht global und regelmäßig in ausreichender Qualität verfügbar. Limb-Messverfahren von Satelliteninstrumenten sind besonders gut geeignet um den Bereich der Tropopause zu beobachten. Bei diesem Messverfahren schaut das Instrument durch die Atmosphäre über den Erdboden hinweg in Richtung des Weltraumes und kann so verschiedene Höhen abtasten. Solche Messungen wurden von SCIAMACHY (engl.: Scanning Imaging Absorption spectroMeter for Atmospheric CHartographY) durchgeführt, einem Spektrometer an Bord des europäischen Satelliten Envisat. Beim Limb-Messverfahren tastet SCIAMACHY die Atmosphäre mit Höhenschritten von jeweils 3.3 km ab. Bei jedem Höhenschritt wird das Spektrum des in der Atmosphäre gestreuten Sonnenlichts über einen breiten Wellenlängenbereich aufgezeichnet. Absorptionslinien des Wasserdampfes im infraroten Bereich des Spektrums ermöglichen es, den Wasserdampfgehalt der Atmosphäre zu bestimmen. Das gemessene Spektrum wird außer vom Wasserdampfgehalt auch durch Druck, Temperatur und die Streuung in der Atmosphäre z.B. an Aerosolen und Wolken beeinflusst.

Um Wasserdampfprofile aus den gemessen Spektren zu bestimmen verwenden wir SCIATRAN (Rozanov et al., 2011). Dabei wird mit einem Strahlungstransportmodell aus einer gegebenen Atmosphäre ein solches Spektrum berechnet, wobei auch die Mehrfachstreuung modelliert wird. Um aus den Messungen und den modellierten Spektren auf Wasserdampfprofile in der Atmosphäre zu schließen sind aufwändige, inverse mathematische Verfahren nötig. Das Ergebnis sind Wasserdampfprofile zwischen ca. 10 und 25 km Höhe. Die Berechnungen erfolgen iterativ und der Zeitaufwand ist groß, unter anderem weil ein breiter Spektralbereich und ein dichtes Höhengitter verwendet werden müssen. Dazu kommt die große Zahl von Profilen, die berechnet werden kann. SCIAMACHY Messungen gibt es von August 2002 bis zum plötzlichen Kontaktverlust mit Envisat im April 2012. In diesem Zeitraum gibt es etwa 4.5 Millionen Limb-Messungen bei Tageslicht, die sich prinzipiell für die Berechnung des Wasserdampfgehaltes eignen. Das sind über 1000 Profile pro Messtag. Mit einem Wolkenfilter werden zunächst die Profile identifiziert, bei denen hohe Wolken eine Auswertung erschweren. Nach der Filterung bleiben etwa 700 Profile pro Messtag übrig, die Zahl der Profile reduziert sich besonders in der Nähe des Äquators. Deshalb wurde für die letzte Datenversion V3.01 nur jeder 8. Tag global und jeder 2.Tag zwischen 45°N und 45°S ausgewertet.

Die Datenversion V3.01 haben wir mit verschiedenen Datensätzen von anderen Satelliteninstrumenten und Ballonmessungen verglichen und die Berechnung anhand von simulierten Messungen überprüft, siehe Weigel et al. (2016). Die Wasserdampfdaten werden im Rahmen internationaler Initiativen wie SPARC-DI (engl.: Stratospheric Processes and their Role in Climate - Data Initiative) und SPARC - WAVAS (engl.: Water Vapour Assessment) zur Erforschung der Stratosphäre genutzt und mit anderen Daten verglichen, siehe Hegglin et al. (2013; 2014) und Lossow et al. (2017). Der Datensatz wird auch bei einer Studie zu Polaren Stratosphärenwolken verwendet (Khosrawi et al., 2016).

Für die neue Datenversion V4.2 wurde die Rechenmethode verbessert, insbesondere hinsichtlich der Aerosolkorrektur und der Höhenauflösung. Mit der neuen SCIATRAN Version 3.5 ist es nun möglich, zusätzlich zur bisher verwendeten openMP Parallelisierung auch eine Parallelisierung mit Hilfe von MPI (engl.: message passing interface) zu verwenden. Dadurch konnten die Berechnung auf dem HLRN deutlich besser organisiert werden. Wir erwarten, dass wir damit jetzt für die Datenversion 4.2 den kompletten Datensatz auswerten können. Bisher wurden alle Daten zwischen 45°S und 45°N ausgewertet und von den Daten polwärts dieser Region etwa jede 2. Woche. Abb. 1 zeigt für diesen Datensatz das Minimum des

Wasserdampf-Volumenmischungsverhältnisses und seine Höhe gemittelt über alle Längengrade und 5° Breitengradbereiche.

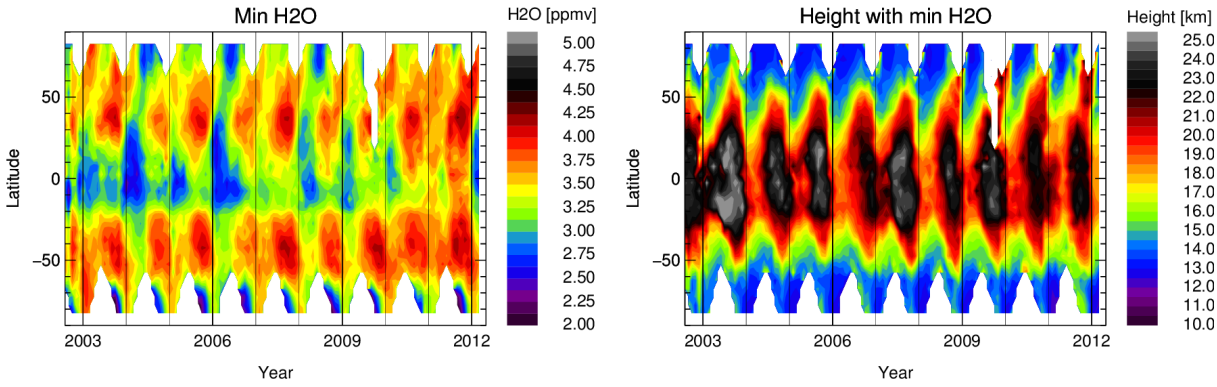

Abb. 1: Zeitserie des Minimums des Wasserdampf-Volumenmischungsverhältnisses (links) und seine Höhe (rechts) gemittelt über alle Längengrade und 5° Breitengradbereiche für die neue Datenversion V4.2, für alle Daten zwischen 45°S und 45°N und etwa jede 2. Woche polwärts dieser Region.

Ausblick

Wir erwarten die Zeitserie für die Datenversion V4.2 im 2. Quartal 2017 vervollständigen zu können und damit das Projekt hbk00018 abzuschließen.

Publikationen

1. Rozanov, A., Weigel, K., Bovensmann, H., Dhomse, S., Eichmann, K.-U., Kivi, R., Rozanov, V., Vömel, H., Weber, M., and Burrows, J. P., *Retrieval of water vapor vertical distributions in the upper troposphere and the lower stratosphere from SCIAMACHY limb measurements*, Atmos. Meas. Techn., 4, 933-954, doi:10.5194/amt-4-933-2011, 2011.
2. Hegglin, M. I., Tegtmeier, S., Anderson, J., Froidevaux, L., Fuller, R., Funke, B., Jones, A., Lingenfelser, G., Lumpe, J., Pendlebury, D. , Remsberg, E., Rozanov, A., Toohey, M., Urban, J., von Clarmann, T., Walker, K. A., Wang, R., Weigel, K.: *SPARC Data Initiative: Comparison of water vapour climatologies from international satellite limb sounders*, J.Geophys. Res., 118, 20, 11824–11846, doi: 10.1002/jgrd.50752, 2013.
3. Hegglin, M. I., Plummer, D. A., Shepherd, T. G., Scinocca, J. F., Anderson, J., Froidevaux, L. Funke, B., Hurst, D., Rozanov, A., Urban, J., von Clarmann, T., Walker, K. A., Wang, H. J., Tegtmeier, S., and Weigel, K.: *Vertical structure of stratospheric water vapour trends derived from merged satellite data*, Nature Geosc., 7, 768–776, doi:10.1038/ngeo2236, 2014.
4. Khosrawi, F., Urban, J., Lossow, S., Stiller, G., Weigel, K., Braesicke, P., Pitts, M. C., Rozanov, A., Burrows, J. P., and Murtagh, D.*: Sensitivity of polar stratospheric cloud formation to changes in water vapour and temperature*, Atmos. Chem. Phys., 16, 101-121, doi:10.5194/acp-16-101-2016, 2016.
5. Weigel, K., Rozanov, A., Azam, F., Bramstedt, K., Damadeo, R., Eichmann, K.-U., Gebhardt, C., Hurst, D., Kraemer, M., Lossow, S., Read, W., Spelten, N., Stiller, G. P., Walker, K. A., Weber, M., Bovensmann, H., and Burrows, J. P.: *UTLS water vapour from SCIAMACHY limb measurements V3.01 (2002–2012)*, Atmos. Meas. Tech., 9, 133-158, doi:10.5194/amt-9-133-2016, 2016.
6. Lossow, S., Khosrawi, F., Nedoluha, G. E., Azam, F., Bramstedt, K., Burrows, John. P., Dinelli, B. M., Eriksson, P., Espy, P. J., García-Comas, M., Gille, J. C., Kiefer, M., Noël,

S., Raspollini, P., Read, W. G., Rosenlof, K. H., Rozanov, A., Sioris, C. E., Stiller, G. P., Walker, K. A., and Weigel, K.: *The SPARC water vapour assessment II: comparison of annual, semi-annual and quasi-biennial variations in stratospheric and lower mesospheric water vapour observed from satellites*, Atmos. Meas. Tech., 10, 1111-1137, doi:10.5194/amt-10-1111-2017, 2017.

Vorträge / Poster

1. Weigel, K., Rozanov, A., Azam, F., Bramstedt, K., Kowalewski, S., Eichmann, K.-U., Noël, S., Weber, M., Bovensmann, H., andBurrows, J. P.: *A new version of water vapour profile data from SCIAMACHY limb measurements*, ESA Living Planet Symposium 2016 - LPS16, Praha, 12.05.2016.
2. Weigel, K., Rozanov, A., Azam, F., Bramstedt, K., Eichmann, K.-U., Stiller, G. P., Weber, M., Bovensmann, H., and Burrows, J. P.: *Validation of SCIAMACHY Limb Water Vapour V4.2*, Atmospheric Composition Validation and Evolution Workshop - ACVE 2016, ESA/ESRIN, Italy, 18-20 October 2016.
3. Weigel, K., Rozanov, A., Azam, F., Bramstedt, K., Eichmann, K.-U., Malinina, E., Weber, M., Bovensmann, H., and Burrows, J. P.: *SCIAMACHY limb measurements - one decade of observations in the upper troposphere and stratosphere*, WCRP/SPARC workshop: "Challenges for Climate Science - Synergies between SPARC and the WCRP Grand Challenges", Berlin, 31 October - 1 November 2016.

6.10 *hbk00032:* Improving physics and efficiency of AWI-CM multi-resolution climate model

HLRN-Projektkennung	hbk00032
Laufzeit:	III/2016–II/2017
Projektleiter	Prof. Dr. Thomas Jung [1]
Projektbearbeiter:	Dmitry Sidorenko [2], Dirk Barbi, Sergey Danilov, Helge Gößling, Ozgur Gurses, Sven Harig, Jan Hegewald, Nikolay Koldunov, Thomas Rackow, Natalja Rakowsky, Dmitry Sein, Tido Semmler, Qiang Wang, Claudia Wekerle
Institut / Einrichtung:	[1] also at University of Bremen [2]Alfred-Wegener-Institute for Polar and Marine Research, Bremerhaven

Summary

In this project we use the AWI-CM climate model which is built upon FESOM (Finite Element Sea Ice-Ocean Model v. 1.4) coupled to the latest version of ECHAM6.3 from the Max Planck Institute for Meteorology, Hamburg. Our main goal is to prepare the AWI-CM for CMIP6-type simulations. To achieve it we work on improvement of simulation quality by exploiting two complementary approaches. First, we work on reduction of the model biases caused by imperfectness of parameterizations of subgrid-scale processes. We limit our focus to eddy stirring and mixing and to the processes within the boundary layer below the ice cover. Second, we improve the quality of simulated solutions by refining the FESOM mesh over the key oceanic fronts. This is possible because of the multi-resolution layout of FESOM. The identification of key areas where the high resolution is of climate importance, is the main question of the second approach. Only minor changes are introduced to the ECHAM6.3, mainly related to the coupling technique.

Existing configurations

Currently, a selection of oceanic meshes is used within AWI-CM framework and some of the configurations are shown in Fig. 1. The relatively low cost of the "coarse" mesh allows efficient debugging of the coupled model and tests of new implementations. The configuration of T63/L47 atmosphere and "coarse" FESOM simulates ca. 30 years per day running on 12 nodes. The "ref." ocean is primarily used for testing the changes introduced to parameterization schemes. The configuration of T63/L47 atmosphere and "ref." ocean simulates ca. 30 years per day running on 28 nodes and produces climate trajectories with the quality compared to the most of the CMIP models. Any improvement made to "ref." climate is then tested with the configuration of the "fine" FESOM and T127/L95 version of ECHAM6 which is the target for the CMIP6. The design for the "fine"-type meshes takes into account the variance of sea surface hight (provided by satellite altimetry), the behavior of the Rossby radius of deformation and coastline geometry (see eg. Sein et al. 2016). In addition, different weighting between regions can be applied. Simulations with “fine” meshes are relatively expensive and one reaches ca. 6 years per day running on 128 nodes.

It is worth mentioning, that the common biases in general circulation ocean models (GCMs), such as the Gulf Stream separation or the Northwest Corner cold bias around Newfoundland, are significantly reduced in "fine" setups as compared to "ref." setup or simulations with other GCMs of similar resolution. This indicates that the eddy-permitting resolution is required along main fronts of the current systems in order to maintain their realistic positions.

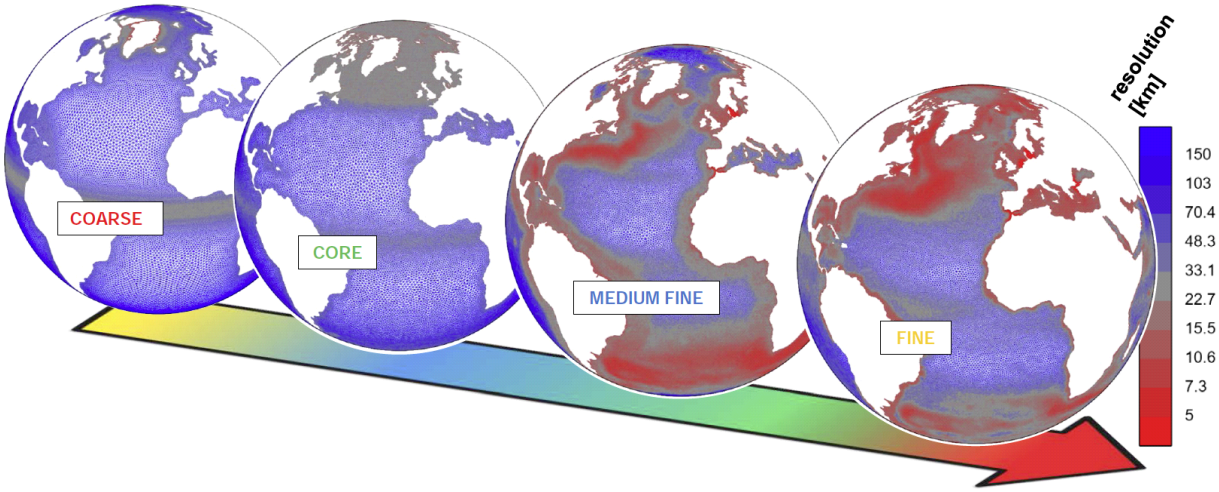

Figure 1: meshes, which are currently used by AWI-CM. **COARSE** and **CORE** meshes have a resolution of ca. 1° on average and consist of ca. 87,000 and 126,000 surface nodes, respectively. **MEDIUM FINE** and **FINE** meshes are the prototypes for the CMIP6 and contain ca. 830,000 and 1,3000,000 surface nodes respectively. The design of the FINE-type meshes takes into account the variance of satellite altimetry, Rossby radius of deformation and the coastline geometry.

Sea Surface Salinity bias

We run AWI-CM under the pre-industrial climate conditions with "ref." configuration and compare the simulated spatial distribution of surface temperature (SST) and salinity (SSS) to other CMIP5 participants. While in the most parts of the global ocean the spatial distributions in AWI-CM were similar to the most of CMIP5 models, the SSS in the central Arctic was found to be an outlier with far too high surface salinity. Fig. 2 (upper panel) shows the simulated SSS difference to the reference, which we choose as PHC 2.1 climatology. Recall that this climatology is not representative for the pre-industrial climate. Nevertheless, much smaller departures of SSS from PHC 2.1 were observed for other pre-industrial trajectories from CMIP5 (not shown). The SSS bias persisted even if FESOM was configured with higher resolution in the Arctic and Nordic Seas and even if the atmospheric configuration was changed to T127/L95. We concluded that the source of the bias is most probably the imperfectness in parameterization of the boundary layer physics. Its reduction could be achieved by changing model parameters, such as the lead closing or salinity of the sea ice. However, the successful reduction required the parameter values which are outside the well established range.

Salt plume parameterization

Further inspection of the SSS bias in the central Arctic pointed to the treatment of the brine rejection in FESOM. Indeed, most ocean GCMs apply the rejected salt during the sea ice formation at the ocean surface. As it has been already mentioned in literature (see, e.g., Duffy and Caldeira 1997, Duffy et al. 1999, Nguyen et al., 2009) in reality, the rejected salt does not stay at the ocean surface but forms so-called salt plumes which penetrate down to

the bottom of the mixed layer. The lack of the salt plume physics in FESOM was guessed to be the prime reason for the bias shown in fig. 2. (upper panel). Also (see, e.g., the discussion by Nguyen et al., 2009), when the salt plume penetration is not accounted for in a GCM, the vertical mixing scheme reacts to the decreased static stability of the upper water column and may potentially destroy the upper picnocline. Therefore, Nguyen et al., 2009 suggested to parameterize the salt plume physics by applying the rejected salt using a power-law profile within the mixed layer. This idea has been also incorporated into FESOM and first tested with ocean only configurations. The effect on simulated SSS was, however, only minor since any ocean only model run is commonly conducted under applied restoring to climatological SSS. The effect in the coupled model, where the surface salinity is free to evolve, has not yet been studied.

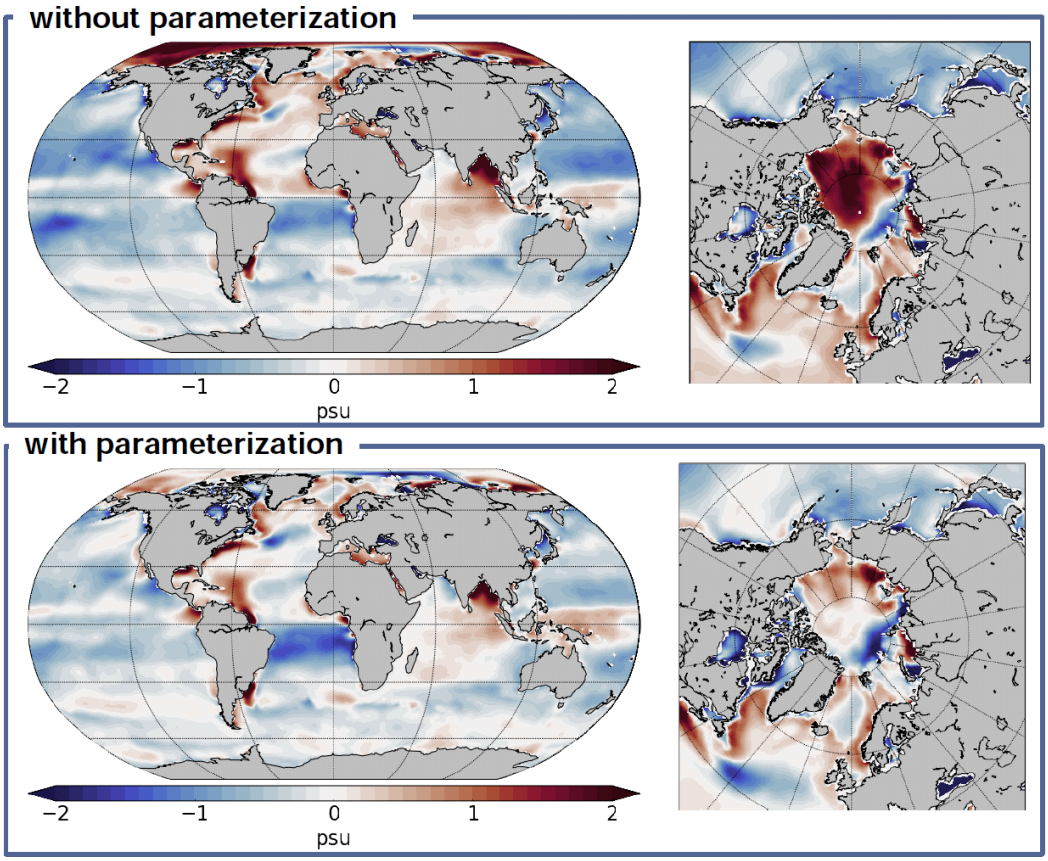

Figure 2: the upper panel shows the departure of SSS from PHC 2.1 climatology for AWI-CM integration without applying the salt plume parameterization. The average over last 50 years of integration is considered. The lower panel shows the same when salt plume parameterization was applied.

We conducted a 200 year run with “ref.“ AWI-CM using salt plume parameterization from Nguyen et al., 2009. The simulated SSS pattern averaged over last 50 years of simulation is shown in fig. 2 (lower panel). The results indicate that the significant part of the SSS bias in the Arctic ocean has been removed when the parameterization was used. Furthermore, analyzing the impact of the parameterization onto the simulated climate we found that it modifies the properties of deep waters in the regions of ventilation and by doing so impacts the whole thermohaline circulation. The detailed diagnostics is still ongoing but it can be already said that the change introduced by parameterization of salinity plumes improved the

quality of the "ref." climate. The salt plume parameterization is currently being tested with the "fine" model setup to prove its applicability for CMIP6.

References

Duffy, P., and K. Caldeira (1997), Sensitivity of simulated salinity in a three-dimensional ocean model to upper ocean transport of salt from sea-ice formation, Geophys. Res. Lett., 24(11), 1323–1326.

Duffy, P., M. Eby, and A. Weaver (1999), Effects of sinking of salt rejected during formation of sea ice on results of an ocean-atmosphere-sea ice climate model, Geophys. Res. Lett., 26(12), 1739–1742.

Nguyen, A. T., D. Menemenlis, and R. Kwok (2009), Improved modeling of the Arctic halocline with a subgrid-scale brine rejection parameterization, J. Geophys. Res., 114, C11014, doi:10.1029/2008JC005121.

Sein, D. V., Danilov, S. , Biastoch, A. , Durgadoo, J. V. , Sidorenko, D. , Harig, S. and Wang, Q. (2016), Designing variable ocean model resolution based on the observed ocean variability, Journal of Advances in Modeling Earth Systems, 8 (2), pp. 904-916, doi:10.1002/2016MS000650

6.11 *hbk00034:* Ice sheet - ice shelf - ocean interaction in the marginal seas of the Southern Ocean
hbk00038: Interaction between marine terminating glaciers and the ocean circulation in Northeast Greenland

HLRN Project ID:	hbk00034 / hbk00038
Run time:	III/2013-III/2017 / III/2014 – II/2017
Project Leader:	Prof. Torsten Kanzow[1,2]
Project Scientists:	Dr. Mathias van Caspel[2], Marta Kasper[2], Svenja Ryan[2], Janin Schaffer[2], Frank Schnaase[1], Lukrecia Stulic[2], Dr. Ralph Timmermann[2], Dr. Claudia Wekerle[2]
Affiliation:	[1] University of Bremen [2] Alfred Wegener Institute, Helmholtz Centre for Polar and Marine Research

Overview

In these projects, we use a global sea ice – ice shelf – ocean model to study the interaction between the deep ocean, the ice shelves fringing the Antarctic continent and part of the Greenland coast, and the ice sheets of Antarctica and Greenland. With its unstructured grid, the Finite Element Sea ice Ocean Model (FESOM) allows for an adequate resolution of the key regions, namely the grounding lines, the ice shelf fronts, and the continental shelf break. Special emphasis is laid on a correct representation of water mass exchange between the deep ocean and the continental shelf regions, and the pathways of water in the cavity beneath Filchner-Ronne Ice Shelf (FRIS) and the 79-North Glacier. Coupling with dynamic ice sheet/shelf models is one of the key activities in these projects and will allow for a complete and consistent representation of ocean – ice sheet interaction in decadal- to centennial-scale simulations. With the high computational burden imposed by the use of a finite-element ocean model (to which there is no alternative if local processes are to be represented in a global system), the projects depend on resources provided through the HLRN.

Results

We have recently completed a suite of centennial-scale simulations with the coupled Regional Antarctic and Global Ocean (RAnGO) model; results are currently being prepared for publication. RAnGO is based on a global FESOM configuration with an eddy-permitting mesh in the Weddell Sea sector of the Southern Ocean and an even further refinement in the sub-ice cavities. It is coupled to an implementation of the three-dimensional ice dynamics model RIMBAY that comprises the FRIS and the ice streams in its catchment area up to the ice divides with a terrain-following vertical coordinate and 10 km horizontal resolution.

As the reference simulation, we analyzed a coupled model run forced with A1B scenario data from the HadCM3 climate model. Similar to earlier experiments in a different configuration, a substantial increase of FRIS basal melt rates during the 21st/22nd centuries occurs as a response to a redirected coastal current (Fig. 1). This event does not occur in two control simulations (coupled/uncoupled) with a perpetual 20th-century forcing from the same climate model and can thus clearly be attributed to the climate scenario/forcing data used.

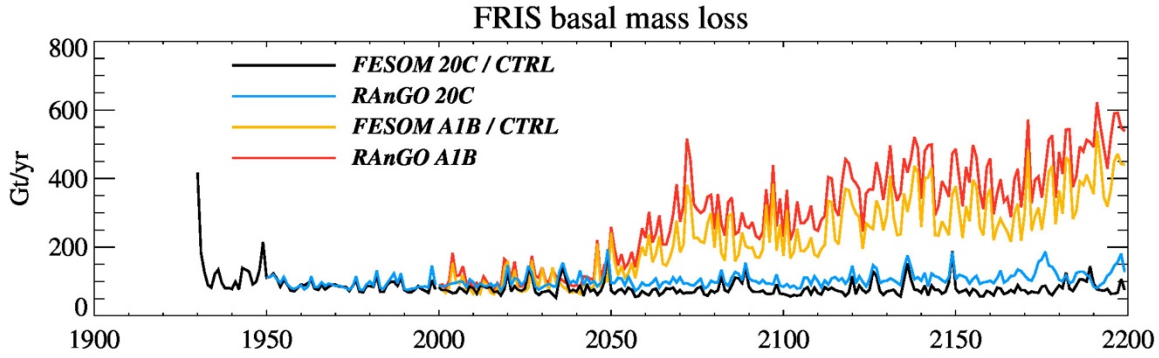

Fig.1: Time series of annual-mean basal melt rate for FRIS in fixed-geometry FESOM experiments with 20th-century (black line) and A1B (yellow line) forcing and in RAnGO experiments for the 20th century (blue line) and the A1B scenario (redline).

Basal mass loss in the coupled A1B simulation increases by a factor of six between the simulated 1990s and the projected 2190s; maximum melt rates near the grounding line increase from 4 to 15~m/yr. Simulated ice-shelf thickness is reduced by almost 25% near the grounding line of Support Force Glacier.

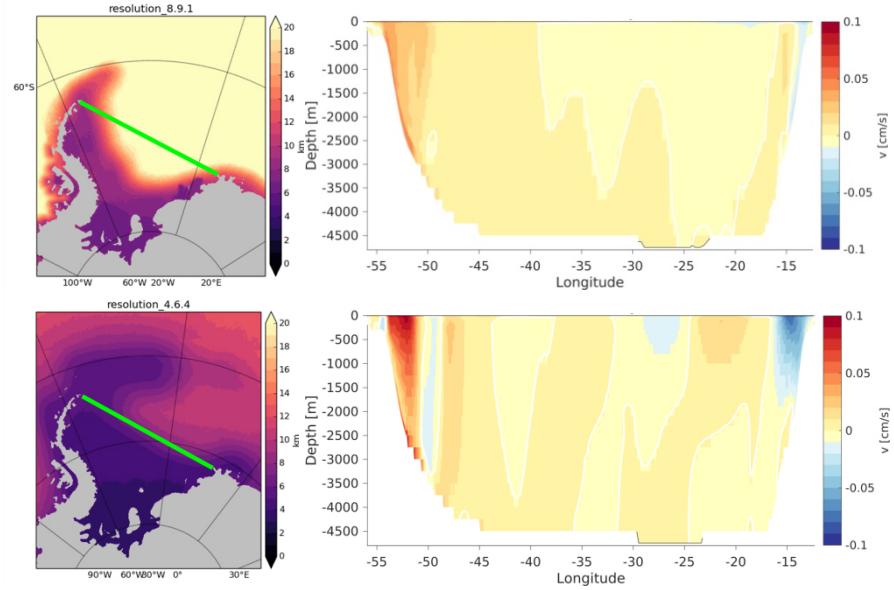

Fig.2: Horizontal resolution of our coarse-resolution workhose mesh (top left) and a velocity section across the Weddell Gyre from Kapp Norwegia to the Antarctic Peninsula (top right) obtained with this mesh. Bottom row: JEDDY mesh resolution and velocity section at the same locations.

To improve the representation of Weddell Sea hydrography in FESOM, particularly the modelled dynamics of the Antarctic Slope Front, we developed a new global mesh with an eddy-permitting/eddy-resolving resolution over the whole Weddell Sea and an additional focussing over the continental shelf (Figure 2, left panels). First results of these Joint Eddy (JEDDY) experiments show a significant improvement of the Antarctic Slope current, which transports the Warm Deep Water (WDW) along the shelf break. A comparison of simulated velocity sections in the Weddell Sea from the low- and high-resolution meshes (Figure 2,

right panels) shows that after 5 years, the slope current has significantly degraded in the coarse-resultion run along with an erosion of WDW, while both are maintained much better in the new high-resolution mesh. This proves the importance of mesocale processes even for such large-scale features.

In the northern hemisphere, our activities focus on the interaction between the deep ocean and the cavity beneath the 79-North Glacier (Nioghalvfjerdsbrae). Our current workhorse configuration here uses has a horizontal resolution of about 1° in the vast open ocean, 0.5° along the coastlines, and 24 km in the North Atlantic. We apply a mesh with 4.5 km resolution in the Arctic Ocean and Nordic Seas and 1 km resolution in Fram Strait and on the Northeast Greenland continental shelf to better resolve the flow of Atlantic Waters towards the ice shelf. In contrast to earlier, coarser configurations with a resolution of 4.5 km in Fram Strait, the recirculation ot Atlantic Water in the northern Greenland Sea is now nicely captured by the model. The optimized model also reveals a recirculation of warm waters in the Norske Trough east of 14°W (Fig. 3). This is also suggested by hydrographic observations and most likely caused by a bathymetric sill of 360 m depth located at 14°W. However, a good representation of the deep shelf circulation in the inner part of the continental shelf remains challenging. Recently obtained moored observations (at about 78°N, 15°W) showed evidence for a boundary current flowing along the northeastern slope of Norske Trough towards the 79 North Glacier, which is not yet captured by the model.

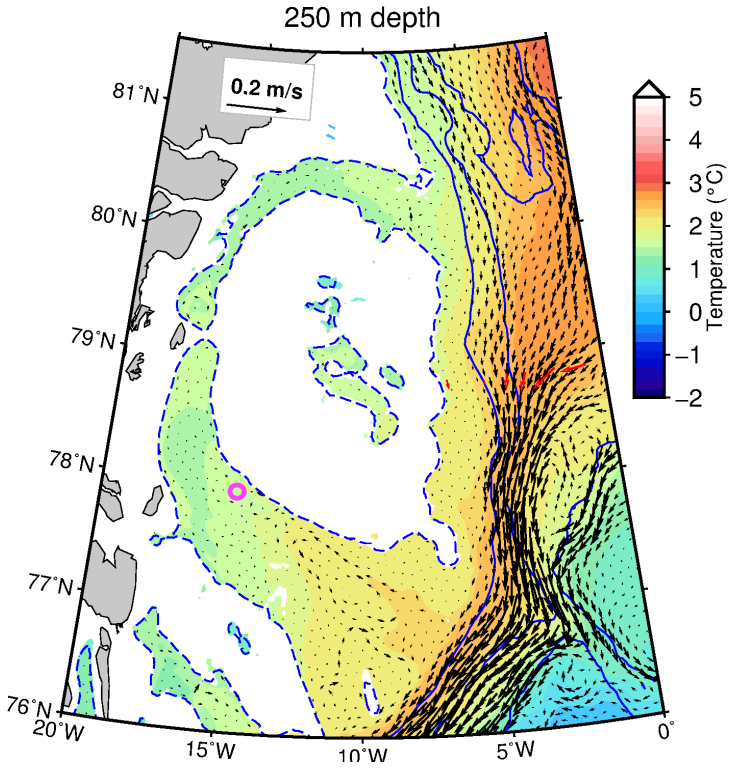

Fig. 3: Simulated annual mean temperature distribution (colours) and ocean currents (vectors) on the continental shelf off Northeast Greenland. Grey shading indicates land; the dashed blue line indicates the 250 m isobath; solid blue lines indicate depth levels in 1000 m intervals. Red arrows show annual mean velocities obtained from moored observations in Fram Strait. The pink circle marks the mooring position, where we recently observed a northwestward flowing boundary current.

Outlook

Building on the experience gained with RAnGO and the JEDDY experiments, we plan to pursue high-resolution ice-ocean coupled simulations for both hemispheres. For the southern hemisphere, coupling FESOM to a pan-Antarctic configuration of the Parallel Ice Sheet Model (PISM) is planned. For Greenland, we plan to couple an optimized FESOM configuration (which may or may not be in a regional domain for this particular purpose) to the finite-element Ice Sheet System Model (ISSM) in a setup focussed on the Northeast-Greenland Ice Stream. Funding for both projects has been ensured; we will apply for the necessary computing time at HLRN later this year.

Publications

1. Rücker van Caspel, M., *The importance of the western Weddell Sea to Weddell Sea Deep Water formation*, PhD thesis, Universität Bremen, 2016.

Presentations / Posters

1. Goeller, S. and Timmermann, R., *Feedbacks between ice and ocean dynamics at the West Antarctic Filchner-Ronne Ice Shelf in future global warming scenarios*, European Geoscience Union, General Assembly, Vienna, Austria, 23 April 2016.
2. Marta Kasper, *Modeling present day Southern Ocean circulationusing the Finite Element Sea-ice Ocean Model (FESOM) and RACMO2.3*, International FRISP Workshop 3-6 October 2016, Gothenburg.
3. Stulic, L., Timmermann, R., Zentek, R., Heinemann, G., Paul, S., Ryan, S., *Quantification of sea ice production in the Weddell Sea coastal polynyas*, International FRISP Workshop 3-6 October 2016, Gothenburg.
4. Timmermann, R. and Goeller, S., *Towards a regional coupled ice sheet - ocean model for Antarctica*, Rising Coastal Seas on a Warming Earth II, NYU Abu Dhabi, 16 May 2016 - 18 May 2016.

6.12 *hbk00042:* Climatic evolution in the marginal seas of the Northwest Pacific Ocean since the last glacial period until present day: changes in the formation of North Pacific Intermediate Water formation and their implications on the Pacific realm

HLRN Project ID:	hbk00042
Run time:	I/2015 – III/2017
Project Leader:	Prof. G. Lohmann
Project Scientists:	Dr. P. Scholz, Dr. X. Gong
Affiliation:	Alfred Wegener Institute Helmholtz Center for Polar and Marine Research

Overview

The aim of this project is to simulate the variability of the sea ice cover, general ocean circulation and hydrology of the marginal seas in the Northwest Pacific Ocean as well as the Arctic Ocean on different time-slices since the last glacial period up to present day (e.g. last glacial maximum (LGM, 21000 years ago), mid (6000 years ago) Holocene, pre-industrial as well as present day).
A particular focus will be on the Sea of Okhotsk, which has nowadays a significant role in the climate system of the Northwest Pacific by influencing the atmospheric and oceanic circulation as well as the hydrology of the Pacific water masses. In the Sea of Okhotsk, the so called Sea of Okhotsk Intermediate Water (SOIW) is formed, which in turn contributes to the vertical ventilation in the North Pacific and to the mid-depth water masses of the North Pacific Intermediate Water (NPIW). NPIW is one of the key elements for the nutrient and oxygen supply of the low latitude Pacific Ocean realm.
As such the main question of this project is: How the role of the Sea of Okhotsk and the other marginal Seas (e.g. Bering Sea) as a source for NPIW has changed during the different climatological time-slices since the last glacial period? Beyond the regional focus on the marginal seas of the Northwest Pacific, this project should also clarify what are the large scale implications and teleconnections of the changes in NPIW.
To find a compromise between a global coverage and a regional highly increased resolution, which is necessary to adequately reproduce the deep and intermediate water formation, at relatively moderate computational costs, we will use in this project the Finite-Element Sea-Ice Ocean Model (FESOM).

Previous simulation of the present-day time-slice revealed significant deficiencies in the vertical stratification of the marginal seas of the Northwest Pacific Ocean when compared with observational data. The comparison showed a tremendous deviation between the modeled and observed temperature and salinity over depth and time in the southern Sea of Okhotsk, especially in depths below 200 m. There, the modeled temperature and salinity features a constant warming and excess in salinity over the entire considered period of around 1.5°C to 2.0°C and ~0.5 psu, respectively compared to the observed values.
The magnitude of the modeled heat and salinity excess in the Sea of Okhotsk linked to an systematic problem in the model. This could be connected to the North Pacific gyre system, consisting of northern subpolar gyre and northern subtropical gyre, which is responsible for

transporting and distributing massive amounts of heat and salt into high latitudes. We could trace back this warming anomaly in the model throughout the entire northern branch of the subpolar pacific gyre and found its possible origin in problems with the Kuroshio Extension Current (KEC) in the model (not shown). It revealed that the detachment and position of the KEC is shifted by around 2° to 3° degree to the north when compared to reality. Also the modeled pathway of the KEC is tilted slightly to the north, although observational data let suggest thats its slightly tilted to the south, as well as the modeled strength of the KEC is overestimated. Due to this, too much warm waters from the subtropical pacific gyre could reach to the north and enter the branch of the subpolar pacific gyre and causes the warming anomaly in the Sea of Okhotsk. The deficiencies in the KEC and the associated warming anomaly was consistent through all spinup cycles that was carried out and was thus not an issue that could have been solved by a further improvement due to more spinup cycles. The factor of the external atmospheric forcing was already excluded by earlier tests. This caused us to search for other possibilities to improve our model results (e.g. mesh improvements, local corrections of the forcing, improvements in the parameterization of the model). First we tried to locally improve the resolution of our mesh configuration.

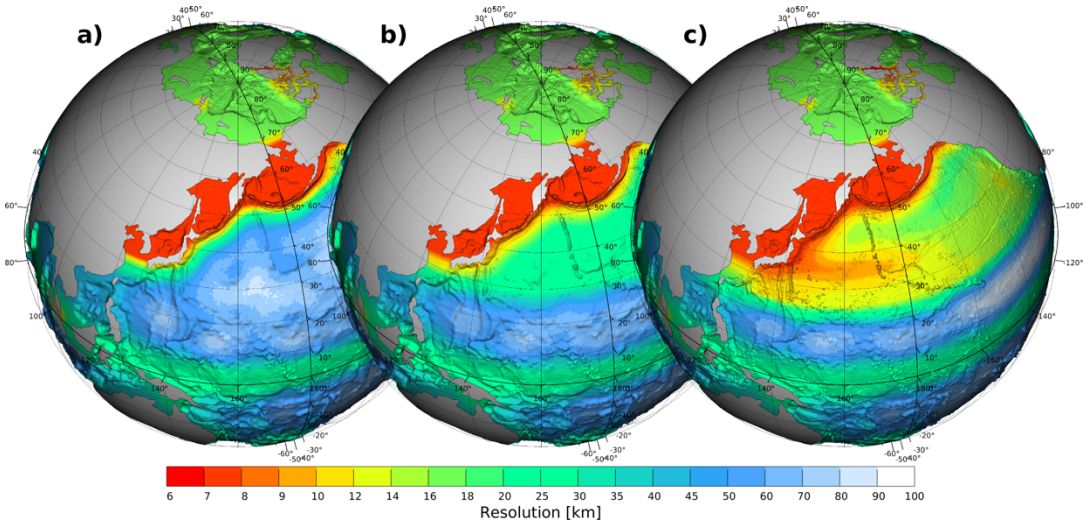

Fig 1. (a)-(c): Approximated mesh resolution of the four customized global FESOM configuration, with a general regional focus on the marginal Seas of the Northwest Pacific Ocean (e.g. Yellow Sea, Sea of Japan, Sea of Okhotsk and Bering Sea) as well as different resolutions in the area of the KEC and Northern Equatorial Current (NEC). All setups have a minimum resolution of ~ 6 − 8 km in the Sea of Okhotsk but different resolutions in the area of the KEC and NEC.

Test Resolution dependence of Kuroshio Extension Current (KEC) Region

The Kuroshio Current (KC) transports in the Pacific Ocean in analogy the Gulf Stream in the Atlantic Ocean large quantities of warm and saline water from the western equatorial warm pool first northward and then eastward into the North Pacific. After detaching from the coast of Japan and turning eastward, the KC turns into the KEC which crosses the Pacific. The KEC is one of the currents that separates the colder and fresher water masses of the subpolar gyre from the warm and saline water masses of the subtropical gyre. To test the resolution dependence of the detachment, confinement and stability of the KEC we analyze the modeled magnitude of the horizontal temperature gradient averaged between a depth of 200 m to 500 m for three different FESOM configurations with low (Fig. 2a, Fig. 3a), intermediate (Fig. 2b, Fig. 3b) and high (Fig. 2c, Fig. 3c) resolution in the area of the KEC and compare them to the observational derived horizontal temperature gradient averaged

between a depth of 200 m to 500 m (Fig. 3d). In the coarse setup (Fig. 3a) no clear branch for the KEC is present. The detachment point is to far in the north and the temperature gradient is immediately dissipating after detaching from the coast of Japan. For the intermediate (Fig. 3b) and higher (Fig. 3c) resolved setup a clear development of an eastward directed KEC branch is noticeable. The magnitude of the temperature gradient is spatially stronger confined and shows a more extended stability in the higher resolved setup when compared to the intermediate setup. Also the detachment point of the KEC in the setup with highest resolution in that area is much closer to the observed detachment point at around 36°N. As an outcome of this test we can summarize that we need a resolution between 7 km and 20 km in the area of the KEC to be able to simulate the detachment, stability and confinement close to reality. It should be mentioned that the pathway of the KEC for all modeled setups is slightly tilted to the north, whereas the observational derived KEC pathway is slightly tilted to the south.

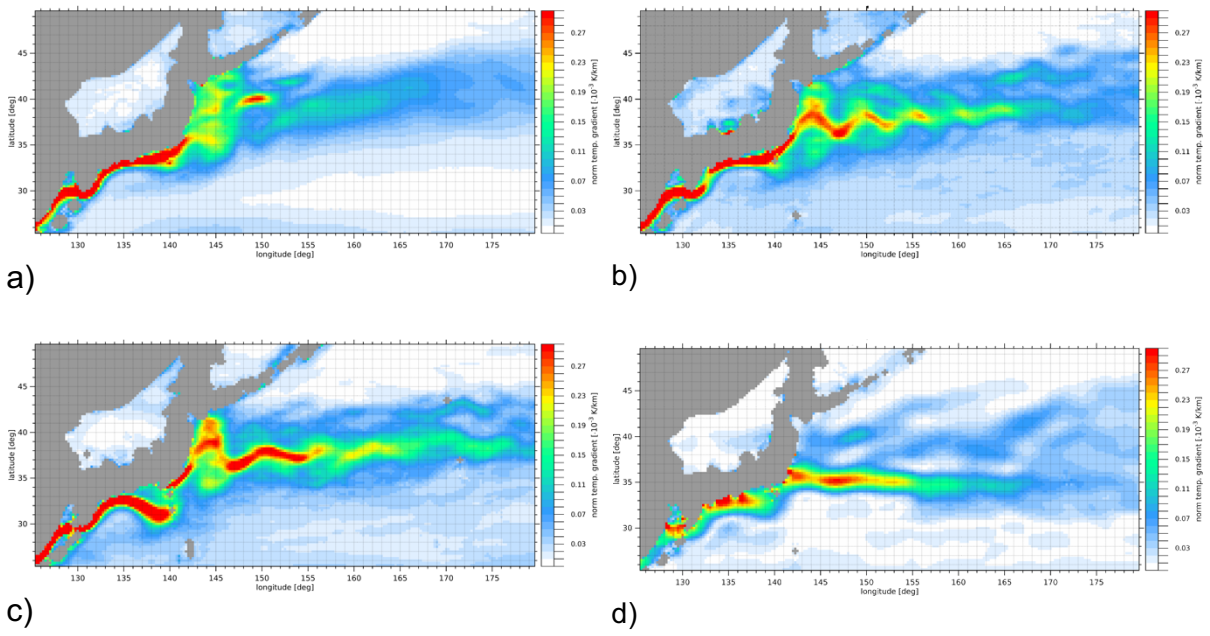

Fig 2. (a)-(c): Modeled horizontal temperature gradient averaged between 200 m - 500 m for setup with coarse (Fig. 1a), intermediate (Fig. 1b) and high (Fig. (1c)) resolution in the area of the KEC region. (d) Observed horizontal temperature gradient averaged between 200 m to 500 m derived from the World Ocean Database 2013 (WOD13) data.

Test the resolution dependence of the Northern Equatorial Current

The Northern Equatorial Current (NEC) corresponds to the southern limb of the subtropical North Pacific gyre, transporting heat and salt, generated by increased insolation and evaporation in the equatorial and subtropical latitudes, westward into the Kuroshio Current (KC). If the NEC in the model is to strong, too much heat and salt could be transported into the KC and be distributed via the subtropical and subpolar gyre system into high latitudes. This in turn could lead to an increase in temperature and salinity in the intermediate layers of the Sea of Okhotsk. To test the resolution dependence of the strength of the NEC we created a additional model configuration (Fig. 3c) which also featured an increased resolution of 10 km to 20 km in the branch of the NEC between −5◦ N and 25◦ N. In this setup we paid particular attention to properly resolve most of the small islands along the equatorial and

subtropical Pacific. Fig. 3a and 3b present the simulated zonal westward directed ocean velocity, averaged between 200 m and 400 m for the model configuration with coarse (Fig. 1c) and high (Fig. 3c) resolution in the area of the NEC, respectively. It is clear, that the resolving of the Pacific equatorial islands and there interaction with the NEC leads to a deceleration as well as meridional spreading of the NEC. As a result, the westward directed heat flux (but also the salt flux) into the KC (Fig. 3c) is decreased by 4 PW to 5 PW in the higher (blue line) resolved equatorial model configuration when compared to the coarse (red line) resolved model configuration. For single events the heat flux in the high resolved equatorial setup can be reduced by up to 10 PW. We also simulated for this model configuration an entire spinup cycle using the COREv2 data as atmospheric forcing. It revealed that the reduction in the heat and salt flux from the NEC into the KC is not sufficient enough to transfer the Sea of Okhotsk in our model configuration into a vertically ventilated state where SOIW is formed on a longer time scale. We tested a plenty of other possibilities to improve the stratification in the Sea of Okhotsk, like the influence of sea ice cover or the influence of the bathymetry and wind forcing on the detachment of the KEC, which we have not presented here. However, non of them led so far to a significant improvement of the stratification in the Sea of Okhotsk on a longer time scale.

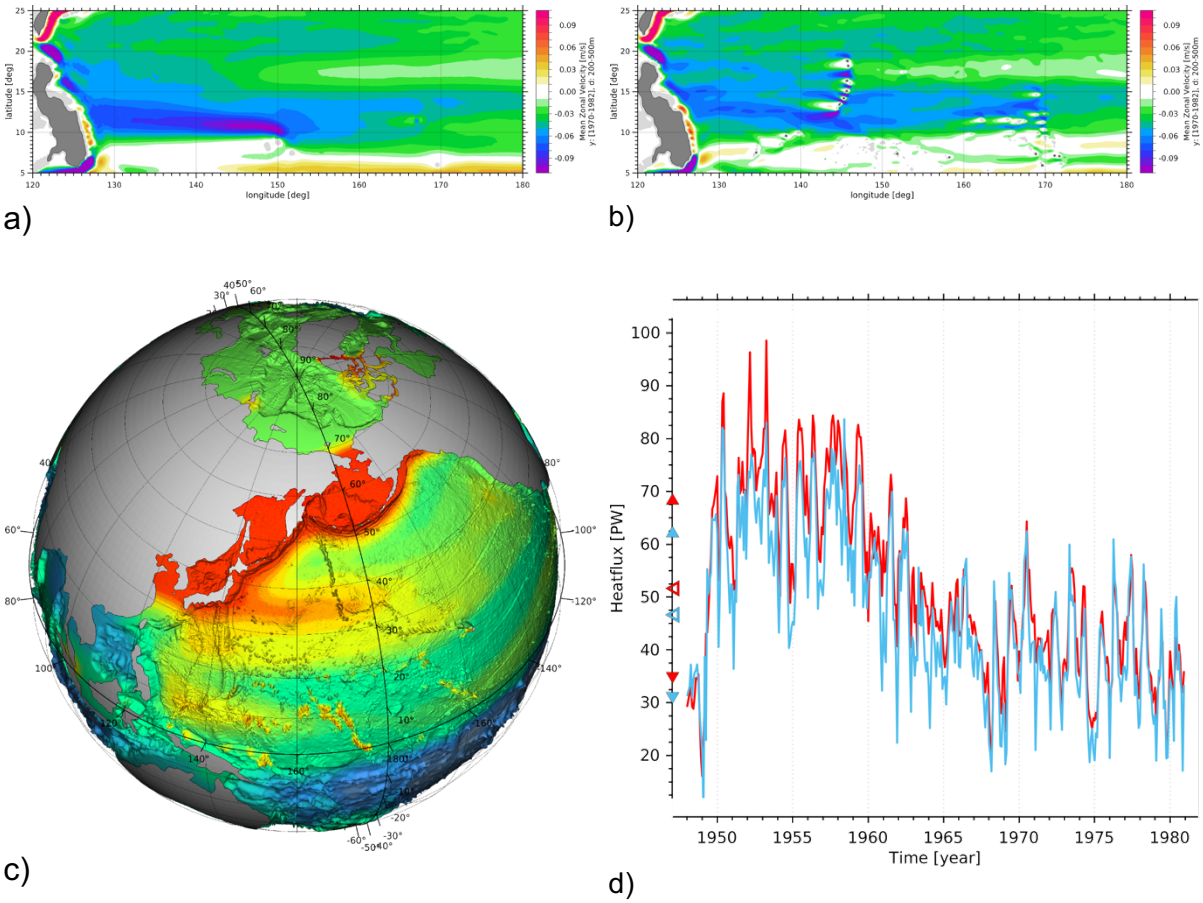

Fig 3. (a)-(b): Modeled mean zonal velocity in the western equatorial and subtropical pacific for a setup with coarse (Fig. 1c) and high resolution (c) in that region. (d): Westward directed heat flux between 0 m and 500 m trough section at lon=[130° W, 130° W], lat = [8° N,14° N] for the setup with coarse (red) and high (blue) resolution.

Outlook

In a next step we want test if a correction of the COREv2 atmospheric surface winds with the monthly climatology of observational derived surface winds fields leads to a southward orientation of the modeled pathway of the KEC. Furthermore, we want to test the influence of different parameterization, like: shortwave penetration, double diffusivity, brine rejection and improved vertical mixing due to non-breaking surface waves on the vertical stratification of the marginal seas of the Northwest Pacific Ocean.

6.13 *hbk00044:* Exploring pathways of Atlantic Water into the Arctic Ocean: high resolution ocean-sea ice and biogeochemical simulations

HLRN Project ID:	hbk00044
Run time:	III/2016 – II/2017
Project Leader:	Prof. Dr. Thomas Jung[1,2]
Project Scientists:	Dr. Claudia Wekerle[2], Dr. Vibe Schourup-Kristensen[2], Dr. Qiang Wang[2], Dr. Sergey Danilov[2], Prof. Torsten Kanzow[1,2]
Affiliation:	[1]University of Bremen, [2]Alfred Wegener Institute for Polar and Marine Research

Overview

The Fram Strait is the deepest and widest gateway that connects the Arctic Ocean with the Nordic Seas and thereby the Atlantic Ocean, thus being the major place where heat and water mass is exchanged between the two oceans. The inflow of Atlantic Water through the Fram Strait into the Arctic Ocean is of high climatic relevance, since it is an important Arctic Ocean heat source and has the potential to melt sea ice. Moreover, changes in the circulation pattern in Fram Strait will have implications for the supply of nutrients to, and phytoplankton growth in, the Arctic Ocean. As the Arctic sea ice extent declines, the light regime in the upper mixed layer and the nutrient supply through horizontal advection and vertical advection and mixing is changing. In order to understand how climate change has, and continues to, impact the biological production and associated uptake of carbon from the atmosphere in the Arctic Ocean, a better understanding of the relative role of the main limiting factors is necessary. A prerequisite for this is an ocean model component providing an adequate representation of the water masses in the Arctic Ocean, their transport, vertical mixing and lateral spreading.

Since around two decades the Alfred Wegener Institute maintains an array of oceanographic moorings in the Fram Strait to monitor the water mass exchange through this gate. Model simulations can complement these measurements and assist in their interpretation.

In this project, we apply a multi-resolution sea ice-ocean model with locally high resolution in the Arctic Ocean and Nordic Seas region. A biogeochemical model coupled to the ocean component allows us to analyze the mean state and variability of the ecosystem. The results obtained so far show that simulated circulation structure and hydrography improve with higher mesh resolution, resulting in good agreement with observations.

Methods

In this project, we apply the multi-resolution Finite-Element-Sea ice-Ocean Model (FESOM) in a global configuration (e.g. Wang et al, 2014). FESOM is coupled to the biogeochemical model REcoM2 (Schourup-Kristensen et al. 2014). In this study we use three different horizontal meshes:

1. **Mesh REF:** Horizontal resolution of 1° throughout most of the world's ocean; resolution is doubled along the coastlines and further improved to 24 km north of 40°N.

2. **Mesh 4.5km:** mesh REF with additional refinement of 4.5 km in the Nordic Seas (north of 60°N) and in the Arctic Ocean. This configuration is considered as "eddy-permitting" in the eastern Nordic Seas and the deep basins of the Arctic Ocean.

3. **Mesh 1km:** mesh 4.5km with additional refinement of 1 km in the wider Fram Strait area (75°N-82.5°N / 20°W-20°E). This mesh is considered as eddy-resolving in the Fram Strait.

All three meshes are used for ocean-sea ice simulations, whereas meshes REF and 4.5km are used for coupled biogeochemical-ocean-sea ice simulations.

Results

1. Eddy-resolving simulations of the ocean and sea-ice dynamics in the Fram Strait

The model performance in the Nordic Seas based on the 4.5 km resolution mesh was assessed by Wekerle et al. (2016). This study showed that the resolution of 4.5 km helps to improve the simulated circulation and hydrography in the Nordic Seas compared to a coarse resolution set-up. However, a temperature bias in the central Fram Strait indicated that higher resolution is indeed necessary for realistically simulating the Atlantic Water circulation and eddy dynamics in the Fram Strait. Thus, an ocean-sea ice simulation applying a resolution of 1 km in the wider Fram Strait area was carried out for the time period 2000-2009 (termed FESOM_1km).

The temperature structure in the Fram Strait is strongly affected by eddies, as shown by a snapshot of the FESOM_1km simulation (Figure 1). Simulated fields of instantaneous relative vorticity reveal a wealth of mesoscale eddies and filaments. Eddies shed from the West Spitsbergen Current are mostly warm-core anticyclonic eddies, whereas cold-core cyclonic eddies are more abundant in the East Greenland Current.

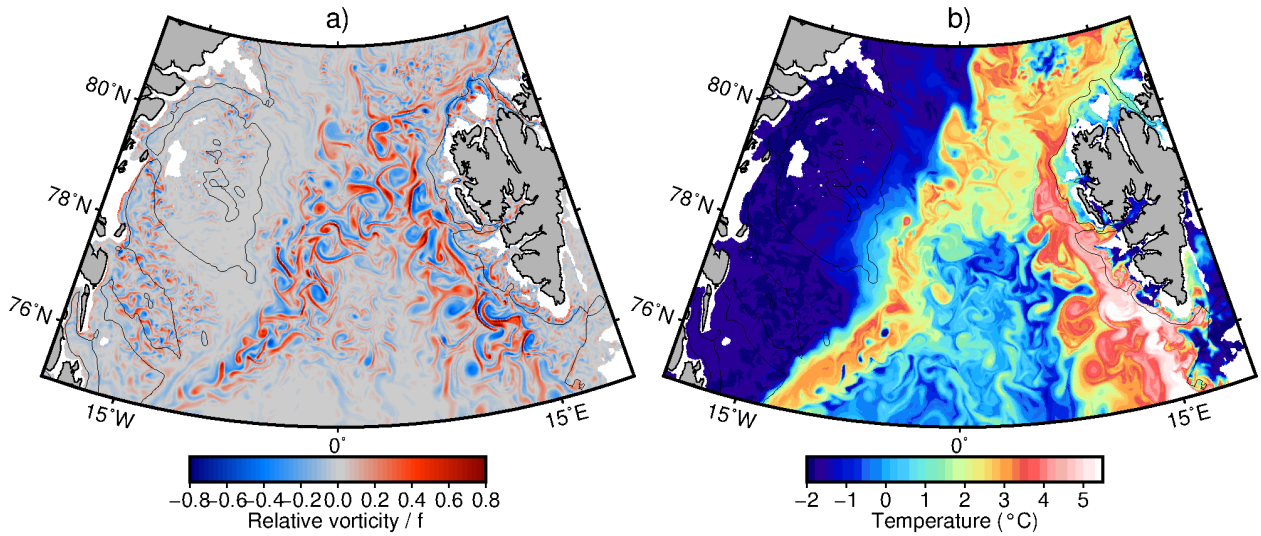

Fig. 1: Snapshots of simulated (a) relative vorticity divided by the Coriolis parameter *f* and (b) temperature in 75 m depth in the Fram Strait region on 31 March 2004 in FESOM_1km. The black contour shows the 250 m isobath.

To assess how realistic the simulated seasonal cycle of eddy kinetic energy (EKE) is, we compare our model results to EKE at 75 m depth derived from current meter measurements of the Fram Strait mooring array (von Appen et al., 2016). The strong eddy activity with

maximum values in winter and lower values in summer simulated by the eddy-resolving model (FESOM_1km) is comparable in magnitude and seasonal cycle to the observations, whereas the eddy-permitting simulation (FESOM_4.5km) underestimates the observed magnitude (Figure 2). Furthermore, when increasing resolution to 1 km a strong cold bias in the central Fram Strait present in the 4.5 km simulation disappears due to changes in simulated mean currents and resolved eddy dynamics (Wekerle et al., 2017, in prep.). In summary, our results suggest that local eddy dynamics are critical in order to realistically simulate the ocean dynamics in Fram Strait.

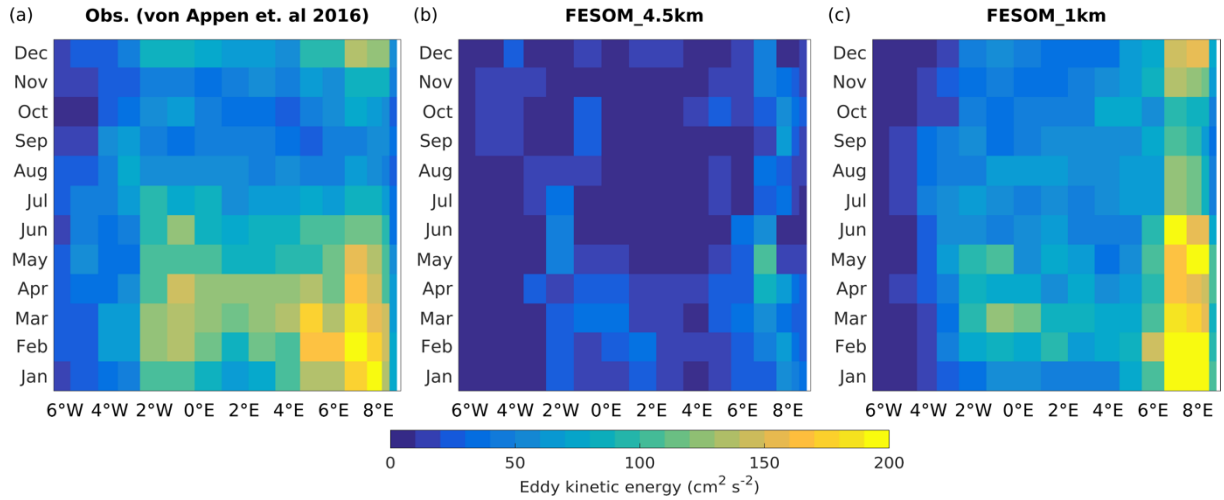

Fig. 2: Seasonal cycle of eddy kinetic energy ($cm^2\ s^{-2}$) at 75 m depth across Fram Strait at 78°50'N from (a) mooring measurements (von Appen et al., 2016) and simulations (b) FESOM_4.5km and (c) FESOM_1km for the time period 2001-2009.

2. Biogeochemical simulations

When we compared the high resolution (4.5 km) and reference resolution (24 km) regarding the biogeochemistry, we noticed large differences in the magnitude and spatial distribution of Arctic biological productivity. The productivity was substantially lower in the 4.5 km run in most of the Arctic Ocean, and especially under the ice. After analyzing the runs, we realized that the difference was brought on by the stronger gradients in the 4.5 km run, which held back spatial mixing of the phytoplankton seeding population, which is necessary for a bloom to start.

We tested new parameterizations for the biogeochemistry using the 24 km mesh, and we have now performed a new 4.5 km run from 1980 to 2014, in which the productivity is improved, being much more spatially variable than before. It does, for instance capture ice edge blooms (Figure 3).

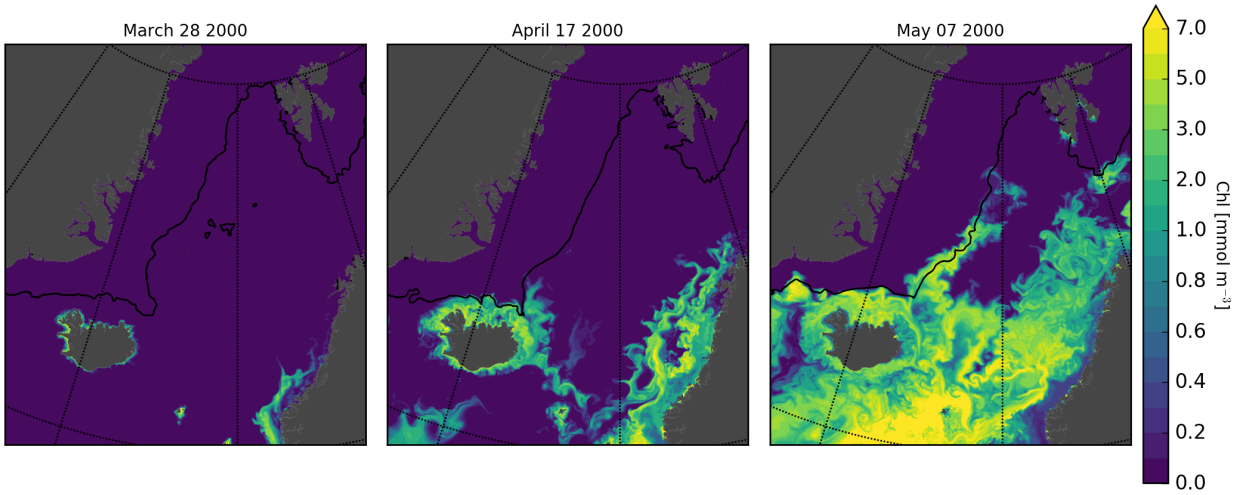

Fig. 3: Surface chlorophyll in the Nordic Seas following the development on three days in the spring. 4.5 km resolution using improved settings for biogeochemistry.

The JRA-55 atmospheric forcing has made it possible for us to run up to the year 2015 (currently we have run until 2014). This makes it possible to look into the current changes of biological productivity in the Arctic Ocean. First results show that productivity has indeed increased since the year 2000, with production peaking in 2012, the year with a record low summer sea ice extent. Conversely, export production is constant, due to a change towards small phytoplankton (Figure 4).

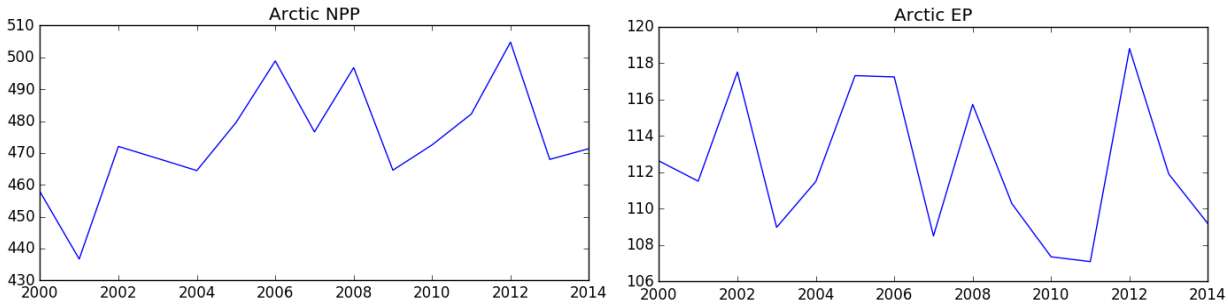

Fig. 4: Yearly development of (left) total net primary production and (right) export production in the Arctic Ocean.

Outlook

Concerning ocean-sea ice simulations, we plan to repeat the 1 km simulations with the atmospheric forcing JRA-55 (which is continuously updated), allowing us to investigate recent changes in ocean and sea ice conditions in the Fram Strait area.

As the Arctic sea ice becomes dominated by first year ice, the under ice productivity is thought to become more important. For models to be able to capture this, a better parameterization of the light penetration through ice is necessary. In the AWI sea ice group, a new light parameterization has been developed using 1D models. The next step would be to test this in FESOM-REcoM2.

Resent observations show that sea ice leads may contribute significantly to the Arctic productivity. The high resolution in FESOM makes it possible to create sea-ice leads in the run, giving us the unique possibility to explore their impact on a larger scale with FESOM.

As the Arctic is changing, the carbon uptake by the ocean is most likely also changing. We have the full carbon cycle in REcoM2, and results from this looks promising in the current run. But to look further into the carbon cycle, a longer spin-up would be needed.

Publications

- Wekerle, C., Wang, Q., Danilov, S., Schourup-Kristensen, V., von Appen, W. J., and Jung, T. (2016), "*Atlantic water in the Nordic Seas: Locally eddy-permitting ocean simulation in a global setup",* Journal of Geophysical Research-Oceans, doi:10.1002/2016JC012121.

Publications (in preparation)

- Schourup-Kristensen, V., Wekerle, C., Wolf-Gladrow, D. A., and C. Völker (2017), *„Arctic biogeochemistry in the Finitel Element Sea-ice Ocean Model",* in prep. for JGR.
- Wekerle, C., Wang, Q., von Appen, W. J., Danilov, S., Schourup-Kristensen, V., and Jung, T. (2017), "*Eddy-resolving simulation of the Atlantic Water circulation in Fram Strait with focus on the seasonal cycle"*, in prep. for JGR.

Presentations

- Schourup-Kristensen, V., Wekerle, C., Wolf-Gladrow, D. A., and C. Völker: *„A high resolution Arctic Pan Arctic biogeochemical module",* Talk, Biogeochemical processes in the Lena Delta and Laptev Sea regions workshop, Potsdam, 25-26 June, 2016.
- Schourup-Kristensen, V., Wekerle, C., Wolf-Gladrow, D. A., and C. Völker: *"Effect of resolution on Arctic net primary productivity"*, Poster, Forum for Arctic modeling & observational synthesis, Woods Hole, USA, 1-4 November 2016.
- Schourup-Kristensen, V., Wekerle, C., Wolf-Gladrow, D. A., and C. Völker: *"The FRAM biogeochemical module"*, Talk, East Siberian Shelf: Observations, data analysis and modelling efforts, workshop, Potsdam, 7-9 December 2016
- Schourup-Kristensen, V., Wekerle, C., Wolf-Gladrow, D. A., and C. Völker: *"Arctic primary productivity in a high resolution biogeochemical model",* Talk, Danish Ocean Sciences meeting, Copenhagen, Denmark, 25-27 January 2017.
- Wekerle, C., Wang, Q., Danilov, S., von Appen, W. J., Schourup-Kristensen, V., and Jung, T.: "*Eddy-resolving simulation of the Atlantic Water recirculation in the Fram Strait",* Talk, DRAKKAR 2017 Annual Workshop, 16-18 January 2017.
- Wekerle, C., Wang, Q., Danilov, S., Schourup-Kristensen, V., von Appen, W. J., and Jung, T.: "*Recirculation of Atlantic Water in Fram Strait: A high resolution modeling study",* Poster, Forum for Arctic Modeling & Observational Synthesis, Woods Hole, USA, 1-4 November 2016.

References

- Schourup-Kristensen, V., D. Sidorenko, D. A. Wolf-Gladrow, and C. Völker (2014), *„A skill assessment of the biogeochemical model REcoM2 coupled to the Finite Element Sea-Ice Ocean Model (FESOM 1.3)"*, Geosci. Model Dev., 7 (6), 2769-2802.
- von Appen, W.J., Schauer, U., Hattermann, T., and Beszczynska-Möller, A. (2016) "*Seasonal Cycle of Mesoscale Instability of the West Spitsbergen Current",* J. Phys. Oceanogr. 46, 1231-1254, doi: 10.1175/JPO-D-15-0184.1.
- Wang, Q., S. Danilov, D. Sidorenko, R. Timmermann, C. Wekerle, X. Wang, T. Jung, and J. Schröter (2014), "*The Finite Element Sea Ice-Ocean Model (FESOM) v.1.4: formulation of an ocean general circulation model"*, Geosci. Model Dev., 7, 663-693.

6.14 *hbk00055 (hbk0046):* Investigating the biogeochemistry of the high latitudes during the period of rapid change: modeling and satellite retrievals

HLRNProject ID:	hbk0055 (hbk0046)
Run time:	III/2016 – III/2017 (IV/2015 – II/2016)
Project Leader:	Prof. Dr. A. Bracher[1]
ProjectScientists:	S. Losa, M. Losch
Affiliation:	Alfred-Wegener-Institut Helmholtz Centre for Polar and Marine Research, Bremerhaven [1]also professor at University of Bremen

Overview

The study relates to the project "Artic Amplification: Climate Relevant **A**tmospheric and Surfa**C**e Processes, and Feedback Mechanisms **(AC)^3**" within the establishment of Transregional Collaborative Research Centre TR 172. One of the subtasks of the project is to improve our understanding of possible interactions between the open water, sea ice, snow, ocean biogeochemistry and ecosystem and chemical composition of the Atmospheric Boundary Layer under the recently observed sea ice decline in the Arctic. The analysis of the changes in phytoplankton functional types (PFT) and Coloured Dissolved Organic Matter (CDOM) absorption observed over the last two decades is based on long-term time series of satellite retrievals and has to be supported by a modelling study. The CDOM and phytoplankton dynamics as well as phytoplankton diversity in response to Arctic Amplification is simulated with the biogeochemical model Darwin (Follows et al., 2007, Dutkiewicz et al., 2015) coupled to the Massachusetts Institute of Technology General Circulation Model (MITgcm, MITgcm Group, 2012). This combined model and satellite-derived information will be used for investigating existing relationships and feedbacks between the Arctic climate change, the ocean biogeochemistry and atmospheric oxidative capacity. Within the HLRN project we continue supporting the DFG research "Antarctic phytoplankton in response to environmental changes studied by a synergetic approach using multi- and hyper-spectral satellite data (PhySen)" within the framework of the DFG-Priority Program 1158 "Antarctic Research" (former HLRN project hbk00046).

Results

The satellite data product. A version of satellite data product on phytoplankton composition (SynSenPFT product, Figure 2) was obtained by combining synergistically empirical PFT retrivals based on multispectral satellite information (OC-PFT, Hirata et al., 2011, Soppa 2014) and analytical hyper-spectral based bio-optical retrievals (PhytoDOAS, Bracher et al. 2009, Sadeghi et al. 2012). The SynSenPFT product is provided on a ~4 km resolution grid for the period of August 2002 – March 2012 on a daily basis. Figure 1 depicts monthly mean SynSenPFT chlorophyll "a" concentration (Chla) of diatoms, coccolithophores and cyanobacterias for the Arctic Ocean in June 2010.

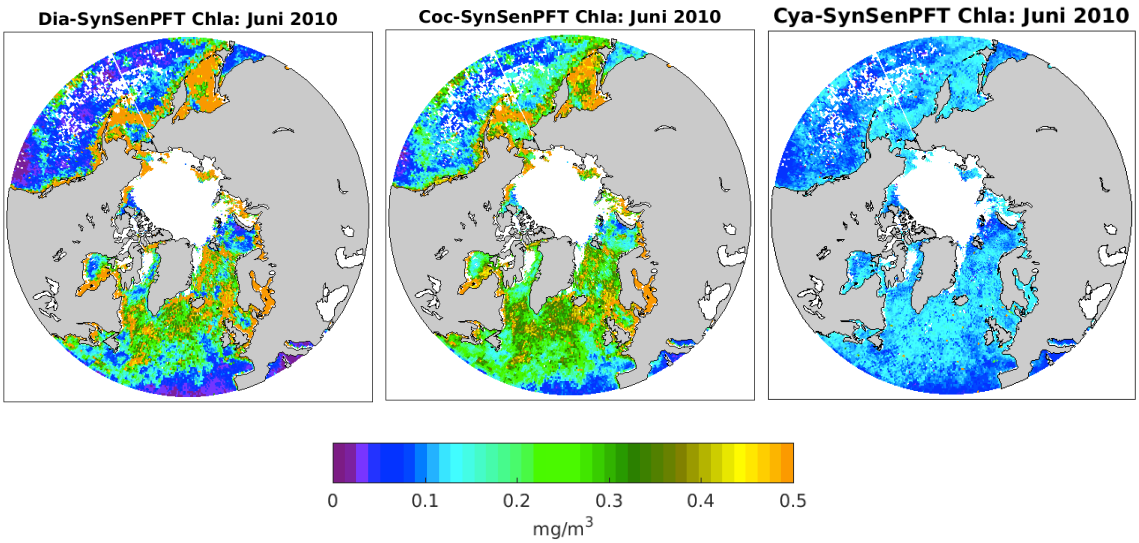

Fig. 1: June 2010 monthly mean Chlorophyll "a" concentration of diatoms, coccolithophores and cyanobacterias obtained when synergistically combining the PhytoDOAS hyper-spectral PFT retrievals (Bracher et al. 2009, Sadeghi et al. 2012a) and multi-spectral based OC-PFT (Soppa 2014) in the Arctic Ocean.

PFTs model simulation. The coupled sea-ice - ocean circulation - biogeochemical model with biogeochemical parameters as in the study by Dutkiewicz et al. (2015) have been integrated over several years and evaluated for the period of 2001-2006. The model configuration based on a cubed-sphere grid (Menemenlis et al. 2008) with mean horizontal spacing of ~18 km and 50 vertical levels with the resolution ranging from 10 m near the surface to ~450 m in the deep ocean. It is worth mentioning that the number of model PFTs has been reduced to 6 when comparing against the complexity used in the study by Dutkiewicz et al. (2015). In particular, we consider analogues of diatoms, other micro-phytoplankton, prochlorococcus, other picophytoplankton (including *Synechococcus*), nitrogen fixing *Trichodesmium* and cocolithophores.

First sensitivity tests showed that setting some of physiological parameters – pico-phytoplankton growth rate, microphytoplankton mortality, coccolithophorese grazing (palatibilty factor), – impacts spatial distribution and characteristics of the bloom of micro-, nano- and pico-plankton. The sensitivity of the phytoplankton phenology to the parameters even more pronounced in the Southern Ocean (SO, not shown). The conducted simulations have revealed a problem with the model dynamics of the coccolithophores (figure 2 and 3, blue and black curves), one of the observed phytoplankton types in dominance. More plausible model simulations of the coccolithophores phenology (sigure 2, red curve) and distribution required some changes in parameterisation of the coccolithophores physiology. Figure 3 illustrates spatial distribution of the model monthly mean PFT Chla in the Arctic Ocean for June 2005 when considering coccolithophores as nanoplankton (in contrast with default Darwin setting and in accordance to observations) with slower growth and lower grazing pressure.

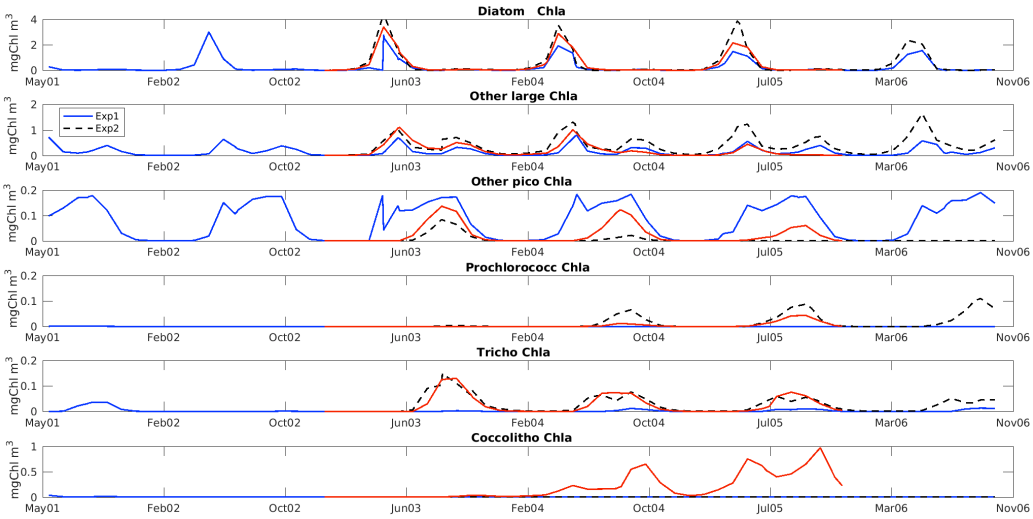

Fig. 2: Temporal evolution of the model various PFT Chla (mg/m3) for the ARCT biogeochemical province (Longhurst, 1998) for experiments with different physiological parameter sets (red: coccolithophore is treated as nanoplankton with slower growth and lower grazing pressure).

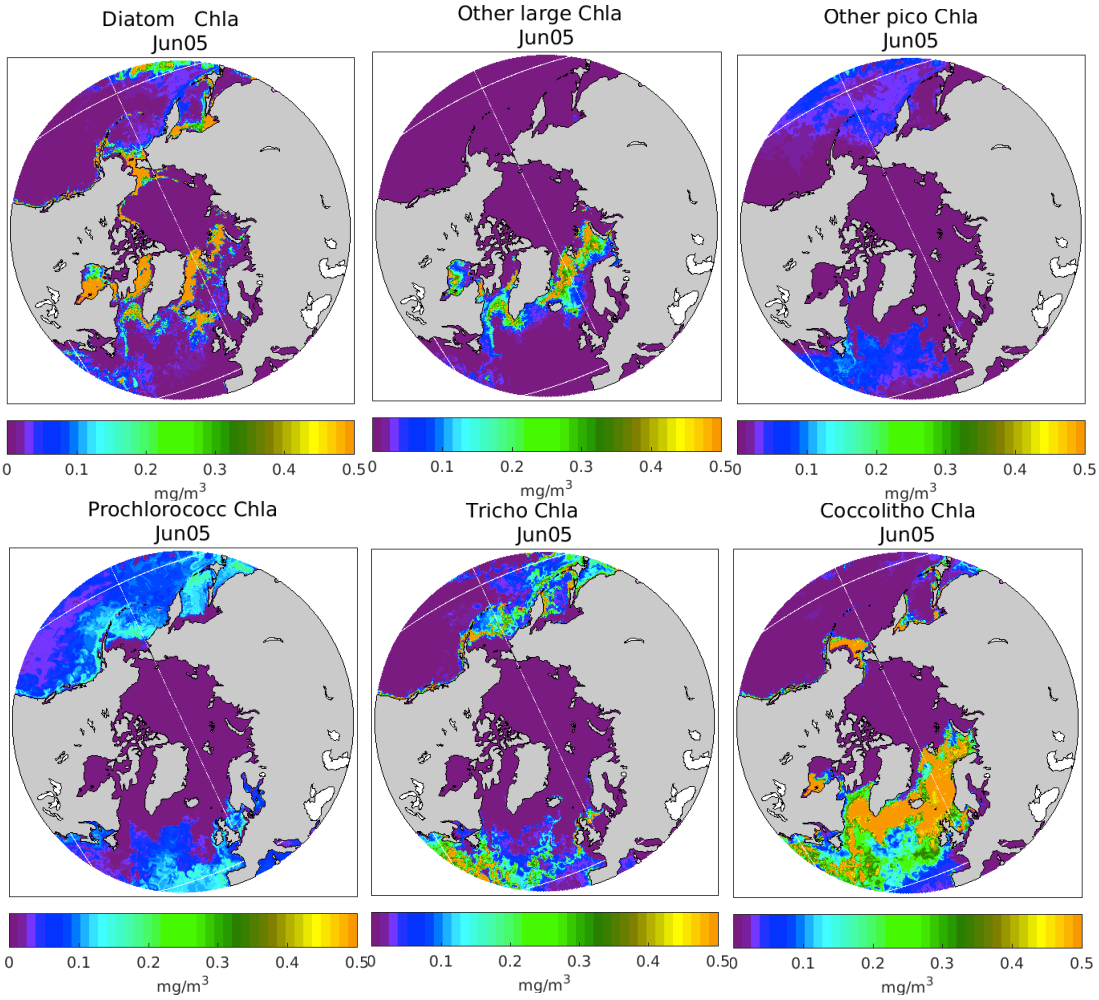

Fig. 3: Spatial distribution of the model monthly mean PFTs Chla for June2005.

Outlook

The calibration and evaluation of the coupled MITgcm-Darwin model will be continued in order to set up plausible model configurations for obtaining long-term Chla data of various phytoplankton groups and CDOM in the Arctic Ocean and in the Southern Ocean (the role of CDOM in SO might be not so crucial, however). A version of the SynSenPFT product updated by using the ocean colour retrievals adapted to high latitude peculiarities (improved corrections for low sun, clouds, ice, photo-adaptation, CDOM) can be also acpected. The satellite retrievals and model results will be validated with *in situ* high precision liquid chromatography (HPLC) measurements.

Presentations

8. Losa, S. N., Oelker, J., Soppa, M. A., Dinter, T., Losch, M., Dutkiewicz, S., Richter, A., Burrows, J. P. and Bracher, Investigating Antarctic PFTs based on satellite observation and modeling, Ocean Optics XXIII, Victoria, BC, Canada, 23–28 October 2016.
9. Oelker, J., Losa, S. N., Soppa, M. A., Losch, M., Dinter, T., Richter, A., Brache, A. and Burrows, J. P., Antarctic phytoplankton in response to environmental changes studied by a synergistic approach using multi- and hyper-spectra satellite data (PhySyn), Koordinations-Workshop SPP 1158, Rostock, 14–16 September 2016.

References

1. Bracher, A., Vountas, M., Dinter, T., Burrows, J.P., Röttgers, R., Peeken, I. (2009) Quantitative observation of cyanobacteria and diatoms from space using PhytoDOAS on SCIAMACHY data. Biogeosciences 6: 751-764.
2. Dutkiewicz, S., Hickman, A. E., Jahn, O., Gregg, W. W., C. B. Mouw, C. B., and M. J. Follows (2015) Capturing optically important constituents and properties in a marine biogeochemical and ecosystem model Biogeosciences 12, 4447-4481.
3. Follows, M. J., Dutkiewicz, S., Grant, S., and Chisholm, S. W. (2007) Emergent biogeography of microbial communities in a model Ocean, Science, 315, 1843–1846.
4. Longhurst. A. (1998) Ecological Geography of the Sea, Academic press.
5. Menemenlis, D., Campin, J.-M., Heimbach, P., Hill, C., Lee, T., Nguyen, A., Schodlock, M., and H. Zhang (2008) High resolution global ocean and sea ice data synthesis, Mercator Ocean Quartely Newsletter, 31, 13–21.
6. MITgcm Group (2012), MITgcm Manual, Online documentation, MIT/EAPS, Cambridge, MA 02139, USA.
7. Sadeghi, A., Dinter, T., Vountas, M., Taylor, B. B., Soppa, M. A., Peeken, I., and A. Bracher (2012) Improvements to the PhytoDOAS method for identification of coccolithophores using hyperspectral satellite data. Ocean Sciences 8:1055-1070.
8. Soppa, M. A., Hirata, T., Silva, B., Dinter, T., Peeken, I., Wiegmann, S., Bracher, A. (2014) Global Retrieval of Diatom Abundance Based on Phytoplankton Pigments and Satellite Data. Remote Sensing, 6(10), 10089-10106.

6.15 *hbk00051: Holozäne Klimavariabilität im Nordatlantik: Zustandswechsel und quasi-dekadische Oszillation in einem Klimamodell*

HLRN-Projektkennung:	hbk00051
Laufzeit:	I/2016 – IV/2016
Projektleiter:	Prof. Dr. Michael Schulz
Projektbearbeiter:	Dr. Matthias Prange, Andrea Klus
Institut / Einrichtung:	Fachbereich Geowissenschaften. MARUM - Zentrum für Marine Umweltwissenschaften, Universität Bremen

Überblick

- Paläozeanographische Aufzeichnungen zeigen erhebliche holozäne Klimaschwankungen im Bereich des Nordatlantiks auf Zeitskalen von Jahrhunderten bis Jahrtausenden.
- Mit Hilfe eines komplexen Klimamodells wurde untersucht, inwieweit die Zufuhr von Süßwasser Erdorbitalparameter oder ein Erhöhen des atmosphärischen CO_2-Gehalts Auswirkungen auf die Ozeanzirkulation des Nordatlantiks haben, insbesondere die Stärke der atlantischen Umwälzzikulation (AMOC).
- Die numerischen Experimente sollen Aufschluss über den Einfluss des klimatischen Hintergrundzustandes auf Wassermassen sowie die Existenz, das Verhalten und die Zeitskalen von nordatlantischen Zustandswechseln geben.

Wissenschaftlicher Hintergrund

Zahlreiche Studien haben einen Zusammenhang zwischen Klimavariabilität auf Zeitskalen von Jahrhunderten bis Jahrtausenden und Veränderungen in der Stärke der AMOC und dem einhergehenden Wärmetransport postuliert (z.B. O'Brien et al., 1995; Bond et al., 1997, 2001; Bianchi und McCave, 1999; Schulz und Paul, 2002; Hall et al., 2004). Nicht nur aus paläoklimatischer Sicht ist es sinnvoll die Auslöser und Dynamik dieser niederfrequenten Variabilität nachzuvollziehen, sondern auch, um eventuelle Zusammenhänge mit anthropogenem Klimawandel zu erfassen (vgl. Knutti and Stocker, 2002). Klimaschwankungen auf Zeitskalen von Jahrhunderten bis Jahrtausenden, die mit der Variabilität der AMOC-Stärke einhergehen, treten im gekoppelten Klimamodell mittlerer Komplexität ECBilt-CLIO auf (Schulz et al. 2007). Sowohl Rekonstruktionen der Dichteschichtung der Labradorsee sowie der Winterkonvektion während des Holozäns (Hillaire-Marel et al., 2001) als auch Modellergebnisse weisen darauf hin, dass den klimatischen Oszillationen eine Bistabilität in der Labradorsee zugrunde liegt. Zwar berichten Yoshimori et al. (2009) von zwei möglichen AMOC-Zuständen in vorindustriellen Simulationen mit dem Klimamodell CCSM3 (Community Climate System Model Version 3; Collins et al., 2006), jedoch wurde die niederfrequente Variabilität systematisch auf ihre Stabilitäts- und Bifurkationseigenschaften hin untersucht. In einer 9760 Jahre langen Simulation des holozänen Klimas mit dem CCSM3 haben wir vor kurzem einen abrupten und dauerhaften Zustandsübergang von starker zu schwacher AMOC gefunden. Die Existenz der zwei AMOC-Zustände zeigt Potenzial für störungsbedingte Übergänge und damit niederfrequente Variabilität ähnlich wie in ECBilt-CLIO. Die Ursache dieser Variabilität ist bisher noch unklar. Mit Hilfe dieses Projekts wollen wir Randbedingungen identifzieren, die

niederfrequente AMOC-Schwankungen begünstigen, sowie Frühwarnsignale für nordatlantische Klimaübergänge ausfindig machen.

Methode

Das voll gekoppelte Klimamodell CCSM3 besteht aus dem spektralen Atmosphärenzirkulationsmodell CAM3, dem Landmodell CLM3, dem Finite-Differenzen-Ozeanmodell POP und dem dynamischen Meereismodell CSIM5 (elastisch-viskos-plastische Meereis- Rheologie). Das Modell wurde mit einer horizontalen Auflösung von 3,75° (T31) für das Atmosphären-/Landmodellgitter betrieben, während das Ozean-/Meereisgitter eine räumlich variable Gitterweite von ca. 3° in zonaler und bis zu 0,9° in meridionaler Richtung besitzt. Die vertikale Darstellung des Atmosphärenmodells umfasst 26 Schichten, der Ozean wird mit 25 Niveaus in der Vertikalen diskretisiert.

Änderungen in den Randbedingungen umfassten sowohl die Süßwasserzufuhr im Bereich des Nordwestatlantiks als auch die Treibhausgaskonzentration. Bei der Durchführung der Sensitivitätsexperimente wurde Süßwasser in einer Menge von 30 bzw. 120 mSv (1 Sv = 10^6 m^3/s) im Nordwestatlantik zugeführt. Orbitalparameter und Treibhausgaskonzentration wurden konstant auf vorindustriellen Werten gehalten. Bei den Sensitivitätsexperimenten mit verschiedenen Treibhausgaskonzentrationen wurde die Auswirkung der Treibhausgas-konzentration von glazialen bis heutigen Werten getestet. Hierbei fand keine zusätzliche Zufuhr von Süßwasser statt und die Orbitalparameter wurden während des jeweiligen Modelllaufes konstant gehalten Als Anfangsbedingung wurde jeweils der Output eines vorindustriellen Kontrolllaufs verwendet.

Erste Ergebnisse

Es wurden zwei Süßwasserexperimente mit 30 bzw. 120 mSv durchgeführt. Das Süßwasser wurde südlich von Grönland eingespeist. Während die Simulation mit einer Zufuhr von 30 mSv keinen Zustandswechsel aufweist, ist in der 120 mSv-Simulation ein Wechsel zu erkennen. Die AMOC schwächt von anfänglichen ca. 16 Sv auf 6,3 Sv ab. Während des schwachen Zustandes unterliegt der AMOC einer Oszillation mit einer Periode von etwa 11,8 Jahren.

Abbildung 1 zeigt die AMOC-Intensität während der CO_2-Experimente, deren orbitale Bedingungen 9000 Jahre vor heute (9 ka BP) sowie heutiger Zeit entsprechen. Hierbei wurden CO_2-Werte von 210 und 240 ppm verwendet. In Abbildung 2 ist die AMOC-Stärke für orbitale Bedingungen von 130 ka BP mit CO_2-Werten von 210, 240, 270, 300 und 330 ppm dargestellt. Bis auf den Modelllauf mit 240 ppm CO_2 und 9 ka BP Orbitalbedingungen wechselt der AMOC aus dem starken Zustand von 12,7-14,3 Sv immer in einen schwächeren Zustand von 9,0 -10,2 Sv. Wenn ein Zustandswechsel in den vorliegenden Simulationen stattfindet, dauert es bis zum Zustandswechsel 80 bis ca. 500 Modelljahren. Zudem weist der schwache AMOC-Zustand ebenso wie während der 120 mSv-Simulation eine Oszillation mit einer Periode von 12,5 bis zu 14,4 Jahren auf. Ein erneuter Übergang in den starken Zustand findet nicht statt.

Zurzeit ist für den Zeitpunkt des Zustandswechsels noch kein eindeutiges System erkennbar. Eine ausführliche Analyse wird noch durchgeführt, um die Interaktion zwischen Süßwasser bzw. CO_2 und AMOC, aber auch die mit Temperatur, Salzgehalt, Eisbedeckung und anderen Klimakomponenten besser zu verstehen. Schon jetzt zeichnet sich ab, dass CO_2-Konzentration und Süßwasserzufuhr einen starken Einfluss nicht nur auf die Intensität der Atlantischen Umwälzzirkulation (AMOC), sondern auf das gesamte Klimasystem des Nordatlantiks und des Nordmeers haben.

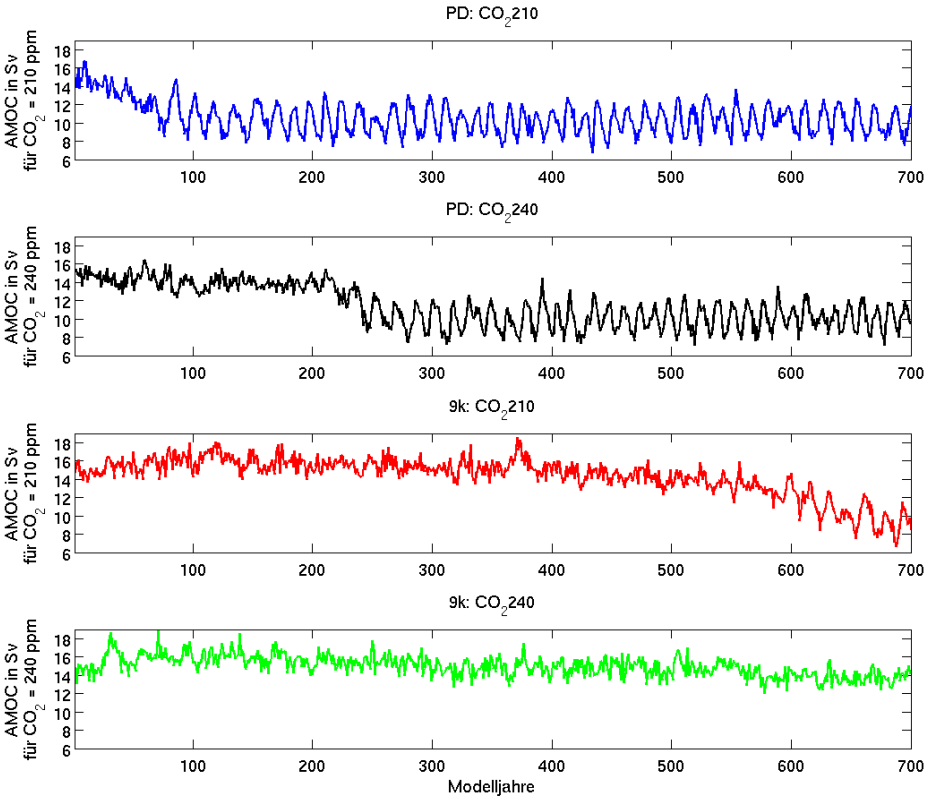

Abb. 1: AMOC-Stärke während der 9 ka BP und heutigen (PD: "present day") Simulationen.

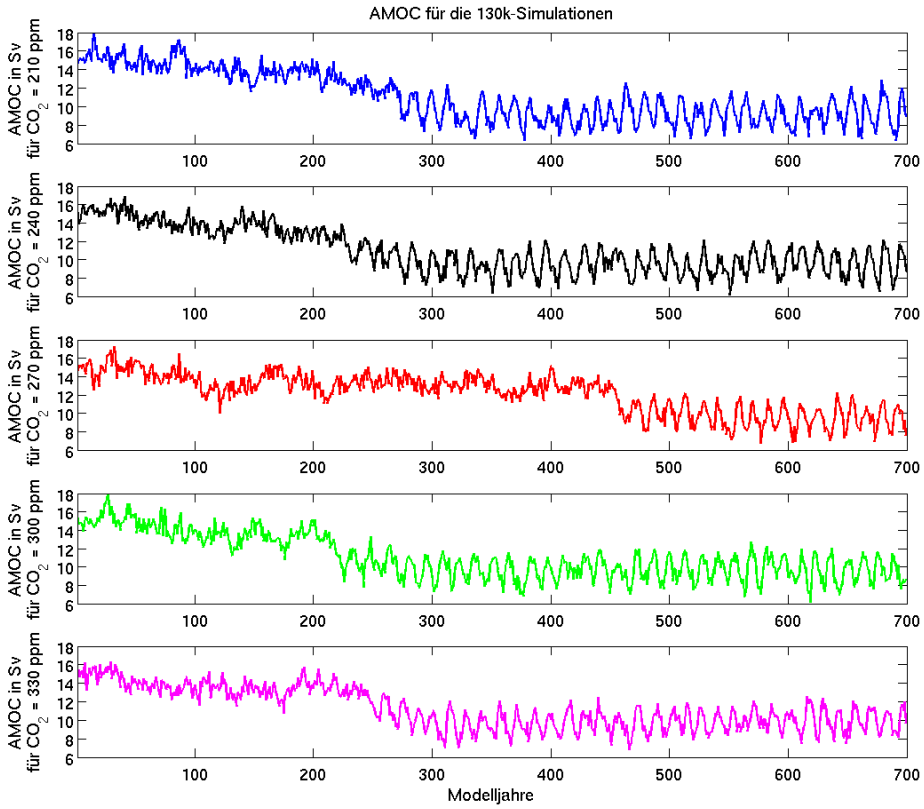

Abb. 2 AMOC-Stärke während der 130 ka BP Simulationen.

Referenzliste (Projektleiter/-bearbeiter *kursiv* gedruckt)

Bianchi und McCave, 1999: Holocene periodicity in North Atlantic climate and deepocean flow south of Iceland. Nature, 397, 515-517, doi:10.1038/17362

Bond et al., 1997: A Pervasive Millennial-Scale Cycle in North Atlantic Holocene and Glacial Climates. Science, 1257-1266, doi:10.1126/science.278.5341.1257.

Bond et al., 2001: Persistent Solar Inuence on North Atlantic Climate During the Holocene. Science, 2130-2136, doi:10.1126/scince.1065680

Brown, N., and Galbraith, E.D., 2015, Hosed vs. unhosed: global response to interruptions of the Atlantic Meridional Overturning, with and without freshwater forcing. Climate of the Past, 11, 4669-4700, doi:10.5194/cpd-11-4669-2015.

Collins, W. D., and Coauthors, 2006: The Community Climate System Model version (CCSM3). J. Climate, 19, 2122-2143.

Hall et al., 2004: Centennial to millennial scale Holocene climate-deep water linkage in the North Atlantic. Quatern. Sci. Rev., 23, 1529-1536.

Hillaire-Marcel et al., 2001: Changes of Potential Density Gradients in the Northwestern North Atlantic during the Last Climatic Cycle Based on a Multiproxy Approach. In: The Seidov, D. et al. (eds.), The oceans and rapid climate changes: 8 Past, present and future. Geophysical Monograph Series, 126, 63-100, GEOTOP publication n_ 2001-0007.pdf

Knutti und Stocker, 2002: Limited predictability of future thermohaline circulation close to an instability threshold, J. Clim., 15, 179-186.

O'Brien et al., 1995: Complexity of Holocene climate as reconstructed from a Greenland ice core. Science, 270, 1962-1964, doi:10.1126/science.270.5244.1962.

Schulz und Paul, 2002: Holocene climate variability on centennial-to-millennial time scales: 1. Climate Records from the North Atlantic Realm. In: Wefer, G., Berger,

Schulz et al., 2007: Low-frequency oscillations of the Atlantic Ocean meridional over- turning circulation in a coupled climate model. Climate of the Past, 3, 97-107

Yoshimori et al., 2009: Simulated decadal oscillations of the Atlantic meridional overturning circulation in a cold climate state. Climate Dynamics, 2010, 34, 101-121, doi:10.1007/s00382-009-0540-9.

6.16 *hbk0056:* Eurasische Klimavariabilität im letzten Jahrtausend

HLRN-Projektkennung:	hbk00056
Laufzeit:	III/2016 – II/2017
Projektleiter:	Prof. Dr. Michael Schulz
Projektbearbeiter:	Dr. Matthias Prange, Sri Nandini
Institut / Einrichtung:	Fachbereich Geowissenschaften, MARUM - Zentrum für Marine Umweltwissenschaften, Universität Bremen

Überblick

- Mit Hilfe einer hochaufgelösten Version des Community Earth System Model (Version 1.2) sollen vergangene und zukünftige Klimaschwankungen in Eurasien mit besonderem Blick auf die pontokaspische Region simuliert und analysiert werden.
- Die Fähigkeit des Klimamodells, heutige Klimavariabilität in der Region zu simulieren, wird anhand von Beobachtungs- und Reanalysedaten ausgewertet.
- Ergebnisse aus dem Klimamodell werden verwendet, um mit Hilfe hydrologischer Modellierung vergangene und zukünftige Seespiegelschwankungen des Kaspischen Meeres zu untersuchen.

Hintergrund

Im Rahmen des EU-finanzierten Marie Sklodowska-Curie Innovative Training Network (ITN) PRIDE (Drivers of Pontocaspian Biodiversity Rise and Demise) sollen vergangene Umweltveränderungen in der pontokaspischen Region (Einzugsgebiete des Schwarzen Meeres mit dem Asowschen Meer, des Kaspischen Meeres und des Aralsees sowie Bereiche des angrenzenden West- und Zentralasien) und deren Einfluss auf die regionale Biodiversität untersucht werden (http://www.pontocaspian.eu). Ein wesentlicher Schwerpunkt liegt dabei auf der jüngeren Vergangenheit, d.h. das späte Holozän mit besonderem Blick auf das letzte Jahrtausend. Ein Teilbereich des internationalen Projekts befasst sich mit der Entwicklung des Klimas und der pontokaspischen Seewasserstände (insb. Kaspisches Meer). Mit Hilfe von Klima- und hydrologischer Modellierung sollen vergangene Umweltveränderungen einerseits “rekonstruiert”, andererseits aber auch physikalisch verstanden werden. Zudem sollen Prognosen für zukünftige hydroklimatische Veränderungen in der Region erstellt werden, um abzuschätzen, inwieweit mit zukünftigen, klimabedingten Seespiegelschwankungen zu rechnen ist.

Methode

Als Teil des PRIDE-Konsortiums führen wir Klimasimulationen des letzten Jahrtausends mit dem voll gekoppelten Community Earth System Model version 1.2 (CESM1.2) durch. Die räumliche Auflösung der atmosphärischen Modellkomponente (CAM5) beträgt 1°, um regionale Prozesse zufriedenstellend darstellen zu können. Das Ozean-/Meereisgitter besitzt eine räumlich variable Gitterweite von ca. 1° in zonaler und bis zu 0,3° in meridionaler Richtung. Die vertikale Darstellung des Atmosphärenmodells umfasst 30 Schichten, der Ozean wird mit 60 Niveaus in der Vertikalen diskretisiert. Um den möglichen Einfluss von Änderungen der solaren Einstrahlung auf die Klimavariabilität in der pontokaspischen Region genauer zu untersuchen, führen wir eine Serie von Jahrtausend-Simulationen durch, in der

sowohl die Unsicherheit im solaren Antrieb als auch die Rolle von interner Klimavariabilität berücksichtigt werden. Die Stärke der solaren Strahlungsschwankungen ist einer der großen Unsicherheitsfaktoren im Klimaantrieb des letzten Jahrtausends. Neben dem solaren Antrieb werden zeitliche Änderungen in der vulkanischen Aktivität (stratosphärischer Sulfataerosol-Gehalt), den Erdorbitalparametern, den Treibhausgasen sowie der Landbedeckung berücksichtigt. Historische Simulationen und deren Vergleich mit Beobachtungs- und Reanalysedaten dienen der Validierung des Modells in der pontokaspischen Region, während Simulationen für verschiedene RCP-Szenarien (RCP: „Representative Concentration Pathways“) für das 21. Jahrhundert Hinweise auf mögliche zukünftige Veränderungen liefern.

Erste Ergebnisse

Die Fähigkeit des Klimamodells CESM1.2, heutige Klimavariabilität in der Region zu simulieren, wird anhand von Beobachtungs- und Reanalysedaten ausgewertet. Abbildung 1d zeigt die CESM1.2-Simulation (1° Modellauflösung) der Jahresmitteltemperatur (2 m; Mittel über den Zeitraum 1900-2000) in der pontokaspischen Region im Vergleich zu Beobachtungsdaten (Abb. 1a) und Modellversionen mit vereinfachter Atmosphärenphysik (sog. CAM4-Atmosphäre) bei 2° (Abb. 1b) und 1° (Abb. 1c) Gitterauflösung. Obgleich die Verwendung einer reduzierten Atmosphärenphysik (CAM4-Simulationen) erheblich Rechenzeit erspart (Faktor 4 gegenüber CAM5 bei gleicher Gitterauflösung), sind die Abweichungen in der Simulation gegenüber den Beobachtungswerten zu groß, um diesen Ansatz weiter zu verfolgen. Die Modellvariante mit hoher (1°) Gitterauflösung und komplexer Atmosphärenphysik (CAM5) liefert die mit Abstand realistischste Simulation (auch in anderen Klimavariablen, die hier nicht gezeigt sind) und wird daher auch im weiteren Verlauf des Projektes verwendet werden.

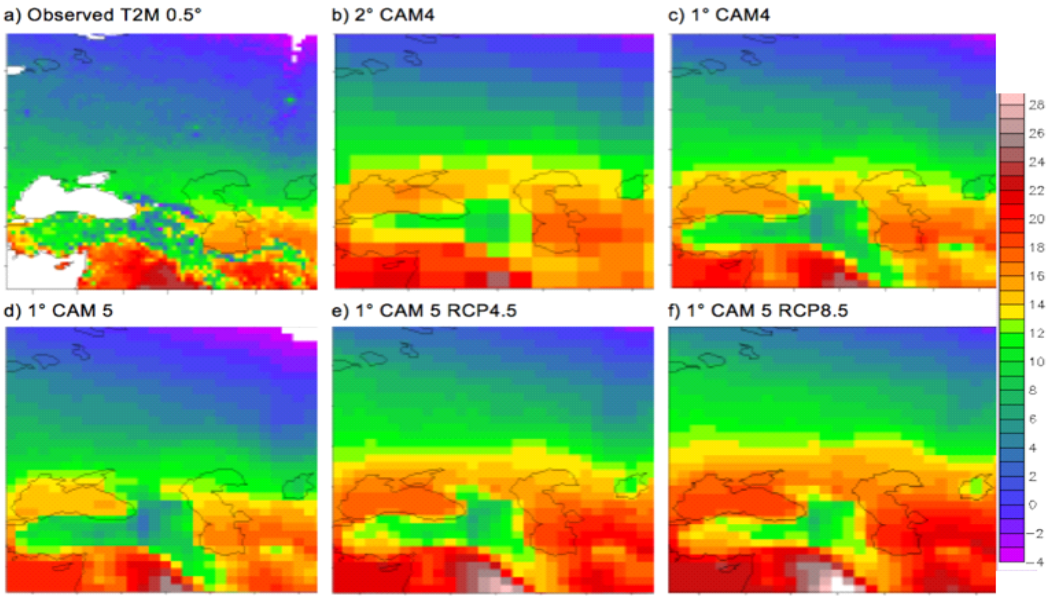

Abb. 1: Jahresmitteltemperaturen (2 m) in °C gemittelt über den Zeitraum 1900-2000. (a) Beobachtungsdaten, (b-d) historische CESM1.2-Simulationen für verschiedene Modellvarianten (siehe Text), (e-f) CESM1.2-Projektionen für den Zeitraum 2020-2100 unter verschiedenen RCP-Szenarien (RCP4.5, RCP8.5).

Abbildung 2 zeigt als Beispiel für heutige Klimavariabilität den Einfluss der Nordatlantischen Oszillation (NAO; das dominante Muster zwischenjährlicher Klimavariabilität über dem Nordatlantik) sowie des Ostatlantischen Musters (EA: East Atlantic Pattern; zweit-

dominantes Muster zwischenjährlicher Klimavariabilität über dem Nordatlantik) auf das pontokaspische Hydroklima in der historischen CESM1.2-Simulation. Positive NAO-Zustände, verbunden mit anomal großen Luftdruckdifferenzen zwischen Island und den Azoren, resultieren in reduzierten Nettoniederschlägen insbesondere im Wolga-Becken, ebenso wie negative EA-Zustände, die mit anomal niedrigem Luftdruck über dem östlichen Nordatlantik der mittleren Breiten verbunden sind.

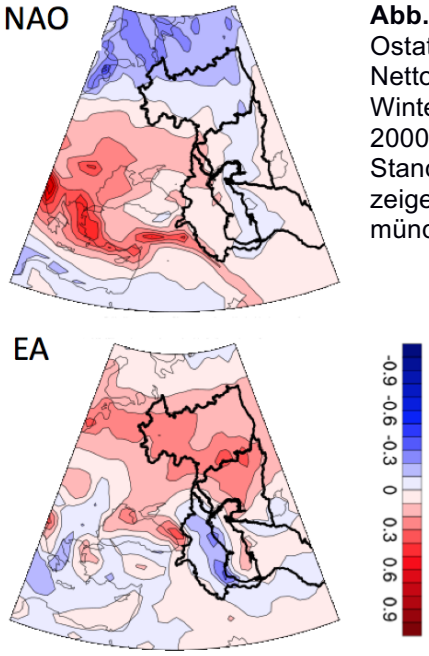

Abb. 2: Einfluss der Nordatlantischen Oszillation (NAO) sowie des Ostatlantischen Musters (EA: East Atlantic Pattern) auf den Nettoniederschlag in der pontokaspischen Region für die Wintermonate Dez.-Feb. simuliert in CESM1.2 für den Zeitraum 1900-2000 dargestellt als Regressionskarten (Einheiten in mm/d pro Standardabweichung des entsprechenden Index). Fette Kontourlinien zeigen das Einzugsgebiet der Flüsse, die im Kaspischen Meer münden.

Vorträge/Poster

- Nandini *et al.* (2016) *Historical and future climates of the Ponto-Caspian basins simulated with the CESM1.2.2 Model*. Poster Presentation and Oral Presentation at The International Union for Quaternary Research (INQUA). 27th August, 2016, University of Reading, England.
- Nandini *et al.* (2017) *Climates of the Caspian Basin from 1850-2100 in the CESM1.2.2*. Poster Presentation at Marie-Curie Alumni Association (MCAA) Conference, University of Salamanca, 24-25th March, 2017.
- Nandini *et al.* (2017) *Past and future impact of North Atlantic teleconnection patterns on the hydroclimate of the Caspian catchment area in CESM1.2.2 and observations*. Poster Presentation at European Geosciences Union (EGU) General Assembly, Vienna, 23-28th April, 2017.
- Nandini *et al.* (2017) *Teleconnections driving the Caspian hydroclimate (1850-2100): Models and observations*. Oral Presentation at PAGES OSM conference, 9-13th May, 2017, Zaragoza, Spain.

6.17 *hbm00045:* Determination of vertically resolved trends in the stratospheric ozone from SCIAMACHY limb measurements

HLRNProject ID:	hbk00045
Run time:	IV/2015 – II/2017
Project Leader:	Dr. Alexei Rozanov
ProjectScientists:	Dr. N. Rahpoe, C. Arosio
Affiliation:	Institute of Environmental Physics, University of Bremen

Overview

The importance of stratospheric ozone layer has been widely discussed by the scientific community. Playing a key role in the radiative budget of the Earth's atmosphere the stratospheric ozone also protects the biosphere from the harmful UV radiation and is closely related to stratospheric circulation and meteorology. After anthropogenic emissions of several strong ozone depleting substances have been ruled out by the Montreal Protocol and its amendments, the severe ozone decline discovered in early eighties of the last century (widely known as Antarctic ozone holes) began to slow down and even some indications of the ozone recovery have been inferred from observations. In the present time the vertical distribution of stratospheric ozone trends has been moved into the focus. Analyzing vertically resolved time series of tropical ozone, scientists agree in their conclusions that a significant ozone recovery is seen in the middle to lower stratosphere (below about 30 km) while a strong ozone depletion is observed at altitudes about 35 km. A discussion if the latter phenomenon has purely dynamic or also chemical reasons is currently ongoing in the scientific community. Being vertically integrated these opposite trends result in a slightly positive contribution which explains the signatures of a recovery seen in the observations of ozone total column.

In the framework of this project global vertical distributions of ozone obtained from measurements of the scattered solar light in the limb viewing geometry from the space-borne SCIAMACHY (SCanning Imaging Absorption spectroMeter for Atmospheric CHartograohY) instrument onboard the European satellite Envisat are analyzed. During the first phase of the project the retrieval algorithm has been improved with the main focus to fix previously identified data quality issues. The global data set over the entire operation time of the SCIAMACHY instrument obtained with the improved retrieval algorithm is to be used to determine trends in stratospheric ozone with a particular focus to explain the reported discrepancies between observations from different instruments in the tropical stratosphere. The final goal is to improve our general knowledge on stratospheric ozone trends needed for a better understanding chemical and dynamic processes in the Earth's atmosphere.

Results

Until the end of 2016 about three fourths of the total data amount has been processed. Due to technical reasons the data in the beginning of the SCIAMACHY operation time as well the measurements within the South Atlantic Anomaly (SAA) were not yet processed.

To assess the quality of the improved retrieval version, the obtained data set has been validated using the coincident measurements from space-borne MLS (Microwave Limb

Sounder) instrument on Aura satellite of NASA [1] as well as from balloon-borne ozone sondes.

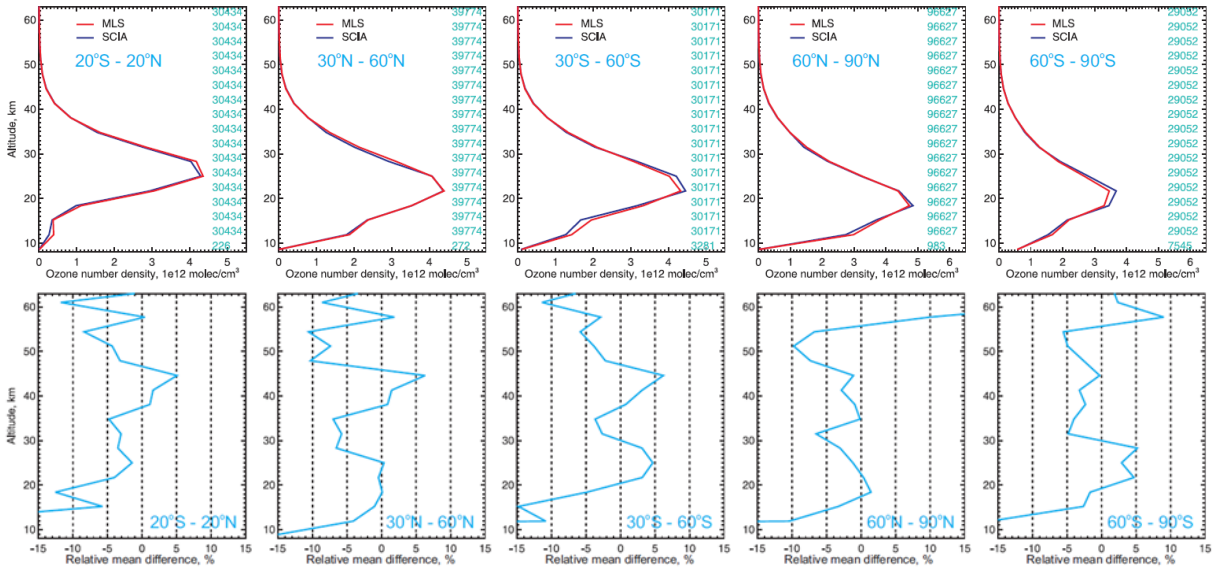

Figure 1: Comparison to MLS measurements. Upper panels: average vertical profiles of ozone number density from SCIAMACHY (blue) and MLS (red). Lower panels: Percentage relative mean difference.

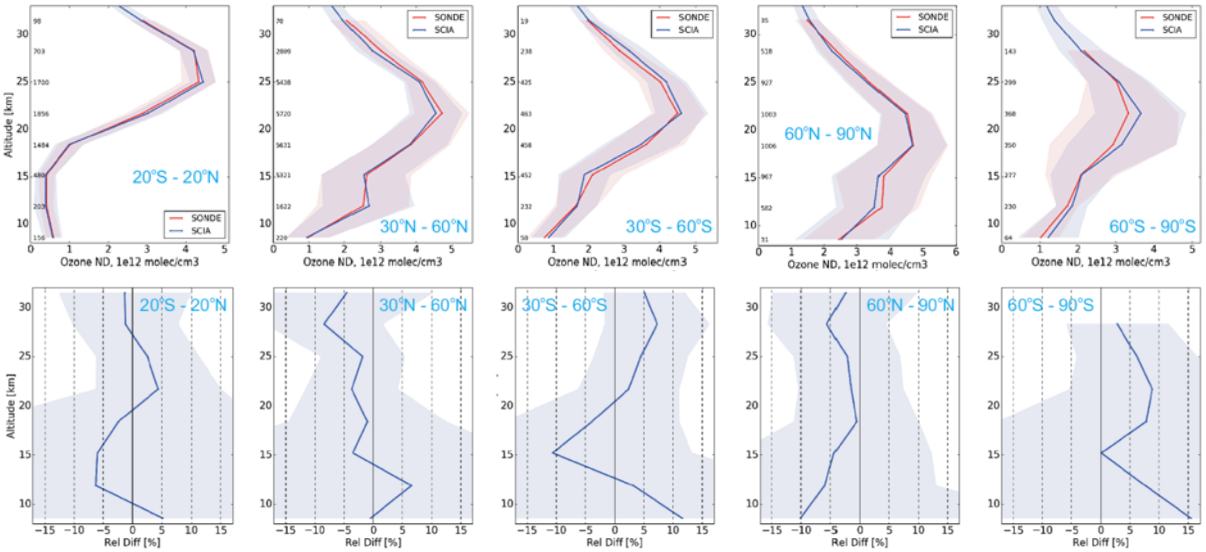

Figure 2: Comparison to in-situ ozone sonde measurements. Upper panels: average vertical profiles of ozone number density from SCIAMACHY (blue) and ozone sondes (red). Lower panels: Percentage relative mean difference.

Figure 1 presents comparison results for the period from January 2004 to April 2012 with respect to MLS. The upper panels show vertical profiles of the ozone number density for SCIAMACHY (blue) and MLS (red) averaged within 5 latitude bands. The green-blue numbers on the right of each plot show the number of pairs of coincident measurements from both instruments included in the comparison at each altitude level. The lower panels show the percentage relative mean difference between two data sets, (SCIAMACHY – MLS)/MLS.The comparisons were performed for pairs of coincident measurements with

maximum distance of 100 km and maximum time difference of 6 hours. The plot demonstrates that both data sets generally agree within 5% in the stratosphere. This represents a major improvement of the current retrieval version V3.5 with respect to the precursor version, V2.5, for which relative differences of up to +20% in the tropical stratosphere and mid-latitude upper stratospherewere reported, see e.g. [2].

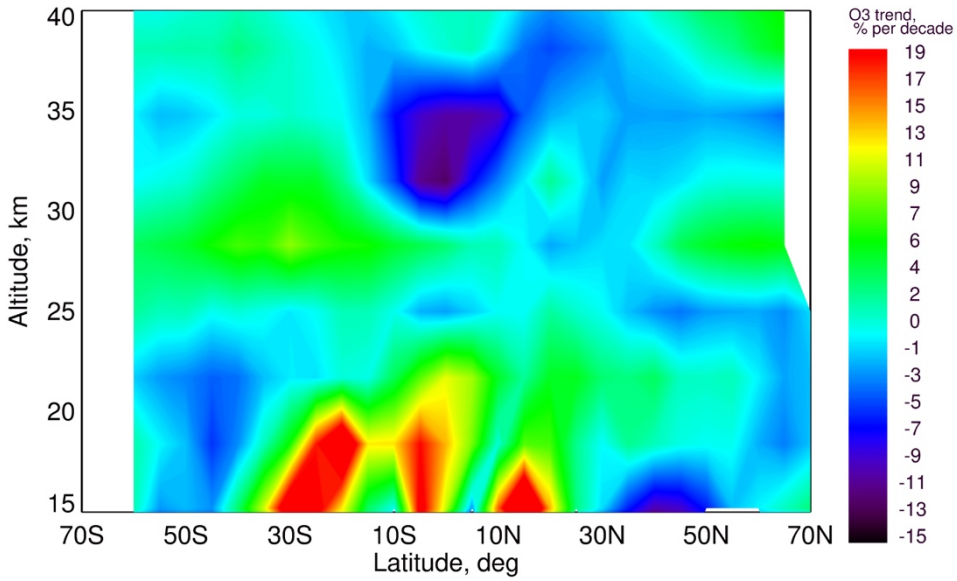

Figure 3: Ozone trends calculated from SCIAMACHY V3.5 ozone vertical profile data (2004 – 2012).

Figure 2 shows the results of the comparison with ozone sonde measurements. The coincident ozone sonde data from World Ozone and Ultraviolet Radiation Data Centre (WOUDC) were used. The coincidence criteria of 5° latitude, 10° longitude, and 6 hours were used for all measurements except for high southern latitudes, where 2.5° latitude, 5° longitude and 12 hours were used instead. The optimal coincidence criteria were determined by tightening the criteria until the difference between the data sets does not change significantly any more. The upper panels show vertical profiles of the ozone number density for SCIAMACHY (blue) and ozone sondes (red) averaged within 5 latitude bands. The lower panels show the percentage relative mean difference between two data sets, (SCIAMACHY – sonde)/sonde. As one can see from the plot, the relative differences between the two data sets are of the similar magnitude as those between SCIAMACHY and MLS and lie mostly within 5%. Even in the troposphere the measurements agree mostly within 5% in the tropics and in the northern mid-latitudes and within 10% in high latitudes and southern mid-latitudes.

A preliminary trend analysis has been performed using the newly generated SCIAMACHY ozone data set of version 3.5. The trends were calculated in a similar way as before (see e.g. [3]) employing the multivariate linear regression accounting for seasonal terms and the contributions from QBO (Quasi-Biennial Oscillation) and ENSO (El Niño–Southern Oscillation). The results of this investigation are shown in Figure 3. Generally, the conclusions for the tropical ozone remain the same as before. Below 30 km the observed ozone trends are dominating positive while significant negative trends are seen between 30 and 37 km. However, the magnitude of these negative trends is now -15% per decade rather than -26% as was obtained with the precursor version 2.5. Preliminary comparisons show that these values are in much better agreement with those reported from other instruments. More detailed comparisons and quality assessments are ongoing.

In addition the stratospheric ozone data generated within this project were used to investigate the increase in tropospheric ozone over the Arabian See area. The results of this study are published by Jia et al. [4].

Outlook

The currently missing data in the beginning of the SCIAMACHY mission (08.2002 – 12.2003) as well as the measurements within SAA are planned to be retrieved and their quality assessed. Upon the obtained results a decision is to be made whether the length and sampling of the time series can be extended using this data or it should be rejected to preserve the overall quality of the time series.

References:

[1] Froidevaux, L., et al., Validation of Aura Microwave Limb Sounder stratospheric ozone measurements, J. Geophys. Res., 113, D15S20, doi:10.1029/2007JD008771, 2008.

[2] Tegtmeier, S., et al. (2013), SPARC Data Initiative: A comparison of ozone climatologies from international satellite limb sounders, J. Geophys. Res. Atmos., 118, 12,229–12,247, doi:10.1002/2013JD019877.

[3] Gebhardt, C., Rozanov, A., Hommel, R., Weber, M., Bovensmann, H., Burrows, J. P., Degenstein, D., Froidevaux, L., and Thompson, A. M.: Stratospheric ozone trends and variability as seen by SCIAMACHY from 2002 to 2012, Atmos. Chem. Phys., 14, 831-846, doi:10.5194/acp-14-831-2014, 2014.

[4] Jia, J., Ladstätter-Weißenmayer, A., Hou, X., Rozanov, A., and Burrows, J.: Tropospheric ozone maxima observed over the Arabian Sea during the pre-monsoon, Atmos. Chem. Phys., doi:10.5194/acp-2016-786, in press, 2017.

Publications

1. Jia, J., Rozanov, , A. Ladstätter-Weißenmayer, A., and Burrows, J. P., Global validation of SCIAMACHY limb ozone data (versions 2.9 and 3.0, IUP Bremen) using ozonesonde measurements, Atmos. Meas. Tech., 8, 3369-3383, 2015.
2. Jia, J., Ladstätter-Weißenmayer, A., Hou, X., Rozanov, A., and Burrows, J.: Tropospheric ozone maxima observed over the Arabian Sea during the pre-monsoon, Atmos. Chem. Phys., doi:10.5194/acp-2016-786, in press, 2017.

Presentations

1. Rozanov, A., J. Jia, E. Malinina, N. Rahpoe, K. Weigel, A. Hilboll, P. Liebing, V. Rozanov, H. Bovensmann, and J. P. BurrowsUTLS observations from SCIAMACHY, UTLS Observation Workshop, Jointly organised by The Global Atmosphere Watch Programme (GAW), SPARC and NDACC, WMO Headquarters, 24-27 May 2016, Geneva, Switzerland.
2. Rozanov, A. Hilboll, E. Malinina, K. Weigel, V. Rozanov, H. Bovensmann, and J. P. Burrows, Ten years observations of the stratospheric composition from SCIAMACHY instrument on Envisat, 9th IAGA - ICMA/IAMAS - ROSMIC/VarSITI/SCOSTEP workshop on Long-Term Changes and Trends in the Atmosphere, Leibniz IAP, 19-23 September 2016, Kühlungsborn, Germany.
3. Rozanov, A., C. Arosio, J. Jia, N. Rahpoe, K.-U. Eichmann, and J. P. Burrows, Validation of O_3 vertical distributions retrieved from SCIAMACHY limb measurements: IUP Bremen scientific processor V3.5, ACVE-2016: Atmospheric Composition Validation and Evolution workshop, ESA/ESRIN, 18-20 October 2016, Frascati, Italy.

6.18 *hbp00003:* Encounters of Neutron Stars

HLRN-Projektkennung:	hbp00003
Laufzeit:	IV/2010 – IV/2016
Projektleiter:	Prof. Dr. C. Lämmerzahl, Prof. Dr. S. Rosswog
Projektbearbeiter.	Emanuel Gafton, Emilio Tejeda
Institut / Einrichtung:	ZARM, Universität Bremen; Oskar Klein Centre for Cosmoparticle Physics, Stockholm University, Stockholm, Sweden

Overview

- Mergers of two compact objects (neutron stars or black holes) are the prime targets of existing **gravitational wave** detectors. Four decades of preparatory work recently been crowned by the first ever direct detection of gravitational waves from two merging black holes.
- If at least one neutron star is involved, such mergers eject very neutron-rich matter which (via a so-called "rapid neutron capture process") produces the **heaviest elements in the Universe** (like platinum, gold or uranium).
- There is an interesting link between these two topics: the radioactive decay of freshly produced heavy elements produces an electromagnetic flash **"macronovae"** that will help to localized the gravitational wave source in the sky. Without such a transient the source is very difficult to localize: for the first detection of two merging black holes the sky localization is only known to within 600 square degrees (apparent size of the full moon: 0.3 square degrees).
- We had used a large part of our HLRN computing time to predict such macronovae. In June 2013, the first ever example of a macronova has been detected with properties close to our predictions. This observation boosts the confidence that mergers of compact objects are major sources of the heaviest elements in the cosmos.

Introduction

Stars with more than eight solar masses end their lives in cataclysmic fireworks called supernovae. During this explosion their luminosity rivals those of whole galaxies. Supernovae eject most of their mass into space where it forms the basis for the next generation of stars. The stellar centres, however, become enormously compressed and – if the star was not too massive – the explosion produces a neutron star, or otherwise a black hole of a few solar masses. Neutron stars can be thought of as gigantic atomic nuclei: with a mass of about 1.4 solar masses and radii of only 12 km their central densities substantially exceed the density in an atomic nucleus ($\rho_{nuc} = 2.7 \times 10^{14}\, g cm^{-3}$).

In some cases these exotic stars are observed in binary systems where they orbit their common centre of mass. Due to their enormous compactness, such stars can revolve around each other at very small separations and in such systems strong-field gravity effects become important, making such systems excellent laboratories to test theories such as Einstein's theory of General Relativity. In fact, the first indirect evidence for the existence of gravitational waves came exactly from such a system and it earned its discoverers, Russel

Hulse and Joseph Taylor, the Nobel Prize for Physics in 1993. One implication of the emission of gravitational waves is that the binary orbit shrinks further until the stars finally merge. This releases gigantic amounts of gravitational energy, more than the Sun could radiate away during the whole lifetime of the Universe. The final merger most likely causes (a fraction) of the brightest explosions in the Universe since its beginning in the Big Bang, so-called Gamma-Ray Bursts.

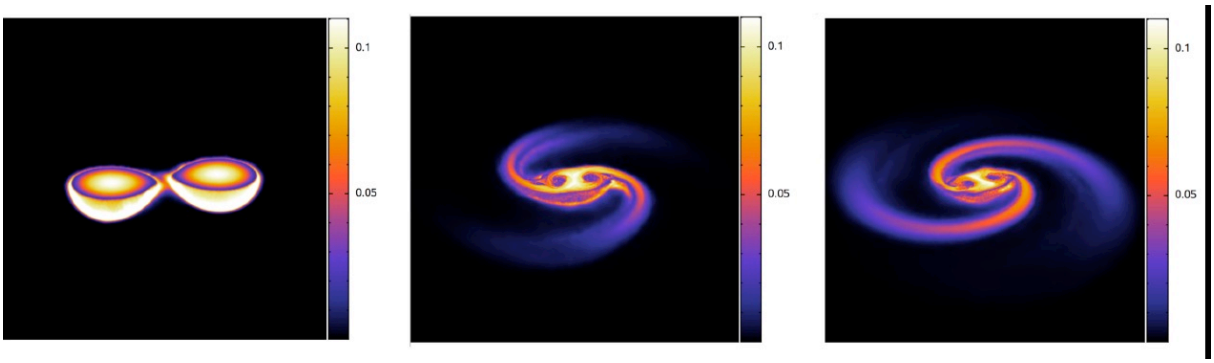

Fig. 1: Merger of two 1.3 and a 1.3 $M_\odot$ neutron star. Shown are volume renderings of the electron fraction (=number of electrons per nucleon). This quantity is pivotal for the resulting formation of heavy elements via the rapid-neutron capture process. To allow a view inside, only the lower part of the matter distribution is visualized. From Rosswog et al. in prep. (2017), arXiv: 1611.09822.

On September 14, 2015, the American LIGO detectors detected for the first time directly a gravitational wave: they saw the inspiral and final merger of 29 and an 36 $M_\odot$ black hole. In our HLRN project we study the question how different mergers and collisions are in a) their gravitational wave, b) neutrino and c) electromagnetic emission. Moreover, we want to understand d) what their contribution to the cosmic inventory of heavy nuclei is.

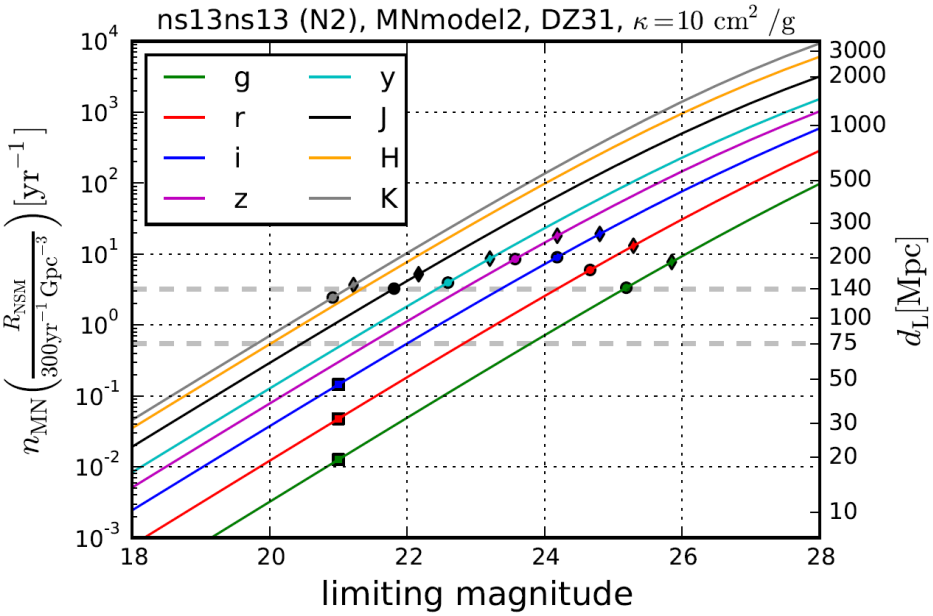

Fig. 2: Predicted number of macronovae detections. The markers show the expected depths for a 60-second (circle) and 180-second (diamond) exposures wih the VISTA telescope (J, K band) or Large Synoptic Survey Telescope (LSST). Square markers show the expected numbers for a depth of 21 mag in i-band as expected for the Zwicky Transient Facility (ZZTF).

Recent Results

We have performed a very large set of simulations where we have explored the parameter space of neutron star mergers with unprecedented breadth and numerical resolution. Such a merger ejects ~ 1% of a solar mass in extremely neutron rich matter: out of 100 nucleons only 3 are protons, the rest are neutrons. These are ideal conditions for the formation of heavy elements via "rapid neutron capture" or "r-process". Indeed our calculations show that in this way a very robust pattern of nuclear abundances is produced that is very similar to what is observed throughout the Universe (the solar system and various stars).

A major focus in the last year has been this type of element formation and in particular the electromagnetic transients that are produced by the radioactive decays of the freshly produced nuclei. These transients called "macronovae" are a crucial link between ifferent phenomena: gamma-ray bursts, enormously bright flashes of gamma-rays, gravitational waves and – of course – the formation of the heaviest elements in the cosmos. The importance of macronovae comes through the complementary information they provide: from the gravitational wave signal one can extract the parameters of the merging system (masses, spins etc.), but – since the sky localisation through gravitational waves is very poor (the first ever gravitational wave detection could – due to the absence of an electromagnetic signal – only be localized to 600 square degrees; the full moon as seen from Earthhas only 0.3 square degrees) – one is essentially blind with respect to the astrophysical environment in which the merger occurs. If detected coincidently in electromagnetic waves, one learns in addition to the binary parameters also about the astrophysical environment, say the type of host galaxy, the density of the surrounding medium etc. This can provide on the one hand confidence about the nature of the gravitational wave source, but on the other hand also constrains the stellar evolution of binary stars.

In the least year we have mainly focussed on the prediction of such electromagnetic transients. They are ejected via several channels: extremely neutron-rich matter is ejected via dynamic (hydrodynamic and gravitational) interaction and a second channel, somewhat proton-richer, is blown off the merged remnant via neutrinos. A remnant emits neutrinos at enormous luminosities: they are about 20 orders of magnitude(!) larger that the (electromagnetic) luminosity of our Sun. As we have found in recent studies (Perego et al. 2014, Martin et al. 2015), neutrinos emitted in one part of the remnant can be absorbed in another part and this blows off a strong wind from the remnant. In a close collaboration with observational astronomers we have made detailed predictions for the expected event rates for a number of telescopes, see Fig. 2. Such predictions are crucial to design optimal strategies to detect electromagnetic counterparts of gavitational wave sources.

Outlook

We have investigated in detail the fate of two compact objects, either neutron stars or a neutron star with a stellar-mass black hole, that either merge after having having been driven together by the emission of gravitational waves or that collide dynamically, say, in a Globular Star Cluster. We have predicted in detail the observable signatures in various channels: gravitational waves, neutrinos and electromagnetic emission ("macronova"). In June 2013 the first ever macronova event has been detected, with properties close to our predictions. Such predictions will substantially enhance the effective sensitivity of existing gravitational wave detector facilities such as Geo600, LIGO, VIRGO. Our current and future efforts focus on enhancing and refining further the physics input in our simulations (more General Relativity, more refined nuclear heating physics, more sophisticated neutrino treatment) and on implementing computationally more efficient gravity solvers.

Publications from 2016 HLRN results

[1] *The Impact of Fission on R-Process Calculations*, Eichler et al., Journal of Physics: Conference Series, Volume 665, Issue 1 (2016)

[2] *Optical Thermonuclear Transients from Tidal Compression of White Dwarfs as Tracers of the Low End of the Massive Black Hole Mass Function,* McLeod et al., ApJ 819, 3 (2016)

[3] *Magnetohydrodynamical simulations of a deep tidal disruption in general relativity*, O. Sadowski, E. Tejeda, E. Gafton, S. Rosswog, D. Abarca, MNRAS, 03, (2016)

[4] *Detectability of compact binary merger macronovae*, S. Rosswog et al., Classical and Quantum Gravity, in press (2017); arXiv:1611.09822

[5] *Tidal disruptions by rotating black holes: relativistic hydrodynamics with Newtonian codes*, Tejeda et al., MNRAS, in press (2017); arXiv:1701.00303

[6] *The Properties of Short Gamma-Ray Burst Jets Triggered by Neutron Star Mergers*, Murguia-Berthier et al., ApJ 835, L34 (2017)

[7] *A line-smeared treatment of opacities for the spectra and light curves from macronovae*, Fontes et al., submitted to MNRAS (2017); arXiv:1702.02990

Several papers from HLRN calculations are currently in preparation

Selection of scientific talks where this work was presented

- *Electromagnetic transients from neutron star mergers*
  Conference Neutron Star Mergers: from gravitational waves to nucleosynthesis; Hirschegg, January 17, 2017
- *Neutron star mergers: what else apart from gravitational waves?*
  Conference on the Theoretical Foundations of Gravitational Waves; Stockholm October 10, 2016
- *Neutron star mergers, their nucleosynthesis and electromagnetic transients*
  Basel September 29, 2016
- *Theory of stellar mergers*
  Binary Stars in Cambridge, Cambridge, UK, July 27, 2016
- *Neutron star mergers: what else apart from gravitational waves?*
  Short Gamma Ray Bursts: from observation to numerical simulation, University of Trento, September 09, 2016
- *Disruptions of stars by massive black holes*
  Jena, January 27, 2016

Public Outreach

Some of the simulations and visualizations produced on HLRN have been selected for the **Multimedia performance "The Warped Side of the Universe"** with **Kip Thorne** (Caltech), **Paul Franklin** (Academy Awards/Oscar for the Best Visual Effects for the movies "Inception" (2011) and "Interstellar" (2015)) and **Hans Zimmer** (Academy Award/Oscar for Best Music "Lion King" (1995).

6.19 *hbp00029:* Carrier dynamics and optical properties of transition metal dichalcogenides

HLRN-Projektkennung:	hbp0029
Laufzeit:	IV/2015 – III/2017
Projektleiter:	Dr. rer. nat. Michael Lorke, Dr. rer. nat. Christopher Gies, Prof. Dr. Frank Jahnke
Projektbearbeiter:	Dr. rer. nat. Alexander Steinhoff, Dr. rer. nat. Matthias Florian, M. Sc. Daniel Erben
Institut / Einrichtung:	Institut für Theoretische Physik, Universität Bremen

Introduction

The aim of this project is the investigation of carrier dynamics and optical properties in semiconducting two-dimensional transition metal dichalcogenides (TMDs) that are promising candidates for optoelectronic devices. Excited carriers and phonons are omnipresent under device operation conditions, thus we will investigate their influence on optoelectronic properties using state-of-the-art many-body methods. This will allow us to gauge the potential of devices for light emission or photovoltaic applications.

Results

1. Carrier-Carrier-Scattering in Monolayer MoS_2

In publication [1] we study the relaxation of optically excited carriers with large excess energy under the influence of carrier-carrier Coulomb interaction in a freestanding monolayer of MoS_2. The results are compared to carrier dynamics predicted for quasi-resonant optical pumping of excitonic resonances. For this purpose, we determine the evolution of the initial nonequilibrium carrier distributions and their relaxation across the whole Brillouin zone on the basis of a material-realistic ab initio description of the electronic band structure and screened Coulomb interaction. Thermalisation on a sub-100-fs timescale following above-band-gap excitation is possible for a wide range of excitation densities due to efficient carrier-carrier scattering in the two-dimensional material. We report significantly slower relaxation on a 5-ps-timescale for quasi-resonant excitation below the band gap, see Fig. 1.

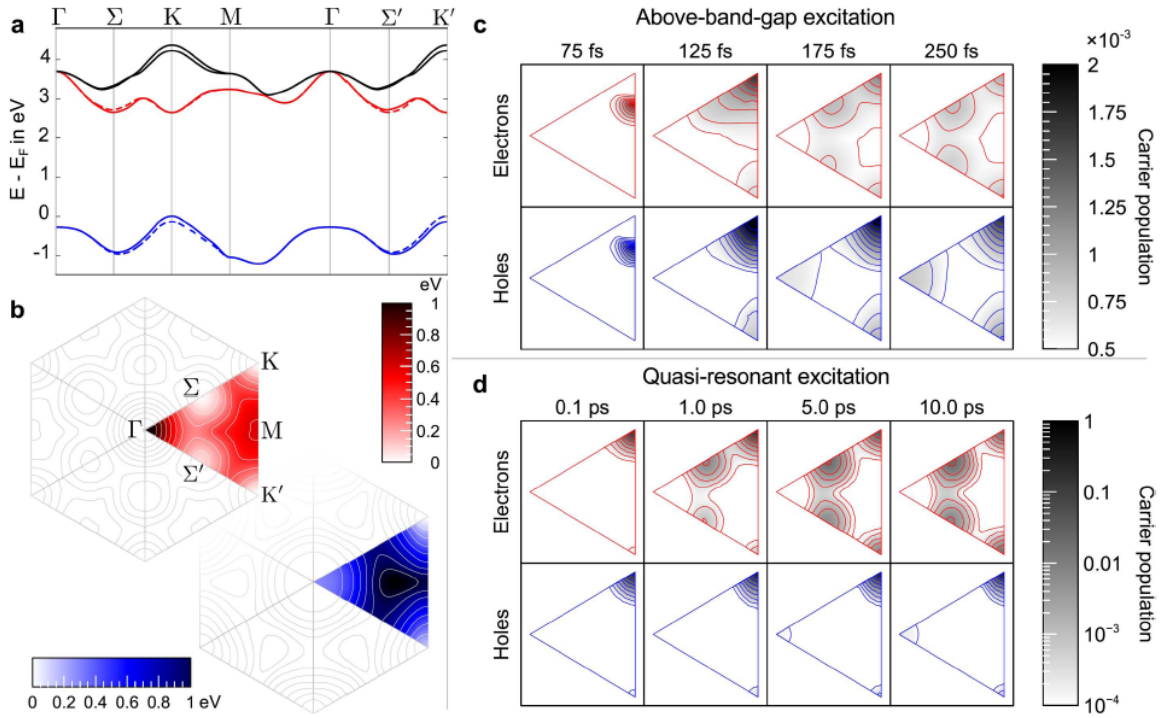

Fig.1: Microscopic characterisation of carrier dynamics. a) Band structure of monolayer MoS_2 as obtained from a G_0W_0 calculation including spin-orbit interaction. The relevant conduction and valence bands are marked in colour, while relevant bands with positive and negative z-direction of spin are represented by solid and dashed lines, respectively. **b)** Band structure of electrons and holes with positive z-direction of spin over the full Brillouin zone (BZ) corresponding to the curves in the top figure with gap energy subtracted. The irreducible part of the BZ is highlighted and high-symmetry points are shown, where band-structure valleys are depicted in white. **c)** Time evolution of the carrier populations with positive z-direction of spin on the irreducible part of the BZ after above-band-gap excitation. **d)** Same as c after quasi-resonant excitation. The optical excitation pulse has its peak amplitude at 75 fs.

2. Second-Harmonic Generation in Bilayer MoS_2

In publication [2] the electric-field-induced second-harmonic generation (SHG) in bilayer MoS_2 embedded into a microcapacitor device is demonstrated and explained in an experiment-theory collaboration. The nanostructure is illustrated in Fig. 2. By applying strong external electric fields the natural inversion symmetry of the bilayer is broken and the nonlinear conversion efficiency into frequency-doubled light is tuned. Based on band structures and optical dipole matrix elements involving up to 60 electronic bands obtained from density functional theory, we calculate second-harmonic signals from first principles.

The tunability observed in experiment is reproduced very well, see Fig. 2. Moreover, we show how the pronounced spectral dependence of the SHG signal reflects the band structure and wave function admixture of different atomic orbitals and that the field-induced second-harmonic generation relies on the interlayer coupling in the bilayer.

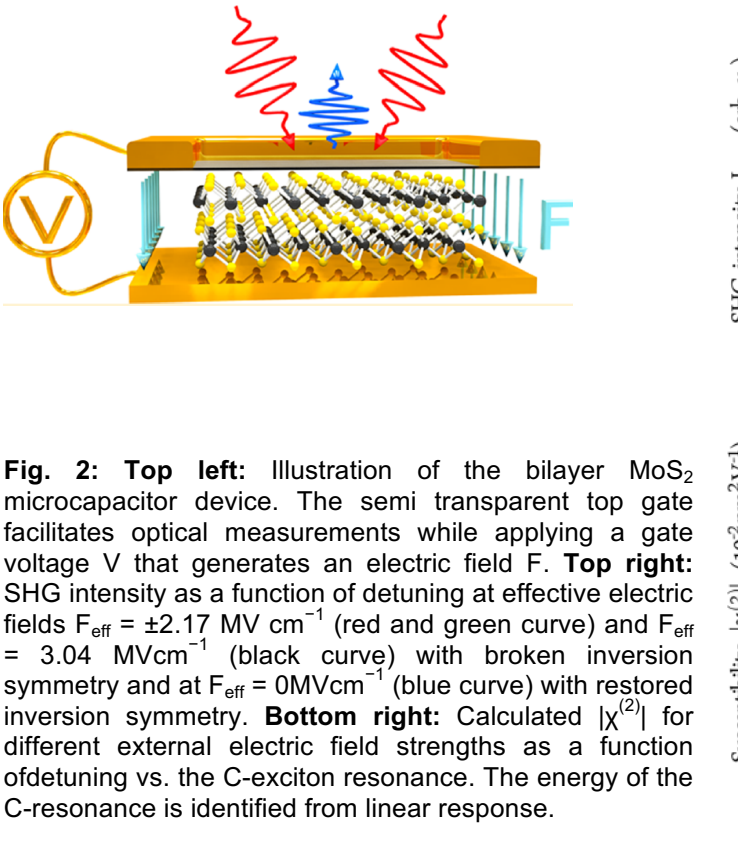

Fig. 2: Top left: Illustration of the bilayer MoS_2 microcapacitor device. The semi transparent top gate facilitates optical measurements while applying a gate voltage V that generates an electric field F. **Top right:** SHG intensity as a function of detuning at effective electric fields F_{eff} = ±2.17 MV cm^{-1} (red and green curve) and F_{eff} = 3.04 MVcm^{-1} (black curve) with broken inversion symmetry and at F_{eff} = 0MVcm^{-1} (blue curve) with restored inversion symmetry. **Bottom right:** Calculated $|\chi^{(2)}|$ for different external electric field strengths as a function ofdetuning vs. the C-exciton resonance. The energy of the C-resonance is identified from linear response.

Outlook

Ongoing work is concerned with the carrier-scattering and cooling efficiency of phonons in TMD semiconductors in connection with non-perturbative polaronic effects. Moreover, we aim at the characterization of trions under the influence of excited carriers and at material-realistic calculations of biexciton binding energies.

Publications

1. A. Steinhoff, M. Florian, M. Rösner, M. Lorke, T. O. Wehling, C. Gies and F. Jahnke, *2D Materials, **3**, 031006 (2016)*

2. J. Klein, J. Wierzbowski, A. Steinhoff, M. Florian, M. Rösner, F. Heimbach, K. Müller, F. Jahnke, T. O. Wehling, J. J. Finleyand M. Kaniber, *Nano Letters, **17,** 392 (2017)*

6.20 *hbp00030*: Correlation Effects in strongly correlated crystals: From ab-initio to model studies

HLRN Project ID:	hb00030
Run time:	IV/2015 – III/2017
Project Leader:	Prof. Dr. Tim Wehling
Project Scientists:	Malte Schüler, Malte Rösner, Elham Khorasani
Affiliation:	Institut für theoretische Physik, Bremen Center for Computational Physics

Overview

The metal-insulator transition (MIT) in vanadium dioxide (VO_2) between rutile-type (R) and monoclinic-type (M1) is a highly discussed topic in both theoretical and experimental condensed matter physics. It is accompanied with significant changes in the structural, electronic and optical properties, which can be triggered by different external stimuli (thermal, electrical, or optical) near room temperature. Because the MIT is associated with changes in the electrical resistance over several orders of magnitude, VO_2 appears as very promising material e.g. for sensor applications. Since both electron correlations and lattice deformation play a role in the MIT, VO_2 has become a model system for investigating the complex physics of metal insulator transitions from the viewpoint of fundamental theory. Over the last years, two mechanisms have been proposed: in the Mott-Hubbard picture, a pure electronic mechanism, electron-electron correlations causes the MIT, while in the Peierls picture, a temperature-driven mechanism (due to crystalline lattice deformations) induces it.

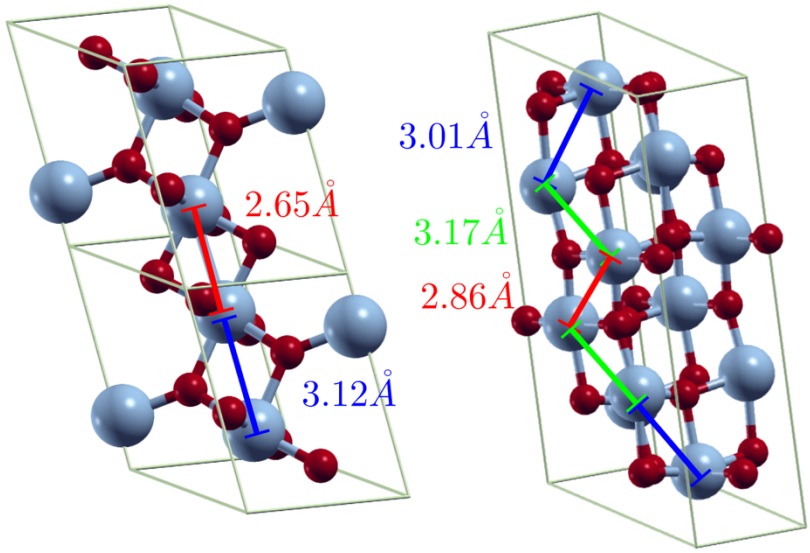

Fig. 1: Schematic of VO_2 in the M1 phase (left) and the high-temperature B-phase (Right). Vanadium ions are shown as grey spheres; small red spheres represent oxygen ions.

The phase diagram of VO_2 is very complex and comprises further phases such as the so-called metastable B-phase. VO_2(B) exhibits a metal-insulator transition somewhat below room temperature. While the MIT across the B-phase VO_2 has been studied by a few

theoretical and experimental methods, the role of electron correlations, in triggering the MIT between the low temperature and high temperature phases has remained elusive. We concentrate on VO_2 in M1 and B phase and investigate how structural changes alter the electronic structure and especially the effects stemming from electronic correlations. We perform LDA+DMFT calculations in order to grasp the electronic correlation effects and structural complexity of VO_2 on equal footing.

Results

For the initial study of the metal-insulator transition in the B-phase of VO_2, electronic structure calculations for the low- and high-temperature B-phases VO_2 have been performed by using GGA+U (GGA in the Perdew-Burke-Ernzerhof formulation) with the Vienna Ab Initio Simulation (VASP) package.

VO_2 (B) has a monoclinic structure with space group C2/m in which the V atoms are surrounded by O octahedrons sharing a common edge, as schematically shown in Fig. 1. Each vanadium atom is surrounded by an oxygen octahedron, resulting in a splitting of the d orbitals to triply degenerate t_{2g} and doubly degenerate e_g^{σ} states. An additional tetragonal distortion lifts the degeneracy of the t_{2g} state to a_{1g}, π_1 and π_2 states. The MIT of VO_2(B) is less sharp and occurs at a lower temperature than the M1→R MIT. In the following, the results of my calculations for VO_2 (B) are presented.

The high temperature B-phase VO_2 (HT) is metallic. The nearest-neighbor V-V distances are quite short (2.867 Å like in the metallic R-phase), while other V-V distances exceed 3 Å, as shown in Fig. 1. It is expected that at high temperature, the partial occupation of orbitals by the one itinerant electron is the reason for the metallic behavior.

In spin-polarized GGA+U calculations, U_{eff}=3.32 eV (U=4.0 eV and J=0.68 eV) was used, as determined by first principle calculations. We observe that for the high temperature B-phase, an insulating gap in the partially occupied 3d bands wrongly opens. Since GGA+U does not provide a correct description of the gap, we conclude that this simplified description of correlation effects is insufficient. Therefore, an approach which considers correlation more precisely is needed.

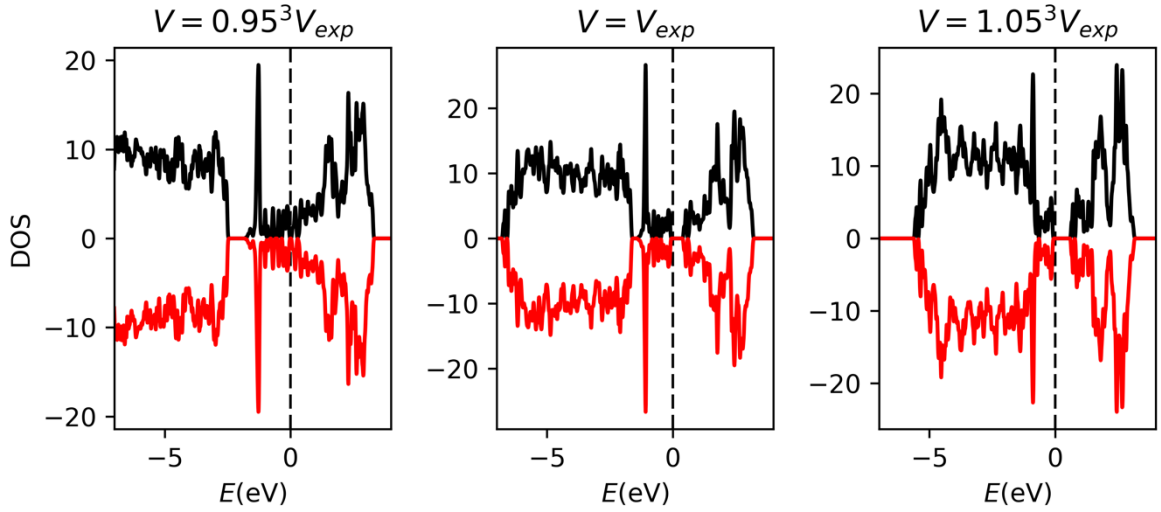

Fig. 2: Total density of states (DOS) for low temperature B-phase VO_2 (B) for different volumes 0.95^3-(left)-, 1.00^3(middle) and 1.05^3 -times the experimental volume with relaxation of the atoms.

In the low temperature B-phase (LT) with space group:C2/m, the experimentally obtained V-V distances across shared VO_6 octahedrons (see Fig. 1) indicate that the shortest V-V distance, 2.670 Å is even shorter than in the HT (2.867 Å), while other distances are almost unchanged. According to the Goodenough-explanation, V-V dimers form if the V-V distance is less than 2.92-2.94 Å. Thus, V ion pairs are formed in these sites and half of the V atoms in the LT form dimers. In the picture of Goodenough, the dimerization of the vanadium atoms leads to the splitting of the a_{1g} ($d_{||}$) partial density of states, into a lower-energy bonding and a higher-energy anti-bonding combination. The bonding states are located below the Fermi energy, while the anti-bonding states are above it. The V_d−O_p anti-bonding π_1 states are pushed higher in energy, due to the tilting of the pairs which increases the overlap of these states with O states. The single d electron occupies the a_{1g} -bonding combination, resulting in a (Peierls-like) band gap.

The DOS resulting from the spin polarized GGA+U calculation, gives a gap of 0.53 eV for the low temperature phase. It should be noted that there is no conclusive experimental result available at the moment for the band gap structure of the low temperature B-phase.

	$(0.95)^3$ V	V	$(1.05)^3$ V
$V(1)^{i}$ - $V(1)^{iv}$	3.142	3.307	3.472
$V(1)^{i}$ - $V(2)^{ii}$	3.010	3.005	3.151
$V(1)^{i}$ - $V(2)^{iv}$	2.851	3.005	3.151
$V(2)^{i}$ - $V(2)^{ii}$	2.537	2.670	2.804

Table I: Vanadium distances in low temperature VO2 (B) by increasing volume from 0.95 to 1.05 with ionic relaxation.

We have scaled the cell-size of the LT and optimized the atom positions to see, if larger cells lead to a loss of pairing. Spin polarized GGA+U calculations have been carried out for increasing volumes from 0.95^3 -to 1.05^3 -times the experimental volume, to prove the hypothesis that thermal expansion can decrease the effect of V-V pairing and make the gap of the low temperature phase gradually disappear with increasing temperature. The computed electronic densities of states are shown in Fig. 2. In the first plot (0.95^3-times the experimental volume) the shortest V-V distance, V-V separation in dimers, decreased from 2.670 to 2.537 Å, as given in Table I, and in spite of our expectation, a metallic ground state has been obtained. This runs against the Goodenough-explanation, since the separation is below the critical value, 2.94Å, so there should be a band gap. Expanding the volume (1.05^3 -times the experimental volume), the V-V dimerization distance as well as all other V-V distances have increased. Still an insulating ground state has been obtained although thermal expansion has increased the distances of dimers, decreasing the pairing effect. Obviously, B-phase VO_2 has a more complicated behavior than the monoclinic phase and even the insulating properties of the low temperature phase cannot be reliably described within DFT+U. To describe the complicated magnetic behavior, we use a many body approach: the static cluster dynamical mean-field theory (C-DMFT).

C-DMFT introduces a frequency dependent self energy which is non-local with respect to the V-V pairs. Furthermore, a previous study by Tomczack et al. (2007) showed that the frequency dependent self energy can be approximated by a static self energy. Such approximation leads to a reasonably good reproduction of the fully interacting one-particle

spectrum. We have reproduced this approach (sC-DMFT) for M1 and applied it to the low temperature B-phase.

The left panels of Fig. 3 display the partial DOS for the M_1 phase, calculated by using the GGA and GGA+sC-DMFT methods. It can be seen clearly that the static one-particle potential pushes the a_{1g} bonding and π^* bands apart. In fact, the down shift of the a1g bonding band together with an up shift of the π^* bands to higher energy is responsible for the opening of the gap. Furthermore, the obtained splitting between the bonding and anti-bonding states, due to dimerization, is considerably enhanced by non-local intra-dimer correlations. It indicates that the M1 phase of VO_2 is a correlated band insulator and intersite correlation effects within vanadium dimers is the driving mechanism of M1→R MIT in vanadium dioxide.

For the low temperature B-phase VO_2, the calculated partial DOS with GGA+sC-DMFT are presented in the right panels of Fig. 3. The top plot displays the partial DOS for a chain-forming V atom. It shows that for a non-dimerized atom, the bonding/antibonding splitting of a_{1g} state does not occur and the a_{1g} orbital locates above the Fermi energy. At the bottom, for a dimer, the a_{1g} state splits into a bonding combination below the Fermi energy and an anti-bonding combination above it. Dimers have similar behavior in both M1 and LT phase.

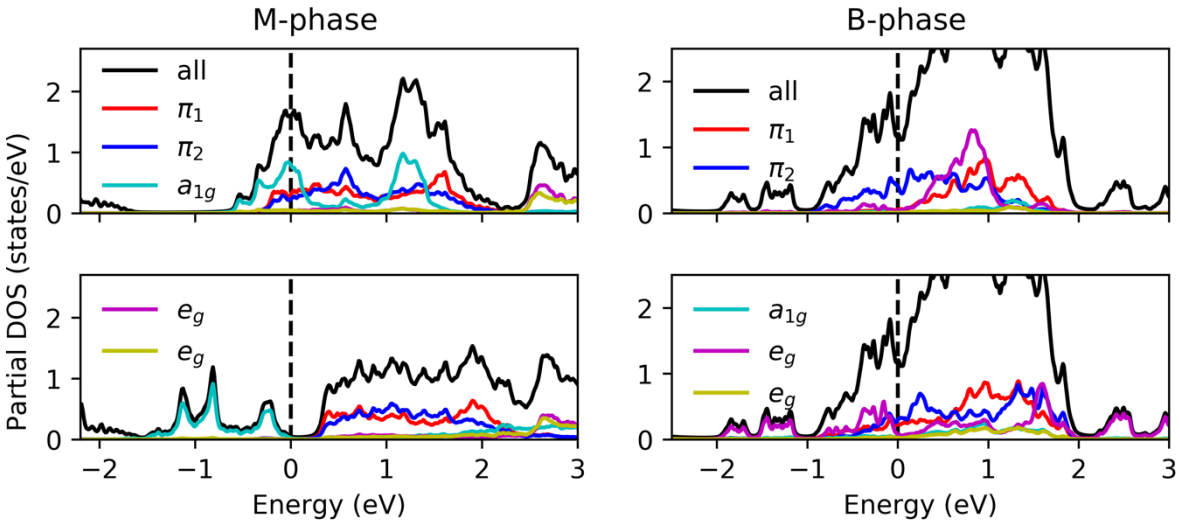

Fig. 3: Partial DOS for LT phase for non-dimerized V atom(top) and dimerized V atom(bottom) as calculated within the sC-DMFT method. Left panels: M1 phase. Right panels: B phase.

That is, the splitting for dimers between the bonding and anti-bonding states is increased by intra dimer correlations as shown by partial DOS in Fig. 3. In comparison to the M1 phase, the π^* -states are not pushed up in energy; so, the overlap of a_{1g} and π^* states leads to a metallic ground state also in the low temperature B-phase, in conflict to experiments. However, we can see a pseudo gap for dimerized V atoms and this underlines the insulating behavior of the low temperature phase. Still, analysis of our results for all V atoms shows that our calculation including static intra and inter site potentials, fails to reproduce the band gap in LT phase.

Outlook

In the M1 phase of VO_2, the MIT is assisted by a change in structure, i.e., dimerization of V-atoms along the z-axis, requiring nonlocal (cluster-) extensions to the DMFT in order to

properly describe the Mott-Peierls insulator. Experimentally, it is well known, that, e.g, VO_2-nanobeams undergo a structural and electronic phase-transition as a function of stress and temperature and the alloyed nanoplatelets $V_{1-x}Al_xO_2$ as a function of concentration x as well. The electric field on the transport properties of a 10-nm-thick, strained VO_2 film clearly show a MIT as a function of voltage and temperature this correlated material and the interplay between electron correlations, geometrical structure and electric-field doping.
For all of these systems we will first do ab-initio calculations using VASP and construct the corresponding low-energy models in the local crystal field basis on each V-atom. These low energy models consist of three orbitals in the R structure and six orbitals in the M1 structure, which serves as input for the multiorbital AIM using values from literature for the Coulomb matrix elements using the density-density approximation. This approximation neglects certain elements of the Coulomb matrix, which leads to smaller relevant matrices and a smaller sign problem. The corresponding AIM are solved by quantum Monte Carlo methods described above using the TRIQS 1.2 library applying single-site or cluster- DMFT, depending on the details of the system. We do this for two different inverse temperatures β (β[1/eV] = 20, 30) due to the high numerical complexity.

6.21 *hbp00034:* Effects of the interfacial transition metal intercalation on the Dirac surface states of topological insulators

HLRN Project ID:	hbp00034
Run time:	I/2016 – I/2017
Project Leader:	Dr. Bin Shao
Project Scientists:	Dr. Bin Shao, Dr. Liujiang Zhou, Miaomiao Han
Affiliation:	Bremen Center for Computational Material Science, Universität Bremen

Overview

Three dimensions (3D) topological insulators (TIs) possessing metallic states on the surfaces and a band gap in the bulk at the same time have drawn considerable attention in recent years. These nontrivial surface states have a linear dispersion relation in the form of a single Dirac cone and are protected by the time reversal symmetry (TRS). Therefore, when a magnetic interaction is introduced into TIs, the TRS is broken, opening a gap at the Dirac point and yielding a lot of intriguing quantum effects, such as topological magneto-electric effect, quantum anomalous Hall effect, weak localization behavior in transport, and enhanced spin transfer torque. By utilizing atomistic simulation methods, we aim to introduce magnetic interactions into TIs by inserting a transition metal intercalation between them and 2D layered normal insulators (NIs). In order to induce a perpendicular magnetization in between TIs and NIs, as the first step, it is significant to understand the nature of the magnetization of a single magnetic adatom on NI surfaces and propose an approach to tune its behavior.

Results

In the past project period, we have investigated the magnetization of a single magnetic adatom on a typical 2D NI – transition metal dichalcogenide (TMDC). Results provide us a better understanding on the magnetization of single adatoms on 2D NIs. In the calculations we have combined first-principles approach and effective Hamiltonian method to investigate the magnetic anisotropy and the magnetization dynamics of single adatoms on TMDCs.

To find the best candidate for the magnetic adatom, we have calculated the electronic and magnetic properties of all the 3d transition-metal (TM) adatom on a monolayer MoS_2 surface, as summarized in Table I. Results show that the most stable site of 3d TMs are Mo-top except for Sc, Ti, and Mn, in which it favors hollow site. For early TMs there is a discrepancy (~2 μ_B) between the total magnetic moment and that of TMs, while for late TMs such discrepancy disappears, indicating the hybridization between TM and MoS_2 is stronger in the former cases than that in the later. Due to this weak hybridization for late TM adatom it is more easy for itself to restore the free-atom orbital moment.

Given that an unquenched magnetic orbital moment, it is of great possibility to obtain large magnetic anisotropy arising from spin-orbit coupling. Since the ground state of Ni case is non-magnetic, we check the density of states of Mn, Fe, and Co cases in late TM adatoms. Our ab-initio calculation predicts that the ground state of spin of Co is double degenerate (S = ½) with d9 configuration, see Fig. 1(a). Because the symmetry of Mo-top is C_{3v}, the crystal field splits the five d-orbitals into two orbital doublets (E1, and E2) and a singlet (A1). The majority spin states are fully occupied and the Fermi energy resides in the E1 state in

minority spin. By extracting the parameters from the density of state for crystal field Hamiltonian, we diagonalized it and found a large perpendicular magnetic anisotropy [Fig.1(b)].

Table I: Summary of conductivities and magnetic moments of 3d magnetic adatoms at stable adsorption sites.

TM	Adsorption site	Conductivity	M(Tot) (μ_B)	M(TM) (μ_B)
Sc	Hollow	Metallic	1.00	0.25
Ti	Hollow	Insulating	0.00	0.00
	Mo-top	Metallic	4.00	1.93
V	Mo-top	Insulating	5.00	2.99
Cr	Mo-top	Insulating	6.00	4.24
Mn	Hollow	Insulating	3.00	3.03
	Mo-top	Insulating	3.00	3.03
Fe	Mo-top	Insulating	2.00	2.10
Co	Mo-top	Metallic	1.00	0.94
Ni	Mo-top	Insulating	0.00	0.00

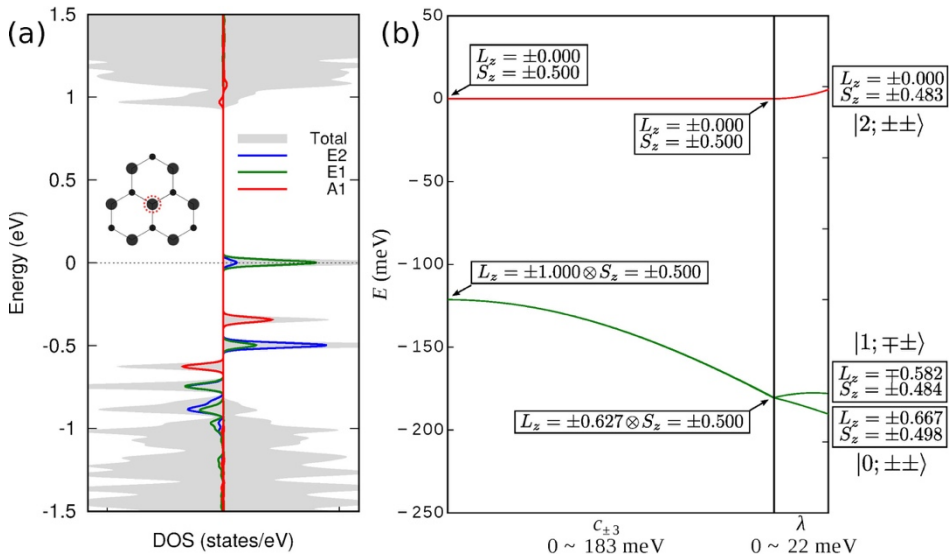

Fig. 1: (a) Projected density of states of a Co adatom on a Mo-top site of a MoS_2 with the GGA method. The Fermi level is at 0 eV. The red, green, and blue lines refer the A1, E1, and E2 states, respectively. The dash circle in the insert indicates the Mo-top site of the MoS_2 where the large (small) dots represent Mo (S) atoms. (b) Energy level diagram by diagonalizing Hamiltonian (1) with the crystal field parameters extracting from the DFT calculation of Co on MoS_2. L_z and S_z are the expectation value of orbital and spin angular momentum along z axis, respectively. The states are denoted by labels |n = {0, 1, 2, …}; L_zS_z = {±±; ∓±}>, respectively.

More interestingly, due to its interaction with charge carriers in MoS_2, the behavior of the magnetization of Co allows to be tuned from a quantum regime with full Kondo screening to a regime of Ising spintronics where its spin-orbital moment acts as classical bit, which can be written and erased electronically and optically. Specifically, as shown in Fig.2 (left), when the system is moderate electron-doped (μ>1.9 eV) or hole-doped (μ<0 eV) where carriers are contributed mainly by dxy and dx^2-y^2 orbital, the spin lifetime of the Co spin state will be dramatically decreased to less than a nanosecond.

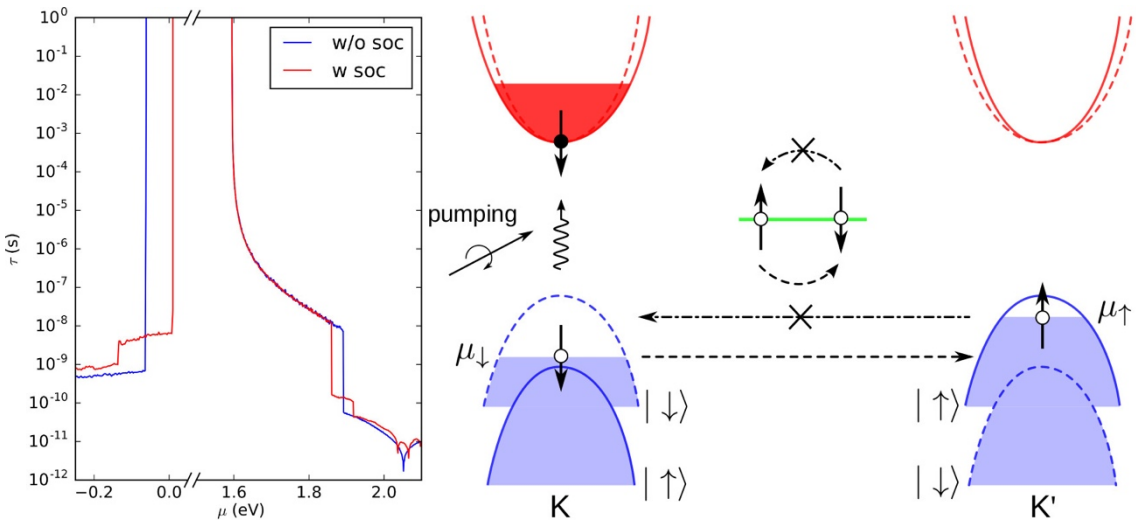

Fig. 2: The spin lifetime τ as a function of chemical potential μ (left) and schematic diagram of the optical spin orientation (right). In the left panel, the blue and red line refer the result without and with SOC, respectively. In the right panel, the circularly polarized optical pumping excites electron and hole pairs in spin down state at K valley. Because the outgoing state for holes in the scattering from K' to K is occupied, the corresponding transition is forbidden. As long as the chemical potential of different spin channel is imbalanced, the spin orientation of TM adatoms will be flipped accordingly via scatterings.

Moreover, the spin-valley coupling in MoS_2 provides an optical way to select the spin state of charge carriers, aligning the spin state of Co accordingly, see Fig.2 (right). Our analysis based on a master equation shows that once the chemical potential of different spin channel is imbalanced, the Co spin state will be flipped and preserved, suggesting a potential application in spintronics.

Outlook

Altogether, we showed that the interplay between adatoms and substrates can seriously affect the magnetic properties of the system. In return, it also provides an approach to tune the magnetic state of adatoms by carefully selecting the quantum state including spin and orbital states of carriers in substrate. Since the diluted transition-metal atoms intercalating between NIs and TIs are weakly correlated to each other, the results obtained in our investigations might be also effective to explain the magnetization dynamics of the intercalation layer of magnetic atom, providing a path to even tune the magnetization, which deserves to be investigated in the future.

Publications

1. B. Shao, M. Schüler, G. Schönhoff, T. Frauenheim, G. Czycholl, and T. O. Wehling, *Optically and electrically controllable adatom spin-orbital dynamics in transition-metal dichalcogenides (prepared to submit)*

Presentations

1. B. Shao, Ising spintronics in transition-metal dichalcogenides, Seminar in TU Darmstadt, Darmstadt, Germany, (2016)
2. B. Shao, Ising spintronics in transition-metal dichalcogenides, International Symposium on Advanced Functional and Computational Materials, Shenzhen, China (2017)
3. B. Shao, Ising spintronics in transition-metal dichalcogenides, Seminar in Institute of Physics, Chinese Academy of Sciences, Beijing, China (2017)
4. B. Shao, Ising spintronics in transition-metal dichalcogenides, DPG-Frühjahrstagung, Dresden, Germany (2017)

6.22 *hbp00035:* 3D Simulation eines Interferometers unter Berücksichtigung optischer Abbildungsfehler für ein Bose-Einstein Kondensat

HLRN-Projektkennung:	hbp00035
Laufzeit:	I/2016 – IV/2016
Projektleiter:	Prof. Dr. Claus Lämmerzahl
Projektbearbeiter.	Dr. Ertan Göklü
Institut / Einrichtung:	Universität Bremen/ ZARM

Überblick

Das schwache Äquivalenzprinzip besagt, dass Körper unabhängig von ihrer Masse in einem Gravitationsfeld gleich schnell fallen (Äquivalenz von schwerer und träger Masse). Verschiedene Ansätze zu Quantengravitationstheorien sagen eine Verletzung des Äquivalenzprinzips voraus. Eine Verletzung wäre der Beweis, dass Einsteins allgemeine Relativitätstheorie nicht auf allen Längenskalen gültig ist. Im Projekt PRIMUS wird sowohl experimentell, als auch theoretisch die Realisierung eines Interferometers mit Bose-Einstein Kondensaten (BEC) unter Mikrogravitation durchgeführt. Das langfristige Ziel ist der Test des schwachen Äquivalenzprinzips mit ultrakalten Quantengasen.

Im Vergleich zu Laserinterferometern wird bei Atominterferometern die Rolle von Materie und Welle vertauscht. Im letzteren Fall übernimmt der Laser die Rolle des Strahlteilers und Spiegels, wohingegen die Materiewelle die Rolle der kohärenten Strahlungsquelle einnimmt.

Für die theoretische Analyse und die Modellierung dieses Aufbaus vor dem Hintergrund hochpräziser Messungen ist es von enormer Wichtigkeit, die Wirkung von Fehlern der Laser-Phasenfronten auf die Eigenschaften des Strahlteilers zu verstehen. Dabei ist hier insbesondere von Interesse, wie bei einer „Double-Bragg“ -Spiegel und -Strahlteiler Konfiguration Spiegelunebenheiten des für die Retroreflektion der Laserstrahlen eingesetzten Spiegels sich auf die Phase der Bose-Einstein Kondensate und mithin auf die Verschiebung der Interferometer-Phase auswirken. Beispielsweise kann unter bestimmten Umständen der Strahlteiler keine 50% zu 50% Teilung mehr gewährleisten. Zudem kommt noch der Einfluss der Wechselwirkung der Teilchen untereinander und verschiedene Formen der Grundzustände (als anfängliche Wellenfunktion) hinzu, die zu veränderten Impulsverteilungen führen.

Ziel dieser numerischen Studie ist es, diese Fehlereinflüsse auf den Ausgang eines Interferometer Experiments zu untersuchen hinsichtlich der Präzision bei der Messung der Interferometer-Phase. Für diese Studie verwenden wir Programm Codes, die seit 2010 am ZARM entwickelt werden - unter anderem hauptsächlich im Rahmen des Vorgängerprojekts ATUS III (DLR Förderkennzeichen 50WM1342) – welche nun im Projekt PRIMUS (DLR Förderkennzeichen 50WM1642) Anwendung finden und weiterentwickelt werden.

Ergebnisse

Das Modell eines Mach-Zehnder Atominterferometers mit Double-Bragg-Diffraction Strahlteilern und Spiegeln wurde in 1D auf einem lokalen Rechner ausgiebig getestet. Um Teilchen-Teilchen Wechselwirkungen Rechnung zu tragen (Bose-Einstein-Kondensat), welche als nichtlinearer Term in der Bewegungsgleichung auftreten (Gross-Pitaevskii Gleichung) und Phasenfehler zu berücksichtigen (z.B. Unebenheiten der Spiegel), sind 3D Simulationen nötig, die auf dem HLRN durchgeführt wurden.

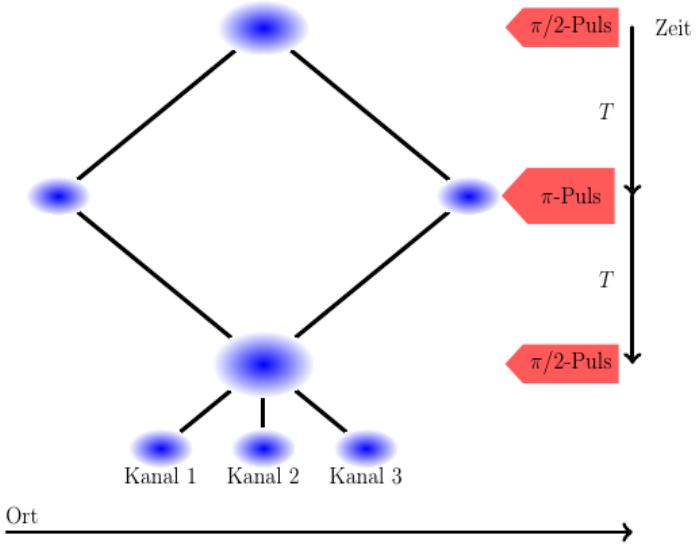

Abbildung 1: Schema eines Mach-Zehnder Atominterferometers mit Double-Diffraction. Der $\pi/2$-Laser-Puls dients als Strahlteiler, der π-Puls dagegen als Spiegel. Durch den zweiten $\pi/2$-Puls werden die beiden Strahlengänge überlagert. Für jeden der drei Kanäle wird anschließend die Teilchenzahl bestimmt. Die Teilchenzahl in jedem Kanal variiert in Abhängigkeit von der Verstimmung der Laserfrequenz des letzten Pulses. Aus der Variation der Teilchenzahl kann die Interferometerphase bestimmt werden.

Es sollten die folgenden beiden Fragestellungen beantwortet werden, um den Einfluss der Phasenfehler zu untersuchen:

- Wie hoch ist der Teilchenverlust bei einem realistischeren Modell?
- Wie wirken sich Phasenfehler der Wellenfronten auf die Interferometerphase aus?

Geringere Teilchenzahlen führen zu einem schlechteren Signal-Rausch-Verhältnis und letztlich zu einem geringeren Kontrast der Interferenzstreifen. Das schränkt die Präzision bei der Messung der Interferometerphase ein. Ein Fehler in der Interferometerphase führt u.a. zu einer limitierten Präzision bei der Messung von Beschleunigungen.

Es wurde eine neue Methode zur Bestimmung der Interferometerphase entwickelt. Dazu wurden die ersten beiden Laserpulse und die beiden freien Propagationszeiten simuliert. Für den letzten Puls wurden drei verschiedene Pulse angenommen, die sich in der Frequenzdifferenz zwischen beiden Lasern unterscheiden. Die Anzahl der Teilchen in den Kanälen 1 bis 3 ist abhängig von dieser Frequenzdifferenz. Aus der Teilchenanzahl in den jeweiligen Kanälen lässt sich die Interferometerphase bestimmen. Durch die zwei

zusätzlichen Lichtwechselwirkungen kommt es aber zu längeren Simulationszeiten, welche durch eine Vergrößerung der Schrittweite dt von $1\mu s$ auf $5\mu s$ während der freien Propagation ausgeglichen werden. Gleichzeitig wurde die freie Propagationszeit auf $T = 10.000\mu s$ erhöht, sodass die Rechenzeit insgesamt gleich bleibt.

Es wurden Simulation für mehrere Spiegelrealisierungen mit jeweils gleicher Rauheit und Korrelationslänge durchgeführt und anschließend ein mittlerer Phasenfehler und eine mittlere maximale Teilchenzahl bestimmt. Für verschiedene Paare von Parametern(σ, l) wurde der Phasenfehler und die Teilchenzahl bestimmt.
Man erkennt, dass bei größerer Rauheit der Phasenfehler zunimmt. Bei größeren Korrelationslängen nimmt der Phasenfehler zu.

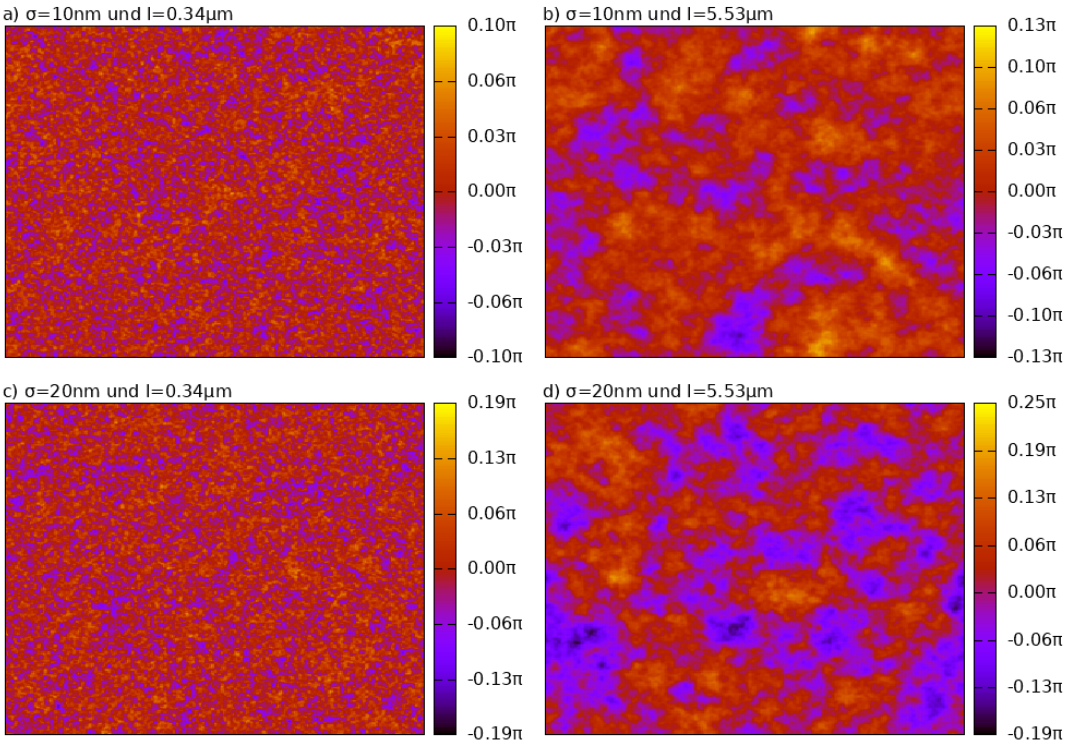

Abbildung 2: Fehler der Laserphasefronten in Abhängigkeit von den gewählten Parametern für die Rauhigkeit σ und Korrelationslänge l für jeweils eine Realisierung eines Spiegels. Der simulierte Spiegelbereich beträgt 100 x 100 μm^2.

Dabei bedeuten größere Korrelationslängen größere Spiegelstrukturen. Im Fall der Korrelationslänge von $l = 0{,}34\mu m$ ist die räumliche Ausdehnung des BEC's deutlich größer als die Spiegelstruktur. Die Spiegelstruktur hat deshalb nur einen geringen Einfluss auf den Phasenfehler. Die Korrelationslänge von $l = 5{,}53\mu m$ entspricht hingegen in etwa der räumlichen Ausdehnung des BEC's. Die Spiegelstruktur erzeugt deshalb einen großen Phasenfehler.

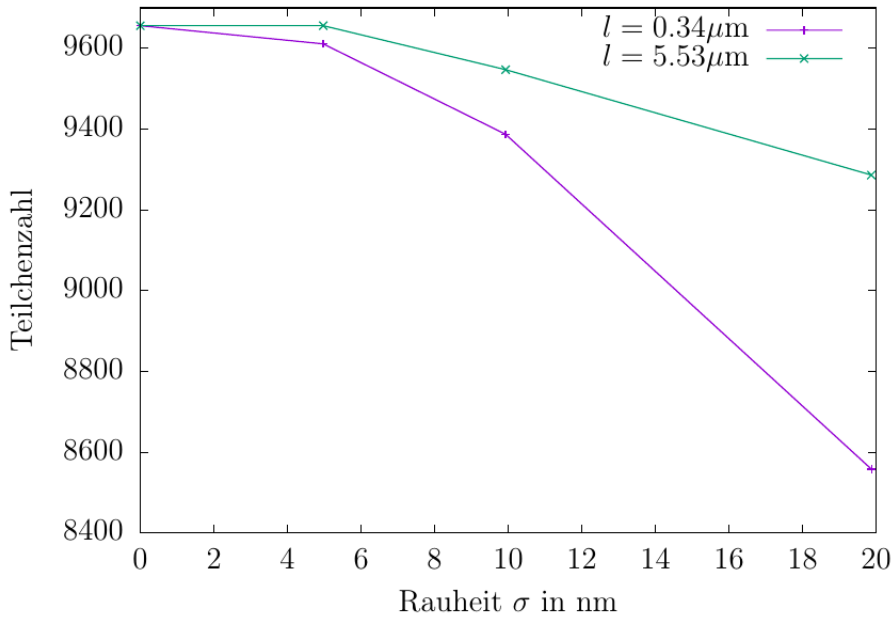

Abbildung 3: Teilchenanzahl in Abhängigkeit von der Rauheit für zwei verschiedene Korrelationslängen l.

Bei größerer Rauheit nimmt die Teilchenzahl ab. Hier führen kleinere Korrelationslängen zu einem größeren Verlust an Teilchen. Durch die kleineren Spiegelstrukturen kommt es zu sehr großen Änderungen der Laserphase.Dies verschlechtert die Effizienz der Strahlteiler.

Mit den von uns gewählten Spiegeln kommt es zu großen Fehlern in der Interferometerphase, die im Experiment auf keinen Fall vernachlässigt werden können. Diese Spiegelfehler führen bei einer Messung der lokalen Gravitationsbeschleunigung g auf einen systematischen Fehler.

Die durch die Gravitationsbeschleunigung verursachte Interferometerphase ist gegeben durch

$$\phi = k(g - g')T^2 := k\bar{g}T^2,$$

wobei *k* der Wellenvektor der Laser, *T* die freie Propagationszeit und *g'* die Kompensation der Dopplerverschiebung ist, die durch die Gravitation verursacht wird. Wir nehmen an, dass die Dopplerverschiebung bis auf $\bar{g}$ kompensiert wird. Diese kann dann durch Messung der Interferometerphase ϕ bestimmt werden. Wenn diese durch einen nicht perfekten Spiegel gestört wird, führt dies somit zu einem Fehler in der Bestimmung von $\bar{g}$.

In unserem Fall ist der Fehler in der Größenordnung von $\Delta\bar{g} \approx 10^{-9} ms^{-2}$. Dies entspricht der Genauigkeit, die auch von PRIMUS für die Überprüfung des schwachen Äquivalenzprinzips angestrebt wird.

Ausblick

Die bisherigen Simulationen geben nur einen Teil des experimentellen Aufbaus wieder. Um eine adäquate und realistischere Analyse von systematische Fehlern im Kontext von Tests des Äquivalenzprinzips mittels der PRIMUS-Experimentapparatur durchzuführen zu können, sollen die Simulationan auf Systeme von BECs, sog. Gemische, ausgeweitet werden. Im

Experiment sollen BEC-Gemische von Rubidium und Kalium im Atom-Interferometer genutzt werden.

Daher müssen und sollen folgende Fragen beantwortet werden:

- Wie beeinflusst das Verhältnis der Teilchenzahlen von BEC-Zwei-Spezies - Gemischen die Effizienz der Strahlteiler und Spiegel?
- Wie wirken sich Phasenfehler auf die Interferometerphase im Hinblick auf Messungen des schwachen Äquivalenzprinzips aus?
- Lassen sich daraus geeignete Strategien ableiten, um das Experiment zu optimieren?

Dies wird mittels einer Parameterstudie geschehen.

Vorträge / Poster

1. J. Rosskamp, Z. Marojevic, E.Göklü, C. Lämmerzahl: „Berücksichtigung optischer Abbildungsfehler bei Atominterferometern", Vortrag auf dem QUANTUS Meeting in Bremen, April 2016

6.23 *hbp00038:* Elektronische und Optische Eigenschaften von Halbleiter-Quantenpunkten

HLRN-Projektkennung:	hbp00038
Laufzeit:	II/2016 – I/2017
Projektleiter:	Dr. Michael Lorke
Projektbearbeiter.	Christian Carmesin, Dr. Stephan Michael, Dr. Matthias Florian
Institut / Einrichtung:	Institute for Theoretical Physics, University of Bremen

Motivation

Eine der Herausforderungen der Quanteninformationstechnologie ist die Realisierung deterministischer Einzelphotonenquellen mit hoher Wiederholungsrate und einstellbarer Emissionsenergie [1].

Selbstorganisierte Quantenpunkte (QDs) sind vielversprechende Kandidaten aufgrund des Vorteils der Integrierbarkeit in elektrische Bauteile [2-3]. Zu den aktuellen Herausforderungen gehört die systematische Erweiterung der Emissionsenergien in die verlustarmen Telekom-Bänder bei 1.3 µm und 1.5 µm [4]. Unser Ziel ist es, ein neues und vielversprechendes Materialsystem von InAs/ InAlGaAs/InP-basierten QDs (s. Abb. 1) zu charakterisieren und dominante Beiträge zum Zusammenhang zwischen Morphologie und optischen Eigenschaften zu identifizieren.

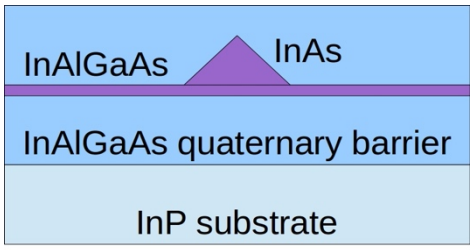

Abb. 1: Schema der verschiedenen Schichten beim Wachstum neuartiger InAs/InAlGaAs/InP-basierter QDs für die Emission im Telekom-Bereich.

Die theoretischen Untersuchungen im Rahmen dieses Projektes wurden in enger Kooperation mit der Arbeitsgruppe von Prof. Dr. Reithmaier aus Kassel (Probenherstellung, optische Charakterisierung) sowie der Arbeitsgruppe von Prof. Dr. Andreas Rosenauer aus Bremen (Transmissions-Elektronen-Mikroskopie (TEM) -Charakterisierung der Proben) durchgeführt, um die elektronischen und optischen Eigenschaften von InAlGaAs-Quantenpunkten systematisch zu analysieren.

Methoden und Ergebnisse

Für elektronische Zustandsberechnungen von Halbleiter-QDs, werden häufig sowohl Kontinuumsmodelle als auch atomistisches TB verwendet. Da die experimentellen Untersuchungen eine TEM Charakterisierung eines einzelnen QDs mit atomarer Auflösung beinhalten, haben wir uns für einen atomistischer TB-Ansatz zur Modellierung entschieden.

Dazu wurde zunächst das Verspannungsfeld der Gesamtstruktur von Quantenpunkt und Quantenfilm-Einbettung anhand der Valence-Force-Field-Methode berechnet (s. Abb. 2).

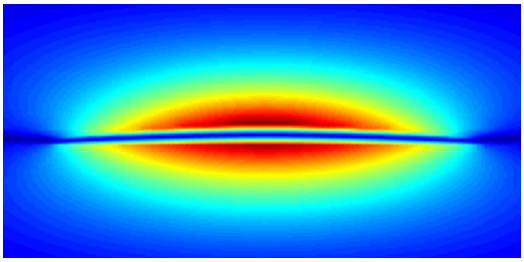

Abb. 2: Verspannungsfeld in xz-Ebene als Querschnitt durch die Mitte der Superzelle. Dargestellt ist der Betrag der Differenz der Atompositionen vor und nach der Minimierung, wobei blau den geringsten Verschiebungen und rot den größten Verschiebungen entspricht.

Dabei werden sowohl die Bindungslängen als auch die Bindungswinkel verändert und neue Atompositionen berechnet. Aufgrund der ausgelenkten Atompositionen entsteht ein Verspannungsfeld, das über eine verallgemeinerte Harrison-Regel in das Tight-Binding-Modell als Modifikation der Kopplungsmatrixelemente einfließt. Das Tight-Binding-Modell bildet auf einem atomaren Gitter (s. Abb. 3) die experimentell bestimmte Geometrie des Quantenpunktes ab, wobei der Einbau von In-Atomen durch konkrete zufällige Realisierungen gemäß dem aus TEM-Untersuchungen bestimmten Konzentrationsprofil berücksichtigt wird. Dabei wird an jedem atomaren Gitterplatz ein Satz lokalisierter orbitaler Basisfunktionen mit je zwei Spinrichtungen sowie Spin-Orbit-Kopplung berücksichtigt. Die Diagonalisierung des Tight-Binding-Hamiltonians liefert die Eigenenergien und Eigenzustände (s. Abb.4) der gebundenen Elektronen- und Loch-Zustände im QD.

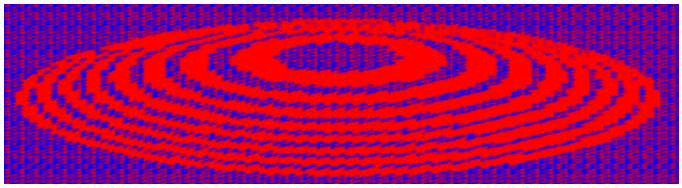

Abb. 3: Modellierung des Quantenpunktes mit atomarer Auflösung: Ausschnitt der Superzelle mit Anionen (As) in blau und Kationen (Al, Ga, In) in rot.

Im Quantenpunkt befinden sich mehrere lokalisierte Zustände, wobei diejenigen, die aus dem Leitungsband (c-band) entstammen als Elektronen und diejenigen, die dem Valenzband (v-band) entstammen als Löcher bezeichnet werden. Zwischen diesen Zuständen sind optische Übergänge möglich, wobei derjenige mit der niedrigsten Übergangsenergie als Grundzustandsübergang (s. Abb. 4 GS) bezeichnet wird. Übergänge mit höherer Emissionsenergie werden als angeregte Übergänge (s. Abb. 4 ES) bezeichnet. Diese sind jeweils exemplarisch in Abb. 4 eingetragen.

Ausgehend von der in Abb.3 dargestellten Struktur haben wir die Einflüsse von Größen- und In-Konzentrationsschwankungen auf die Emissionsenergie des Grundzustandsübergangs untersucht. Für die Analyse von Größenfluktuationen haben wir in verschiedenen Rechnungen einzelner QDs die Größe variiert, indem jeweils ein konstantes Verhältnis von Durchmesser zu Höhe für jeden QD beibehalten wurde. Für eine Analyse der Konzentrationsfluktuationen haben wir in verschiedenen Berechnungen für einzelne QDs die In-Konzentration an der Basis des QDs variiert, wobei die Größe unverändert blieb. Hierbei nahm bei jeder Berechnung die In-Konzentration linear zu bis 100% an der Spitze, während Ga und Al gleichmäßig auf die verbleibenden Kationgitterplätze verteilt wurden.

Wir konnten zeigen, dass für dieses Ensemble von Quantenpunkten die Konzentrationsfluktuationen einen erheblichen Einfluss auf die Übergangsenergien hatten, wogegen die Größenfluktuationen einen vergleichbar geringen Einfluss zeigten.

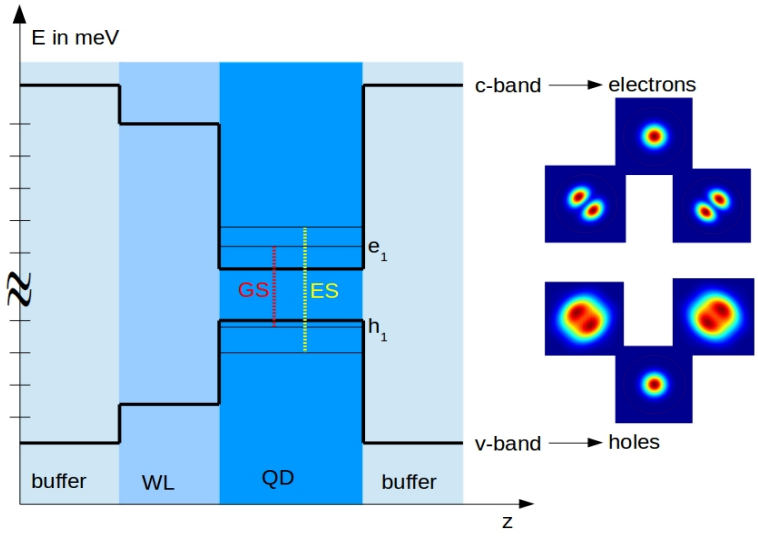

Abb. 4:
Links: Energieniveauschema der Einteilchen-Zustände nach der TB-Diagonaliserung: Innerhalb des quaternären Buffer-Materials (buffer) ist ein Wetting-Layer (WL) eingeschlossen, der wiederum den Quantenpunkt (QD) enthält. Rechts: In z-Richtung integrierte Aufenthaltswahrscheinlichkeit der jeweils niedrigsten drei Elektronen- und Löchzuständen im Quantenpunkt.

Der Grund für den vergleichsweise geringen Einfluss der Größenfluktuationen ist, dass es sich um einen relativ großen Quantenpunkt mit einem Durchmesser von 55nm an der Basis handelte. Somit ist für diesen ohnehin großen Quantenpunkt kaum zu erwarten, dass Größenfluktuationen von +-10% einen erheblichen Einfluss auf die Emissionsenergie haben. Dies kann intuitiv mit dem einfachen Teilchen im Potenzialtopf Modell veranschaulicht werden, bei dem der Einfluss der Emissionsenergie mit mit dem Radius r abnimmt. Legt man dieses vereinfachte Modell zugrunde, so entspricht die Situation des relativ großen Quantenpunktes der Situation der Asymptote der $1/r^2$ Abhängigkeit des Potentialtopf-Modells.

Der relativ starke Einfluss der In-Konzentration kann damit veranschaulicht werden, dass sich die Bandlücken von InAs (~0.5eV) und die von AlAs (~3.0eV) sowie GaAs (~1.3eV) relativ stark unterscheiden und somit der In-Anteil im Quantenpunkt die Emissionsenergie maßgeblich beeinflusst.

Literatur

[1] Z. Y. Zhang, A. E. H. Oehler, B. Resan, S. Kurmulis, K. J. Zhou, Q. Wang, M. Mangold, T. Süedmeyer, U. Keller, K. J. Weingarten, and R. A. Hogg. 1.55 µm inas/gaas quantum dots and high repetition rate quantum dot sesam mode-locked laser. Scientific Reports, 2, 2012.

[2] Dieter Bimberg, Marius Grundmann, and Nikolai N Ledentsov. Quantum dot heterostructures. John Wiley & Sons, 1999

[3] Zhiliang Yuan, Beata E Kardynal, R Mark Stevenson, Andrew J Shields, Charlene J Lobo, Ken Cooper, Neil S Beattie, David A Ritchie, and Michael Pepper. Electrically driven single-photon source. Science, 295(5552):102-105, 2002

[4] L. Brusberg, C. Herbst, M. Neitz, H. Schröder and K. D. Lang, in 2014 The European Conference on Optical Communication (ECOC) (2014), pp. 1–3, ISSN 1550-381X.

Vorträge

C. Carmesin, M. Schowalter, M. Benyoucef, D. Mourad, M. Lorke, J. P. Reithmaier, A. Rosenauer, and F. Jahnke: Influence of morphology on InAlGaAs quantum dots emitting at telecom wavelength – DPG Frühjahrstagung 2017, Dresden